

Fluids confined by nanopatterned substrates

vorgelegt von
Diplom Chemiker
Henry Bock
aus Eisenhüttenstadt

Der Fakultät II
Mathematik und Naturwissenschaften
der Technischen Universität Berlin
zur Erlangung des akademischen Grades

Doktor der Naturwissenschaften
Dr. rer. nat.

genehmigte Dissertation

Promotionsausschuß:

Berichter: Prof. Dr. M. Schoen

Berichter: Prof. Dr. S. Hess

Tag der mündlichen Prüfung: 15. August 2001

Berlin 2001
D 83

Zusammenfassung

Der Einfluß chemischer Heterogenität der Substratoberflächen auf Phasenverhalten und mechanische Eigenschaften von Fluiden in begrenzender Geometrie wird untersucht. In der vorliegenden Arbeit sind Fluide durch chemisch strukturierte, planparallele Substrate auf schlitzförmige Bereiche nanoskopischer Dicke eingeschränkt. Die chemisch strukturierten Substrate bestehen aus alternierenden stark und schwach adsorbierenden Streifen.

Zur Untersuchung des Phasenverhaltens werden Phasendiagramme eines (einfach-kubischen) Gittergases berechnet. Eine modulare Verfahren erlaubt die analytische Berechnung von Phasendiagrammen bei verschwindender Temperatur ($T = 0$). Für $T > 0$ wird das Gittergas innerhalb einer Molekularfeldnäherung behandelt. Das komplexe Phasenverhalten ist unter anderem dadurch gekennzeichnet, daß die Porenkondensation in zwei aufeinander folgende Phasenübergänge erster Ordnung aufspaltet. Während des ersten Überganges wird eine Flüssigkeitsbrücke zwischen den sich gegenüberliegenden stark adsorbierenden Substratteilen gebildet. Brückenphasen unterscheiden sich von allen anderen Phasen, da sie bei allen Abständen zwischen den Wänden laterale Inhomogenitäten aufweisen. Um den Einfluß der Vereinfachungen dieses Modells zu kontrollieren, werden wesentliche Ergebnisse mit Hilfe eines kontinuierlichen Modells überprüft.

Durch relative Verschiebung der Wände gegeneinander, können Flüssigkeitsbrücken einer Scherdeformation αs_x ausgesetzt werden, die zu einer nicht verschwindenden Scherspannung T_{zx} führt. Die entsprechenden Scherspannungskurven $T_{zx}(\alpha s_x)$ stimmen qualitativ mit denen überein, die für feste Filme zwischen atomar strukturierten Wänden gefunden werden. Bei kleinen αs_x verhält sich eine Flüssigkeitsbrücke wie eine Hooke'sche Feder, gefolgt von einem Bereich zunehmender Nichtlinearität, bis schließlich ein Maximum, der sogenannte Haltepunkt erreicht ist. Variationen der Breite der stark und schwach adsorbierenden Streifen führen zu einer Verschiebung des Haltepunktes, ändern jedoch die generelle Form der Scherspannungskurven nicht. Mit Hilfe einer Theorie korrespondierender Zustände können die Scherspannungskurven auf die Koordinaten des Haltepunktes normiert und durch eine systemparameterfreie universelle Kurve repräsentiert werden.

Publikationen von Teilen dieser Dissertation

1. *Phase behavior of a simple fluid confined between chemically corrugated substrates*, Henry Bock and Martin Schoen, Phys. Rev. E **59**, 4122 (1999)
2. *Shear-induced phase transitions in confined lattice gases*, Martin Schoen and Henry Bock, J. Phys.: Condens Matter **12**, A333 (2000)
3. *Thermophysical properties of confined fluids exposed to a shear strain*, Henry Bock and Martin Schoen, J. Phys.: Condens Matter **12**, 1545 (2000)
4. *Shear-induced phase transitions in fluids confined between chemically decorated substrates*, Henry Bock and Martin Schoen, J. Phys.: Condens Matter **12**, 1569 (2000)
5. *Phase behaviour of fluids confined between chemically decorated substrates*, Henry Bock, Dennis J. Diestler and Martin Schoen, J. Phys.: Condens. Matter, **13**, 4697 (2001)

Abstract

The impact of chemical heterogeneity of solid surfaces on phase behavior and mechanical properties of confined simple fluids is investigated. In the present work fluids are confined to a slit of nanoscopic width by chemically decorated, plane-parallel substrates consisting of alternating slabs of weakly and strongly adsorbing solid.

The phase behavior is explored by calculating phase diagrams using a simple-cubic lattice-gas model. A modular approach is developed which allows us to calculate the phase diagram analytically at vanishing temperature ($T = 0$). At higher temperatures $T > 0$ the lattice gas is treated within the mean-field approximation. A rich phase behavior is observed which depends on the large set of parameters needed to describe the heterogeneous confinement. Caused by the chemical heterogeneity of the substrates the capillary condensation is split into two successive first-order phase transitions. During the first transition the gap between opposing strongly adsorbing wall parts is filled with liquid surrounded by vapor, that is a bridge phase forms. Bridge phases are distinguished from all other phases in that they are laterally inhomogeneous at all planes $z = \text{const}$. The mean-field approximation to the lattice-gas model is used since it provides phase diagrams at moderate computational expense. To control the influence of the simplifications inherent in the lattice model, the main findings are verified qualitatively employing a parallel continuous model, which is treated by Monte Carlo simulations.

By misaligning the the opposite substrates, bridge phases can be subjected to a shear strain αs_x . Because of their unique internal structure bridge phases support a nonvanishing shear stress T_{zx} . The shear stress curve $T_{zx}(\alpha s_x)$ is qualitatively similar to the one characteristic of solidlike films confined between atomically structured substrates, in that the response to small strains is Hookean, followed by an increasingly nonlinear regime up to the yield point where $T_{zx}(\alpha s_x)$ assumes its maximum. Variation of the width of strongly and weakly adsorbing slabs causes the yield point to shift, but does not alter the general form of $T_{zx}(\alpha s_x)$. With the aid of a theory of corresponding states, $T_{zx}(\alpha s_x)$ is renormalized by yield stress and strain such that the results can be represented uniquely by a master curve independent of any system parameters.

Contents

1	Introduction	1
2	The mean-field lattice-gas model	12
2.1	The lattice gas model	12
2.1.1	Grand potential	12
2.1.2	The Prototype	14
2.1.3	Nearest-neighbor lattice gas in magnetic language	16
2.2	Exact solutions	17
2.2.1	The grand potential at $T=0$	17
2.2.2	Morphologies at $T=0$	20
2.2.3	Thermodynamically stable morphologies at $T=0$	26
2.3	Mean-Field Theory	32
2.3.1	Variational treatment of the mean field model	33
2.3.2	Bulk phase diagram of the mean-field lattice gas	36
2.3.3	The limit $T=0$	40
2.4	Phase behavior for $T > 0$	42
2.4.1	Grand potential curves	42
2.4.2	Phase diagrams	46
3	The continuous model	56
3.1	The continuous model	57
3.2	Thermodynamics	60
3.3	Statistical Thermodynamics	63
3.3.1	Partition function of the grand mixed isostress-isostrain ensemble	64

CONTENTS

3.3.2	The classical limit	66
3.3.3	Molecular expressions for stress tensor components	68
3.4	Monte Carlo simulation	72
3.4.1	The general method	72
3.4.2	Application and Implementation	74
4	Results	78
4.1	Phase behavior	79
4.1.1	Variation of wall distance	79
4.1.2	Variation of chemical corrugation	90
4.1.3	The impact of shear strain	93
4.2	Thermo-mechanical properties	103
4.2.1	Shear stress of confined fluids	103
4.2.2	Thermodynamic stability	110
5	Discussion and conclusions	118
A	Jacobi–Newton iteration	125
B	Fluid–substrate forces	131
C	Implementation of the fluid–substrate potential	134

Chapter 1

Introduction

Among the three classical states of (single-component bulk) matter, namely gas, liquid and solid there is a clearcut distinction as far as gas and solid are concerned. While the latter is characterized by a highly symmetric and periodic microscopic structure, the former lacks any inherent structural features, that is gases are completely disordered from a molecular perspective. From a structural point of view liquids are somewhat intermediate to both gas and solid, that is off the gas-liquid near-critical regime they exhibit short-range positional order vanishing on a lengthscale set by the range of intermolecular forces.

The three states of matter may be transformed into one another by changing the thermodynamic conditions, that is temperature T , pressure p , or density $\rho = N/V$ (N number of molecules, V volume). The associated phase transitions are accompanied by significant changes in certain system properties. For example, the liquid-solid phase transition is characterized by a qualitative change in the degree of molecular order. Therefore liquid-solid phase transitions appear even at very high pressures where properties such as the mean intermolecular distances are much the same in both phases [1]. Moreover, a liquid-solid critical point is unknown so far. In other words, liquid-solid phase transitions in infinitely large bulk systems are always discontinuous (i.e., first-order according to Ehrenfest's classification [2]) and accompanied by release of latent heat. On the contrary, a key feature of liquid-gas phase transitions is a change in the mean density. If the temperature T is increased coexisting gas and liquid

phases become more and more alike the higher T is. At the critical point they become indistinguishable and the gas–liquid phase transition disappears. This offers the interesting possibility to pass from any gas state to any liquid state continuously along a partially supercritical path in thermodynamic state space. Because one can gradually transform gases into liquids and *vice versa* the term “fluid” is often used to refer to both nonsolid states of matter if a more detailed classification is not required.

The first quantitative picture of gas–liquid phase transitions in the bulk emerged from the thesis of van der Waals published in 1873 [3] (for an English translation see [4]). In his thesis van der Waals proposed an equation of state capable of describing real fluids whose properties are determined by intermolecular forces, attraction and repulsion that is. Because of attractive interactions the van der Waals equation predicts gas–liquid phase transitions for sufficiently low temperatures and existence of a critical point. This is different from liquid–solid transitions which are driven by repulsive interactions, as solidification of hard sphere fluids clearly indicates [5]. In this latter system solidification occurs solely on account of entropic effects.

As far as fluids are concerned it is almost commonplace that a container of some sort is required to keep them. In view of this it seems surprising that only after more than a hundred years after van der Waals physicists became aware of the impact of the container walls on the phase behavior of fluids. The interaction of fluids with solid substrates and its consequences for the phase behavior of fluids near solid surfaces was first realized by Cahn [6] and Ebner and Saam [7, 8]. These works were concerned with ways a fluid wets a solid surface. Since then these wetting phenomena are nowadays perceived as substrate–induced phase transitions in the classical thermodynamic sense. They can be investigated experimentally by measuring the amount of fluid adsorbed on a solid surface or by determining the thickness of the adsorbed film. Experiments are usually carried out under isothermal conditions and (relative) pressures $P/P^{\text{sat}} \leq 1$ where P^{sat} is the saturated–gas pressure for the given temperature T . If T is below the so–called wetting temperature ($T_w < T_c$, T_c critical temperature), the amount of adsorbed fluid Γ remains finite (partial wetting) even for $P/P^{\text{sat}} = 1$, that is at (bulk) gas–liquid coexistence; for $T_w < T < T_c$, Γ becomes infinitely large

(complete wetting), that is, the thickness of the wetting layer attains macroscopic dimensions for $P/P^{\text{sat}} \geq 1$. In addition, Γ may diverge continuously (critical wetting) or discontinuously (first-order wetting) if $T \rightarrow T_w$ such that $P/P^{\text{sat}} = 1$ is maintained. For sufficiently low temperatures, Γ may change discontinuously but remains finite for states off gas-liquid coexistence, that is for $P/P^{\text{sat}} < 1$ [9]. During this prewetting transition the thickness of the wetting layer remains finite, since the infinitely thick film (i.e., the liquid) is still thermodynamically unstable. Points $\{(T, P) | P/P^{\text{sat}} < 1\}$ where prewetting takes place form the prewetting line which ends at the prewetting critical point. Moreover, the formation of the wetting layer may appear in a sequence of first-order phase transitions layer by layer (layering transitions) such that the thickness of the adsorbed liquid film eventually may become infinitely large (roughening) [10, 11].

Wetting of solid substrates plays also an important rôle in common technical applications. Consider, for instance, painting solid surfaces. To obtain particularly nice-looking, smooth surfaces the paint should form a homogeneous layer on the surface. Thus, wetting of the surface by the paint should be optimum. As another example consider special coatings designed to enhancing the wetting of glass surfaces by water. These coatings prevent water from forming small droplets that would otherwise blur the view through the glass. On the contrary, in the automobile industry, where one is concerned with safety aspects, water-repellent glass is utilized to optimize the driver's vision in rain. Instead of perfect wetting one aims at optimizing the "drying" characteristics of the glass so that water can easily form droplets rolling off the glass surface without difficulty [12].

In nature this latter problem is already solved. Leaves of many plants are not wetted by water. The most prominent representative is the so-called "sacred lotus" (*Nelumbo nucifera*) [13]. This is particularly surprising since the leaf consists mostly of water. The key to understanding this so-called lotus-leaf phenomenon is surface roughness, that is the surface of the leaf is covered with asperities characterized by a large aspect ratio. In addition, the surface is coated with water-repellent material.

Wetting of *homogeneous* planar substrates has been intensively studied over

the last twenty years [10, 14, 15, 16]. To explore wetting of *heterogeneous* surfaces and eventually design and fabricate surfaces with specific and controllable local wetting characteristics, an improved understanding of molecular aspects of wetting of heterogeneous surfaces is required. At the nanometer lengthscale, heterogeneity can be achieved by endowing surfaces with geometrical or chemical patterns. Various techniques have been developed to decorate smooth homogeneous surfaces with such structures. For example, lithography frequently used in the fabrication of microelectronic chips can be used to produce structures with typical sizes of the order of a few tenths of a micrometer. Using synchrotron radiation (X-Ray) lithography is capable of generating structures on the micrometer lengthscale, with a remarkably high aspect ratio, that is with a height of up to two millimeters [17]. On the other hand, very small structures from 10 μm to 10 nm are available by using masks in the lithographic process which are formed by a (self-assembled) monolayer of colloidal particles located directly on the surface [18, 19]. Even smaller structures can be realized in thin (submonolayer) films which relieve surface stress by formation of thermodynamically stable, periodically ordered domains on the nanometer scale [20, 21, 22]. Moreover, using scanning probe techniques single atoms can be manipulated [23, 24]. Vapor deposition through grids and microcontact printing are alternative methods.

The manufacturing of micro- and nanostructures using microcontact printing is another well established technique [25, 26, 27, 28, 29]. The core of this method is a polymer stamp which is set up lithographically with subsequent wet chemical etching. In this case the “ink” for the stamp consists of a chemical substance which after printing forms a self assembled monolayer anchored to the surface. The result of this treatment is a chemically heterogeneous surface nearly flat on an atomic lengthscale. Microcontact printing is a relatively simple technique. Stamps can be used several times and a wide range of pattern sizes from tens of centimeters to tens of nanometers is accessible, so that this method may in principle be used in industrial applications. It is furthermore noteworthy that microcontact printing can also be used to decorate curved surfaces [30].

If fluids are exposed to patterned surfaces they are no longer spatially uniform (i.e., homogeneous) as in the bulk. Take as an example a hard sphere fluid

exposed to a periodic array of opposite and parallel hard wedges characterized by a dihedral angle Θ and a distance s_x between the “tips” of this sawtooth-shaped substrate [31]. In Ref. [31], Schoen and Dietrich demonstrated by means of grand canonical ensemble Monte Carlo (GCEMC) simulations that in general the fluid in the corner of such a wedge is more ordered than in the vicinity of the tips. For the special case $\Theta = \pi/2$ a substrate-induced solidlike structure of fourfold in-plane symmetry is observed which cannot exist in the bulk.

Moreover, fluids adsorbed on patterned surfaces comprise a rich variety of morphologies and transitions between them [32]. Consider, for instance, a fluid in single (macroscopic) wedge. Using an effective interface Hamiltonian, Rejmer *et al* [33] showed that wedge filling may compete with wetting of the sloping substrates forming the surface of the wedge. That is, depending on the opening angle of the wedge a so-called prefilling line appears in the phase diagram. It represents a line of first-order phase transitions where the filling height of the liquid in that wedge jumps from a microscopic to a macroscopically large value, while the thickness of the wetting layer sufficiently far away from the corner of the wedge does not vary discontinuously. The influence of the specific geometry of the structured surface has also been investigated by comparing filling transitions in wedges and cones [34].

Studies of fluids wetting *chemically* structured surfaces indicate a strong influence of the substrate structure on the film morphology. Both experimental and theoretical investigations of fluids exposed to chemically striped surfaces show formation of liquid channels along the chemical stripes [35]. A large number of channel morphologies have been observed, that is, depending on the thermodynamic conditions channels on single stripes comprise different volumes [36]. Moreover, liquid can spill over to neighboring channels to form bigger channels which cover more than one chemical stripe. Transitions between these morphologies, which can be either continuous or discontinuous, are also of particular practical interest [37, 38, 39, 40, 41](see below). Experimentally it has been observed that liquid channels may become unstable and undergo a transformation where a bulge occurs along the channels. If the striped surface domains exhibit corners, bulges will be located preferentially at these corners [35]. In Ref. [35] the size of the structured domains is of the order of a few

μm so that optical microscopy can be employed to analyze the morphologies of wetting films. If on the other hand, these structures “live” on the nanometer lengthscale they cannot be resolved by optical microscopy. In this case scanning force microscopy (SFM) in tapping mode can be utilized as an alternative technique [42, 43, 44, 45].

The results summarized above have contributed to a novel field of technical applications referred to as “microfluidics” where one is concerned with the controlled transportation of tiny amounts of valuable liquids. By locally modifying the wetting characteristics of an underlying solid substrate “lanes” for the transportation of liquids can be created such that liquid does not spill over neighboring substrate parts. It is therefore necessary to understand the interplay between fluid–substrate forces and the morphology of the fluid on such a patterned substrate [46]. An example where these principles are invoked already is a continuous flow mixer created on a patterned silicon wafer. This device is capable of mixing nanoliters of fluids on timescales of less than $10\ \mu\text{s}$. Since an investigation of kinetics of chemical reactions is limited by the time needed to mix the reactants, this device enables one to study very fast reaction kinetics inaccessible by conventional mixing technology on account of their much larger mixing times in the range of milliseconds. At the same time only very small amounts of the chemical substances are needed in many applications. Thus, microfluidics provides useful tools to treat valuable fluids such as human DNA [47, 48, 49, 50, 51].

Another interesting application has been reported by Wang *et al* who observed that the wettability of glass coated with TiO_2 can be changed by ultraviolet irradiation [52]. Upon illumination the coated glass is wetted by water, whereas the original, unilluminated coating is water–repellent. Light–induced variation of wetting characteristics may also be used to imprint chemical patterns onto a monolayer film of a polymeric material immobilized on a silicon wafer [53]. The chemical heterogeneity was imprinted by illuminating the coating with ultraviolet light (350nm) through a mask, whereupon the illuminated polymer undergoes a transition from the trans– to the cis–isomer. Thus, it results in a surface with cis and trans domains, which are either wetted (cis–isomer) or nonwetted (trans–isomer) by water, respectively. This system exhibits another

interesting property: by illumination of the surface with blue light (455nm) the structures can be erased completely (transformation to the trans-isomer) and new patterns can be created by subsequent illumination with ultraviolet light.

These examples may suffice to demonstrate the richness and practical importance of wetting of a single solid surface. However, the behavior of fluids becomes even more fascinating if such a fluid is confined by two (or more) solid substrates to spaces of nanoscopic dimension(s), that is spaces comparable in size with the range of the fluid–solid interaction potential. Confinement adds a new lengthscale with profound consequences for the properties of fluids. The most obvious consequence is that confinement precludes roughening and complete wetting because formation of films of macroscopic thickness is impossible (see Ref. [54]). Prewetting and layering, on the other hand, compete with capillary condensation which is the analogue of the bulk gas–liquid phase transition. In general, confinement shifts the coexistence curve of a confined fluid with respect to the bulk. This shift has been observed in sorption experiments, where a fluid vapor is confined to a (random) porous material (VYCOR, CPG) [55, 56, 57]. In particular, a depression of the pore critical temperature and an increase of the the pore critical density with respect to the bulk have been reported [55, 56, 57]. Consequently, the gas–liquid two–phase region (in the T – ρ representation of the phase diagram) has been shifted to higher densities and lower temperatures. The two–phase region is much narrower compared with the bulk. The gas branch of a confined fluid’s phase diagram is more affected than the liquid branch. The shift of the coexistence lines and of the critical point is the stronger the more severe confinement is (see figure 7 in Ref. [55]).

Several theoretical methods are available to study fluids in disordered porous materials [58]. Rosinberg and co-workers investigated the phase behavior of a lattice gas exposed to a disordered (solid) matrix, the latter being realized by placing “wall” particles at random positions on the lattice [59, 60, 61]. Their main findings agree with experimental results discussed above, that is depression of the critical temperature, increase of the critical density, and a narrower gas–liquid two–phase–region. Moreover, at sufficiently low temperatures and densities additional phases appear. In parallel Monte Carlo studies of a Lennard–Jones LJ(12,6) fluid exposed to a random porous matrix Page and

Monson observed that one of these transitions is associated with partial condensation of the fluid in regions where the spherical particles forming the solid matrix are more densely packed [62, 63]. Röcken and co-workers used a mean-field lattice gas model [64] and a density-functional approach [65] to investigate fluids confined by planar, chemically heterogeneous substrates. In their model the chemical heterogeneity of the walls is represented by a wall potential varying sinusoidally in one lateral direction (x) while it is uniform in the other (y). The walls are arranged such that chemically identical parts of the substrates are exactly opposite, that is the substrates are in registry. For this system Röcken and co-workers observed a split capillary condensation occurring as two discontinuous phase transitions. The first transition is related to partial condensation of the fluid in regions where the walls are strongly attractive, that is liquid fills the gap between the opposite strongly attractive substrate parts. In a second step the fluid condenses in the remainder of the system. Thus, eventually the entire pore is filled with liquid. The occurrence of this two-stage capillary condensation was found to depend on the period of the substrate potential, that is it appears only if this period is large compared with the “diameter” of a fluid molecule. Fluids confined by *geometrically* inhomogeneous substrates may form similar liquid bridges in the narrower regions of the pore depending on the thermodynamic conditions [66, 67]. Recently Schoen studied a Lennard–Jones LJ(12,6) fluid confined between solid substrates endowed with wedge-shaped furrows using GCEMC [67]. The furrows are arranged such that they are periodic in one lateral direction and translationally invariant in the other one. A comprehensive overview of actual experiments and theoretical progress is given in reference [68].

Besides phase behavior mechanical properties of confined fluids are of interest. An appropriate device to carry out measurements of mechanical properties of confined phases is the surface forces apparatus (SFA) [69]. The core of an SFA consists of two macroscopically curved cylinders (radius of curvature ca. 1cm), arranged such that their axes are at right angles. This configuration minimizes the contact area on the cylinder surfaces. Due to the macroscopic curvature of the cylinders the surfaces can be taken as parallel on a molecular lengthscale around the point of minimum distance. In most cases the surfaces

of the two cylinders are coated with mica, which can be prepared with atomic smoothness over molecularly large areas. The whole setup is immersed in a reservoir of the fluid of interest. Between the cylinder surfaces a thin film forms in thermodynamic equilibrium with the bulk reservoir. The distance between the two cylinders, which is a measure of film thickness, is determined by optical interferometry. In one particular setup of the SFA the force exerted in direction normal to the fluid–substrate interface is maintained such that the film thickness may fluctuate thermally. This is done by attaching springs to the upper cylinder whereas the lower cylinder remains stationary. In addition a confined film can be exposed to a shear strain by attaching a movable stage to the upper substrate *via* another spring device and moving it at some constant velocity, in a direction parallel to the film–wall interface. Experimentally it is observed that the upper wall first “sticks” to the film as it were because the upper wall remains stationary. From the known spring constant and the measured elongation of the spring, the shear stress sustained by the film can be determined. Beyond a critical shear strain (i.e., at the so-called “yield point” corresponding to the maximum shear stress sustained by the film) the shear stress declines abruptly and the upper wall “slips” across the surface of the film. If the stage moves at a sufficiently low speed the walls eventually come to rest again until the critical shear stress is once again attained so that the stick-slip cycle repeats itself periodically.

A key issue still under discussion is whether or not the rheological behavior of confined phases reflects confinement–induced solidification or not (see [70, 71] and references therein). For instance, Klein and Kumacheva carried out SFA experiments in which an octamethylcyclotetrasiloxane (OMCTS) film confined between mica surfaces is exposed to a shear strain [70, 71]. In SFA experiments OMCTS plays a prominent rôle because of its approximately spherically symmetric molecular structure so that models based upon “simple” fluids (i.e., fluids composed of molecules having only translational degrees of freedom) can be employed theoretically to understand many important aspects of SFA experiments [72]. In their work Klein and Kumacheva find that for large substrate separations of 1160 Å “confined” OMCTS behaves essentially like bulk liquid. In this case a characteristic relative lateral displacement of the upper substrate

is observed on account of thermal noise (see Fig. 6(a) in [70]). This motion remains unaltered if the distance between substrate surfaces is reduced down to approximately 62 Å. However, for a slightly smaller substrate separation of about 54 Å the lateral motion of the upper substrate suddenly disappears as if the film would be capable of “glueing” the substrate to some fixed position in space (see Figs. 6(b) and 6(c) of [70]). Klein and Kumacheva take the abrupt disappearance of lateral substrate motion as evidence of confinement-induced solidification of OMCTS in the narrow gaps between the mica surfaces. If the above films are exposed to oscillatory shear forces, only the thinnest one is capable of sustaining a shear stress which Klein and Kumacheva take as further evidence for a liquid–solid phase transition in OMCTS films triggered by confinement.

Theoretically, most previous studies support the notion of solidification of simple fluids confined by commensurately structured substrate surfaces [73]. However, in this case the fluid and the substrates are composed of the same sort of particles. Thus, under favorable geometrical conditions one expects a strong template effect triggering solidification.

To shed more light on the rôle of solidification as far as mechanical properties of confined fluids are concerned we investigate a model system in which the substrates are perfectly smooth on an atomic lengthscale but decorated with chemical structures such that the confined phase is prevented from solidifying. As will be shown below the partially condensed fluid bridges are capable of sustaining a shear strain. A comprehensive understanding of their rôle can only be achieved if one understands their phase behavior as well. This can be done conveniently by a combination of two complementary treatments. The first is a lattice gas, where we invoke a mean–field approximation for the intrinsic free energy. The second model employs a Lennard-Jones (LJ)(12,6) fluid treated in Monte Carlo simulations.

In chapter 2 we introduce the lattice model. Applying a modular approach, developed in this work we identify possible morphologies of the confined lattice gas and derive exact expressions for the respective grand potentials are derived in the limit of vanishing temperature ($T = 0$). The phase diagram can then be obtained analytically at $T = 0$. For higher temperatures ($T > 0$) the model is

treated at mean-field level which becomes exact in the limit $T = 0$. Within the mean-field approximation the equilibrium phase diagram is obtained numerically at higher temperatures ($T > 0$). A continuous analogue of this model is introduced in chapter 3. It can only be treated by the Monte Carlo method also introduced in that chapter. Chapter 4 is devoted to a presentation of the results. Phase diagrams for various sets of model parameters are presented. Our main findings are verified with the aid of the continuous model. Furthermore, the continuous model is utilized to study bridge phases exposed to shear strains. A theory of corresponding states is employed to derive a master-curve description for the shear stress curves free of any model-dependent parameters. A discussion of the results and the conclusions drawn from them are represented in chapter 5.

Chapter 2

The mean-field lattice-gas model

2.1 The lattice gas model

2.1.1 Grand potential

We consider a fluid made up of structureless molecules, that is molecules without internal degrees of freedom. Their positions are constrained to the $n_x \times n_y \times n_z$ nodes of a simple cubic lattice, where the lattice constant ℓ is infinitesimally larger than the molecular *diameter*. Any site can be occupied by at most a single molecule. This restriction is caused by the infinite (hard-core) repulsion between molecules occupying the same site. Attractive interactions between molecules are limited to nearest neighbours. They are described by a square-well potential, where depth and width of the attractive well are ϵ_{ff} (coupling constant) and ℓ , respectively. We also assume that the fluid is confined in the z -direction between two plane-parallel substrates. A molecule located at site i is subjected to an (external) field Φ_i . Thus, the Hamiltonian of the lattice gas can be written

$$H^{\text{LG}}(\mathbf{s}) = -\frac{\epsilon_{\text{ff}}}{2} \sum_{i=1}^{\mathcal{N}} \sum_j^{\nu_i} s_i s_j + \sum_{i=1}^{\mathcal{N}} \Phi_i s_i - \mu \sum_{i=1}^{\mathcal{N}} s_i \quad (2.1)$$

where μ is the chemical potential and s_i stands for the occupation number of site i , namely

$$s_i = \begin{cases} 0 & , \text{empty site} \\ 1 & , \text{occupied site} \end{cases} \quad (2.2)$$

in a given configuration $\mathbf{s} = \{s_1, s_2, \dots, s_{\mathcal{N}}\}$, $\mathcal{N} = n_x n_y n_z$ is the number of lattice sites, and ν_i is the number of nearest neighbour sites of site i . For the present confined simple-cubic lattice

$$\nu_i = \begin{cases} 5 & , \text{if } i \text{ is located next to the substrate} \\ 6 & , \text{otherwise} \end{cases} \quad (2.3)$$

Since Φ_i is arbitrary and because the second and the third terms on the right side of (2.1) are both linear in the occupation numbers it is convenient to introduce an “intrinsic” chemical potential *via*

$$\mu_i^{\text{LG}} := \mu - \Phi_i \quad (2.4)$$

so that (2.1) simplifies to

$$H^{\text{LG}}(\mathbf{s}) = -\frac{\epsilon_{\text{ff}}}{2} \sum_{i=1}^{\mathcal{N}} \sum_j^{\nu_i} s_i s_j - \sum_{i=1}^{\mathcal{N}} \mu_i^{\text{LG}} s_i \quad (2.5)$$

The grand partition function of the confined lattice gas can be cast as

$$\begin{aligned} \Xi^{\text{LG}} &= \sum_{\mathbf{s}} \exp[-\beta H^{\text{LG}}(\mathbf{s})] \\ &= \sum_{\mathbf{s}} \exp \left\{ -\beta \left[-\frac{\epsilon_{\text{ff}}}{2} \sum_{i=1}^{\mathcal{N}} \sum_j^{\nu_i} s_i s_j - \sum_{i=1}^{\mathcal{N}} \mu_i^{\text{LG}} s_i \right] \right\} \end{aligned} \quad (2.6)$$

where the sums are taken over all sets \mathbf{s} and $\beta = (k_{\text{B}}T)^{-1}$ (T is the temperature and k_{B} is Boltzmann’s constant). To make contact with thermodynamics we invoke the customary statistical-physical expression for the grand potential

$$\begin{aligned} \Omega^{\text{LG}} &= -\beta^{-1} \ln \Xi^{\text{LG}} \\ &= -\beta^{-1} \ln \sum_{\mathbf{s}} \exp \left\{ -\beta \left[-\frac{\epsilon_{\text{ff}}}{2} \sum_{i=1}^{\mathcal{N}} \sum_j^{\nu_i} s_i s_j - \sum_{i=1}^{\mathcal{N}} \mu_i^{\text{LG}} s_i \right] \right\} \end{aligned} \quad (2.7)$$

where the second line follows directly from (2.6). The grand potential in (2.7) is the quantity of prime interest. Consequently, the subsequent discussion will focus on it.

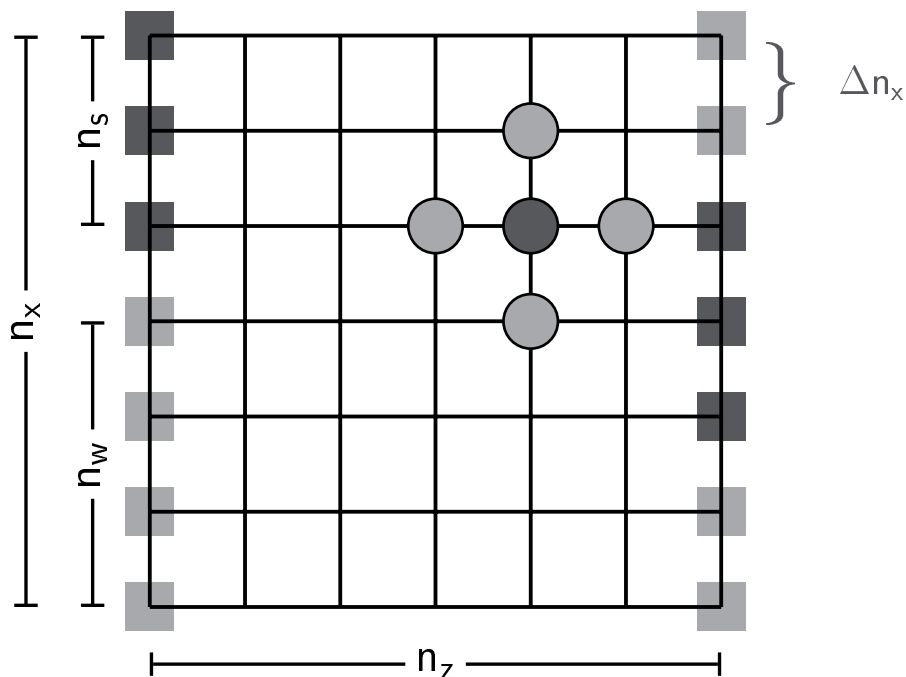


Figure 2.1: Schematic of the prototypical model: cubic lattice gas confined between substrates consisting of strongly attractive stripes alternating periodically with weakly attractive ones. Sites at which a molecule is subject to the strongly attractive substrate ($\Phi_i = -\epsilon_{fs}$) are indicated by dark gray squares; those at which a molecule is subject to the weakly attractive substrate ($\Phi_i = -\epsilon_{fw}$) are denoted by light gray squares. A molecule in central region (black circle) interacts with its six nearest neighbours. The four in the x - z -plane are depicted as gray circles; the two in the y -direction are not shown.

2.1.2 The Prototype

So far the external potential Φ_i is completely arbitrary. However, henceforth it will be associated with the confining substrates. Various confinement scenarios are realized through different choices for Φ_i . The prototype consists of two parallel substrates in the x - y -plane confining the lattice gas in the $\pm z$ -direction. Each substrate comprises stripes composed of different chemical species, whose interaction with the lattice gas is strongly (coupling constant ϵ_{fs}) or weakly (coupling constant ϵ_{fw}) attractive, respectively (see figure 2.1). The stripes are located in the range $1 \leq x \leq n_s$, $-\infty < y < +\infty$ (weak) and $n_s < x \leq n_x$,

$-\infty < y < +\infty$ (strong), such that they are parallel with the y -axis and alternate periodically (period n_x) in the x -direction. Periodicity in the x -direction is realized by applying periodic boundary conditions. Since the external potential is translationally invariant in the y -direction, system properties are translationally invariant in that direction. The attraction with the substrates is short-range: only molecules located at sites across the x - y -planes at $z = 1, n_z$ interact with the substrates. In addition, the substrates may be misaligned in the x -direction by shifting the strongly attractive portion of the upper substrate by Δn_x lattice sites in the $+x$ -direction. For this purpose it is convenient to introduce a parameter $\alpha := \Delta n_x/n_x$ to specify the misalignment of the substrates quantitatively where $\{\alpha \mid 0 \leq \alpha \leq \alpha_{\max} = \min[\frac{1}{2}, (n_x - 1)/2n_x]\}$. If $\alpha = 0$ the substrates are “in registry”, i.e. strongly and weakly attractive portions of both substrates are exactly opposite each other; $\alpha = \alpha_{\max}$ if the misalignment is maximum (i.e., substrates “out of registry”). Notice, α varies discontinuously because of the discrete nature of the lattice. Thus, α is a measure of shear strain imposed on the confined lattice gas.

The external potential Φ_i of the prototype is given by

$$\Phi_i = \Phi_i^{[1]} + \Phi_i^{[2]} \quad (2.8)$$

where

$$\Phi_i^{[2]} \equiv \Phi^{[2]}(x, z) = \left\{ \begin{array}{ll} \infty, & z > n_z \\ -\epsilon_{fs}, & 1 + \alpha n_x \leq x \leq n_s + \alpha n_x \\ -\epsilon_{fw}, & 1 \leq x < 1 + \alpha n_x \\ -\epsilon_{fw}, & n_s + \alpha n_x < x \leq n_x \\ 0, & z < n_z \end{array} \right\} \quad (2.9)$$

specifies the interaction of the lattice gas with the upper substrate. Likewise

$$\Phi_i^{[1]} \equiv \Phi^{[1]}(x, z) = \left\{ \begin{array}{ll} \infty, & z < 1 \\ -\epsilon_{fs}, & 1 \leq x \leq n_s \\ -\epsilon_{fw}, & n_s < x \leq n_x \\ 0, & z > 1 \end{array} \right\} \quad (2.10)$$

represents the interaction with the lower substrate.

2.1.3 Nearest-neighbor lattice gas in magnetic language

By applying “magnetic” language the prototype can be transformed into an Ising magnet in a local magnetic field h_i . This can be demonstrated by starting from the Ising Hamiltonian [74]

$$H^{\mathbf{I}} = -J \sum_{i,j} \sigma_i \sigma_j - \sum_{i=1}^{\mathcal{N}} h_i \sigma_i \quad (2.11)$$

where $\sigma_i = \pm 1$ is a double-valued spin-variable (+1 and -1, corresponding to “spin up” and “spin down”, respectively). Coupling constant J is a measure of the strength of the interaction between neighboring spins and h_i is the (local) external field acting on lattice site i . In (2.11) $\sum_{i,j}$ stands for summation over all nearest-neighbour pairs. Notice that (2.11) is valid regardless of the specific lattice considered. It is therefore convenient to rewrite (2.5) in a similar fashion as

$$H^{\text{LG}} = -\epsilon_{\text{ff}} \sum_{i,j} s_i s_j - \sum_{i=1}^{\mathcal{N}} \mu_i^{\text{LG}} s_i . \quad (2.12)$$

Spin variables can be translated into occupation numbers by means of the transformation

$$\sigma_i = 2s_i - 1 . \quad (2.13)$$

Thus, replacing σ_i in (2.11) according to (2.13) we obtain after some rearrangements

$$H^{\mathbf{I}} = -4J \sum_{i,j} s_i s_j + 2 \sum_{i,j} (J\nu_i - h_i) s_i + \sum_i^{\mathcal{N}} \left(\frac{1}{2} J\nu_i + 1 \right) . \quad (2.14)$$

Comparison with (2.12) shows that

$$H^{\mathbf{I}} = H^{\text{LG}} + \sum_i^{\mathcal{N}} \left(\frac{1}{2} J\nu_i + 1 \right) \quad (2.15)$$

based upon the transformation rules

$$\epsilon_{\text{ff}} = 4J \quad J = \frac{\epsilon_{\text{ff}}}{4} \quad (2.16)$$

$$\mu_i^{\text{LG}} = 2(J\nu_i - h_i) \quad h_i = J\nu_i - \frac{\nu_i}{2} \quad (2.17)$$

converting lattice-gas into magnetic language.

The close correspondence between lattice-gas and magnetic language as reflected by (2.15) is caused by the restriction to nearest-neighbor interactions

and the fact that both σ_i and s_i are double-valued. However, there are differences between the languages. Their origin are the different symmetries of the intermolecular interactions and the interaction of a lattice molecule with the external fields (h_i, μ_i^{LG}) . First, in both languages the interaction with the external field has the same symmetry. For example, in lattice-gas language a particular site i contributes $-\mu_i^{\text{LG}}$ to the Hamiltonian if it is occupied and 0 otherwise. In magnetic language, on the other hand, this contribution is $-h_i$ or $+h_i$ if the spin at site i is “up” (+1) or “down” (−1), respectively. Shifting the magnetic field by $-h_i$ at each lattice site it is simple to realize that sites with spin “up” contribute $-2h_i$ to the Hamiltonian whereas the contribution of sites with spin down vanishes. Comparison with lattice-gas language reveals the like symmetry. The term $2h_i$ on the right side of (2.17) is caused by this shift of the external field.

Consider now the symmetry of the interparticle interaction. Imagine two neighbouring spins are parallel (“up” or “down”) contributing $-J$ to the Hamiltonian if they are parallel (both “up” or both “down”) and $+J$ if they are antiparallel. In lattice-gas language we observe a nonvanishing contribution to H^{LG} only if two neighbouring sites are occupied. Inspecting the translation rules for the fields (2.17), one realizes that an Ising model without an external field $h_i = 0$ is equivalent to a lattice-gas with a field $\mu_i^{\text{LG}} = 2J\nu_i$.

2.2 Exact solutions

2.2.1 The grand potential at $\mathbf{T}=0$

To understand the phase behavior of the prototype introduced in section 2.1.2 we seek (global) minima of its grand potential given in (2.7) for fixed μ and T . In the limit of vanishing temperature the phase diagram can be determined analytically. To demonstrate this we begin by calculating the grand potential in that limit. Starting from (2.6) we assume that a configuration \mathbf{s}_0 exists such that it corresponds to the maximum term in the sum on \mathbf{s} in (2.6). It is then convenient to separate the maximum term from the remainder according to

$$\Xi = \exp[-\beta H^{\text{LG}}(\mathbf{s}_0)] + \sum_{\mathbf{s} \neq \mathbf{s}_0} \exp[-\beta H^{\text{LG}}(\mathbf{s})] \quad (2.18)$$

where $H^{\text{LG}}(\mathbf{s})$ is given by (2.5). The largest term in (2.18), $\exp[-\beta H^{\text{LG}}(\mathbf{s}_0)]$ is determined by the set \mathbf{s}_0 for which $H^{\text{LG}}(\mathbf{s}_0)$ is smallest, i.e. the one minimizing the Hamiltonian. From (2.18)

$$\Xi = \exp[-\beta H^{\text{LG}}(\mathbf{s}_0)] \left(1 + \sum_{\mathbf{s} \neq \mathbf{s}_0} \exp\{-\beta [H^{\text{LG}}(\mathbf{s}) - H^{\text{LG}}(\mathbf{s}_0)]\} \right) \quad (2.19)$$

and

$$\begin{aligned} \Omega &= -\beta^{-1} \ln \Xi & (2.20) \\ &= H^{\text{LG}}(\mathbf{s}_0) - \beta^{-1} \ln \left\{ 1 + \sum_{\mathbf{s} \neq \mathbf{s}_0} \exp(-\beta [H^{\text{LG}}(\mathbf{s}) - H^{\text{LG}}(\mathbf{s}_0)]) \right\} \end{aligned}$$

obtain without further ado. In the limit $T \rightarrow 0$ the sum in $\{\dots\}$ in (2.20) vanishes rapidly since $\beta \rightarrow \infty$. Hence the logarithmic term in (2.20) vanishes much more rapidly than linearly. Thus, for $T = 0$

$$\Omega = H^{\text{LG}}(\mathbf{s}_0) = -\frac{\epsilon_{\text{ff}}}{2} \sum_{i=1}^{\mathcal{N}} \sum_j^{\nu_i} s_{i0} s_{j0} + \sum_{i=1}^{\mathcal{N}} \mu_i^{\text{LG}} s_{i0}. \quad (2.21)$$

According to (2.21) the partition function reduces to a single term in the limit of vanishing temperature. In other words the maximum term method is exact in that limit, which has some important and useful implications. Consider, for example, the mean value $\langle M \rangle$ of any thermodynamic observable M . At $T = 0$ it is given by

$$\langle M \rangle = M(\mathbf{s}_0) \quad (2.22)$$

according to the above rationale. Obviously, this implies there are no correlations, that is

$$\langle s_i s_j \rangle - \langle s_i \rangle \langle s_j \rangle = s_{i0} s_{j0} - s_{i0} s_{j0} = 0 \quad \forall i, j \quad (2.23)$$

and consequently

$$\langle (M - \langle M \rangle)^2 \rangle = \langle M^2 \rangle - \langle M \rangle^2 = M^2(\mathbf{s}_0) - M^2(\mathbf{s}_0) = 0. \quad (2.24)$$

Notice also that (2.21) is free of any entropic contributions in accordance with the third law. At thermodynamic equilibrium and for $T = 0$ the set of \mathbf{s}_0 minimizes the grand potential, and therefore it minimizes the total energy of the lattice gas. Obviously, energetically equivalent sites (i.e., sites at which

lattice-gas molecules are subjected to identical interactions with their neighbors *and* with the external potential) must have the same value of the occupation numbers. This permits one to deduce several important conclusions concerning the prototype (see figure 2.1). For example, along the y -direction all sites are exposed to the same μ_i^{LG} since Φ_i [see (2.9),(2.10)] is translationally invariant in this direction. We may therefore restrict the discussion to an effectively two-dimensional problem. Because of the spatial variation of Φ_i , regions characterized by identical occupation numbers can be identified. The reason for that is not immediately obvious but will become clear shortly when we delineate a strategy to identify such regions by applying a modular approach. This allows us to construct a hierarchy of increasingly complex modules sequentially from simpler ones, starting from the bulk. Any module, which gives rise to a set of so-called morphologies $\{\mathcal{M}\}$, consists of a juxtaposition of one or more of the previous (simpler) modules. We introduce the term “morphology” to refer to the set of energetically homogeneous regions in which the occupation numbers are identical at all sites pertaining to such a region according to the above discussion. However, occupation numbers will generally differ between different such regions. Thus,

$$\mathcal{M} := \{s_i\} . \quad (2.25)$$

The modular approach to construct more complex modules from simpler ones consists of two steps. In the first one, auxiliary surfaces are introduced in the simpler module by breaking a certain number of bonds. This reduces ν_i from 6 to 5 for all sites located at this newly created surface according to (2.3). In the second step two simpler modules are juxtaposed and the auxiliary surfaces between them are removed. Thereby new bonds are created now connecting the original simpler modules across the interface. The grand potential of a given morphology within the more complex module can therefore be expressed as a sum of the grand potentials of the simpler ones, plus corrections which account for the breaking of bonds between nearest neighbors in the simpler modules and the making of new bonds across the interfaces between modules that make up the new composite (more complex) module. Since the system consists of a certain number of regions \hat{n} with equal occupation numbers, we replace individual occupation numbers by occupation numbers for the entire

region by introducing the notion of block occupation numbers \hat{s}_i . Therefore the definition of the morphologies (2.25) simplifies to

$$\mathcal{M} := \{\hat{s}_i\} \quad (2.26)$$

Since \hat{s}_i [like s_i see (2.2)] is double-valued, the number of morphologies conceivable in principle is given by

$$\text{number of morphologies} = 2^{\hat{n}}. \quad (2.27)$$

As we will see shortly for the system of interest, \hat{n} is always small so that only a few morphologies need to be considered. This is because the structure of Φ_i is still quite simple. For more complex external fields such as, for instance, the one characterizing random porous media [58, 61], $2^{\hat{n}}$ may become overwhelmingly large. Because of the small number of possible morphologies in the present case one can construct the phase diagram at $T = 0$ in a straightforward fashion since Ω is an analytic function of the block occupation numbers based upon the modular approach described above. This shall be demonstrated in the following section.

2.2.2 Morphologies at T=0

Bulk lattice gas.

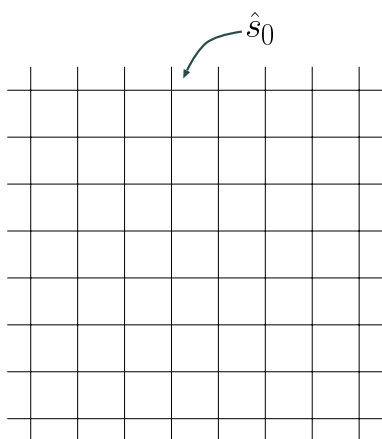


Figure 2.2: Bulk module: All sites are identical. Only one (double-valued) block occupation number \hat{s}_0 accounts for all possible morphologies.

In the simplest case ($\Phi \equiv 0, \nu_i = 6$) (i.e., the bulk lattice gas) all sites are equivalent, so that only one block occupation number \hat{s}_0 is required. Thus,

(2.21) reduces to

$$\Omega_b = -\mathcal{N} \left(\frac{\nu}{2} \epsilon_{\text{ff}} \hat{s}_0^2 + \mu \hat{s}_0 \right) =: \mathcal{N} \omega_0. \quad (2.28)$$

In (2.28), ω_0 is the grand-potential density (per site) of the bulk lattice gas. Because \hat{s}_0 is double-valued, (2.28) gives two possible morphologies [see also (2.27)], namely a “gas” characterized by $\mathcal{M}^g = \{0\}$ having grand potential $\Omega_b^g = 0$ and corresponding to an entirely empty lattice ($\hat{s}_0 = 0$). In addition a “liquid” exists characterized by $\mathcal{M}^l = \{1\}$ and $\Omega_b^l = -\mathcal{N} \left(\frac{\nu}{2} \epsilon_{\text{ff}} + \mu \right)$ where all sites are occupied ($\hat{s}_0 = 1$). Gas and liquid phases may coexist at μ_x^{gl} defined through

$$\Omega_b^g(\mu_x^{\text{gl}}) = \Omega_b^l(\mu_x^{\text{gl}}) =: \Omega_b^{\text{gl}}(\mu_x^{\text{gl}}) = 0 = \mathcal{N} \left(\frac{\nu}{2} \epsilon_{\text{ff}} + \mu_x^{\text{gl}} \right) \quad (2.29)$$

from which $\mu_x^{\text{gl}} \epsilon_{\text{ff}}^{-1} = -\nu/2 = -3$ is easily deduced (see section 2.3.2 and [74]). Thus, for $\mu < \mu_x^{\text{gl}}$, gas is the thermodynamically stable phase, whereas for $\mu > \mu_x^{\text{gl}}$ liquid is the stable phase.

Hard substrates.

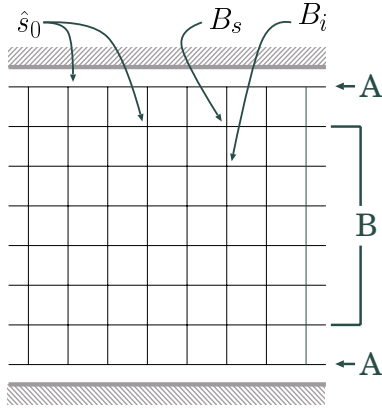


Figure 2.3: Hard-wall module: Sites of groups A and B have different coordination numbers 5 and 6, respectively. Nevertheless, all sites have the same occupation number \hat{s}_0 (see text).

The next slightly more complicated situation is one in which a lattice gas is confined in the z -direction by two planar hard substrates represented by

$$\Phi_i \equiv \Phi_{\text{hs}}(z) = \begin{cases} \infty & z < 1, z > n_z \\ 0 & 1 \leq z \leq n_z \end{cases}, \quad (2.30)$$

where $\Phi_{\text{hs}}(z)$ serves to introduce “surfaces” in the spirit of section 2.2.1. From an inspection of (2.30) it is obvious that the system is translationally invariant in directions parallel to the walls, but comprises two types of sites. All sites

which are located in lattice planes next to the walls, i.e. the surface planes, have a lower coordination number ($\nu_i = 5$) than “core” sites ($\nu_i = 6$). However, all sites are still occupied equivalently and possible morphologies can be described by a single occupation number \hat{s}_0 as for the bulk. To see this, suppose two types of sites exist labeled “A” and “B” with associated block occupation numbers \hat{s}_A and \hat{s}_B , respectively (see figure 2.3). The set of B sites can be subdivided by distinguishing sites labeled B_s which are connected to A sites and sites labeled B_i which are connected to other B sites only. Imagine now $\hat{s}_B = 1$ and $\hat{s}_A = 0$ then sites B_s have only $\nu_i = 5$ occupied nearest-neighbor sites. If it is favorable to occupy the B_s sites then it must be even more favorable to occupy sites A, because in that case A sites have $\nu_i = 5$ occupied nearest-neighbor sites (as B_s before) and B_s sites capture one additional occupied nearest-neighbor site ($\nu_i = 6$). Thus, the latter occupation scenario is energetically preferential. In principle, this rationale can be applied to any other distribution of A and B sites, hence one concludes occupation numbers of all sites to be identical $\hat{s}_A = \hat{s}_B = \hat{s}_0$. It is important to realize that by introducing a hard substrate which corresponds only to the breaking of certain bonds no new morphologies arise. This observation validates and motivates the modular approach. It holds regardless of the complexity of the original modules.

According to our modular approach the present confined lattice gas may be viewed as a bulk system, plus “surfaces”. We can then express the grand potential of the confined phase as

$$\Omega_{\text{hs}} = \Omega_{\text{b}} + \Delta\Omega \quad (2.31)$$

where Ω_{b} pertains to the bulk module and the correction $\Delta\Omega$ accounts for the interactions that are missing for molecules in the surface planes $z = 1$ and $z = n_z$. Since each nearest-neighbor interaction contributes $-\epsilon_{\text{ff}}s^2/2$ per particle to the configurational energy of the original bulk module, and since there are $n_x n_y$ molecules in each surface and two surfaces, the total correction is $n_x n_y \epsilon_{\text{ff}} s^2$. We can therefore rewrite (2.31) as

$$\Omega_{\text{hs}} = n_x n_y n_z \omega_0 + n_x n_y \epsilon_{\text{ff}} s_0^2 = n_x n_y (n_z \omega_0 + \epsilon_{\text{ff}} s_0^2) \quad (2.32)$$

where ω_0 is defined by (2.28). The only effect of confinement is an upward shift in the chemical potential at gas-liquid coexistence. By solving the analogue of

(2.29), $\Omega_{\text{hs}}^g(\mu_x^g) = \Omega_{\text{hs}}^l(\mu_x^g)$, we obtain $\mu_x^g \epsilon_{\text{ff}}^{-1} = -\nu/2 + 1/n_z = -3 + 1/n_z$. As expected, this shift vanishes in the limit of large substrate separations (i.e., as $n_z \rightarrow \infty$).

Chemically homogeneous substrates.

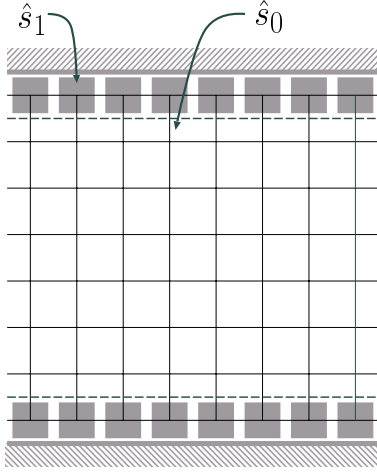


Figure 2.4: Homogeneous-wall module: Two occupation numbers \hat{s}_0 , \hat{s}_1 account for the occupation of the two types of sites. Dotted lines demarcate the position of the auxiliary surfaces. Gray squares represent sites at which lattice-gas molecules are subject to attractive interaction with the substrates.

The situation discussed above becomes slightly more complicated if one replaces (2.30) by

$$\Phi_i \equiv \Phi_{\text{hom}}(z_i) = \begin{cases} \infty & z < 1, z > n_z \\ -\epsilon_{\text{fs}}, & z = 1, z = n_z \\ 0 & 2 \leq z \leq n_z - 1 \end{cases} \quad (2.33)$$

that is by chemically homogeneous substrates capable of attracting the lattice gas in addition to merely confining it. Caused by the external potential Φ_i (2.33) the system now comprises two types of sites (subscripts 0 and 1), since the energy contribution from the external potential might dominate all other contributions. Sites of type 0 having the intrinsic chemical potential $\mu_0^{\text{LG}} = \mu$ [see (2.4)] are located in the region $\{z | 2 \leq z \leq n_z - 1\}$ whereas sites of type 1 with $\mu_1^{\text{LG}} = \epsilon_{\text{fs}} + \mu$ are located at $\{z | z = 1, z = n_z\}$. The grand potential of the lattice gas confined between homogeneous attractive substrates can thus be determined by sandwiching an $n_x \times n_y \times (n_z - 2)$ hard-substrate module [which consists of a slab of uniformly occupied ($\hat{s}_1 = 0$ or 1) sites] between two $n_x \times n_y \times 1$ hard-substrate modules (i.e., identical thin slabs of $n_x n_y$ uniformly

occupied sites). Using the modular principle, we can express the grand potential of the composite “homogeneous” module as

$$\Omega_{\text{hom}} = \Omega_{\text{hs}}^{[0]} + 2\Omega_{\text{hs}}^{[1]} + \Delta\Omega \quad (2.34)$$

where

$$\begin{aligned} \Omega_{\text{hs}}^{[0]} &:= n_x n_y [(n_z - 2)\omega_0 + \epsilon_{\text{ff}} \hat{s}_0^2] \\ \Omega_{\text{hs}}^{[1]} &:= n_x n_y [\omega_1 + \epsilon_{\text{ff}} \hat{s}_1^2] \end{aligned} \quad (2.35)$$

and Ω_{hs} stands for the grand potential of the previous member of the hierarchy of modules, namely a slab between hard substrates. The index 0 denotes the central module at $\mu_0^{\text{LG}} \equiv \mu$, while index 1 pertains to the other two (identical) modules at $\mu_1^{\text{LG}} = \mu + \epsilon_{\text{fs}}$. Since Ω_{hs} already accounts for the breaking of bonds to create auxiliary surfaces (see discussion of the previous simpler module), the correction $\Delta\Omega$ in (2.34) is due solely to the formation of bonds across the two interfaces and is given by $-2n_x n_y \epsilon_{\text{ff}} \hat{s}_0 \hat{s}_1$. Therefore, we can rewrite (2.34) as

$$\Omega_{\text{hom}} = n_x n_y \psi \quad (2.36)$$

where

$$\psi := 2(\omega_1 + \epsilon_{\text{ff}} \hat{s}_1^2) + (n_z - 2)\omega_0 + \epsilon_{\text{ff}} \hat{s}_0^2 - 2\epsilon_{\text{ff}} \hat{s}_0 \hat{s}_1. \quad (2.37)$$

Since the present module consists of two types of sites, four different morphologies arise from the homogeneous module [see (2.27)]. These can be identified by sets of occupation numbers $\mathcal{M} = \{\hat{s}_0, \hat{s}_1\}$, where \hat{s}_0 and \hat{s}_1 are the block occupation numbers of the central and outer slabs, respectively.

Chemically heterogeneous substrates.

Consider now the prototype: a lattice gas between substrates decorated with strongly attractive stripes (ϵ_{fs}) that alternate periodically with weakly attractive stripes (ϵ_{fw}) in the x -direction (see section 2.1.2). We restrict our consideration to the case of perfectly aligned substrates, i.e. $\Delta n_x = 0$. Thus, within one period the potential can be represented as

$$\Phi_i \equiv \Phi_{\text{het}}(x, z) = \begin{cases} \infty & z < 1, z > n_z \\ \left\{ \begin{array}{l} -\epsilon_{\text{fs}} \quad 1 \leq x \leq n_s \\ -\epsilon_{\text{fw}} \quad n_s < x \leq n_x \end{array} \right\} & z = 1, z = n_z \\ 0 & 2 \leq z \leq n_z - 1. \end{cases} \quad (2.38)$$

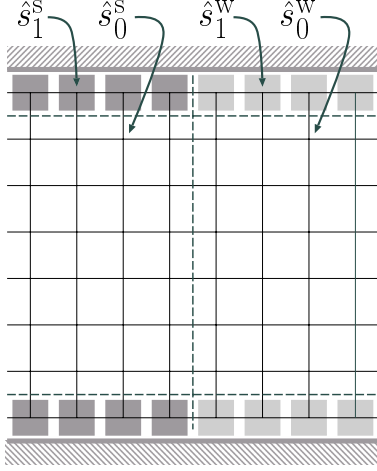


Figure 2.5: Heterogeneous-wall module: Four occupation numbers $\hat{s}_0^w, \hat{s}_1^w, \hat{s}_0^s, \hat{s}_1^s$ account for the occupation of the four groups of sites. Dotted lines demarcate the boundaries of the groups. Gray squares symbolize attractive interaction with the wall. Dark gray squares indicate “strong” interaction (ϵ_{fs}) and light gray squares indicate “weak” interaction (ϵ_{fw}). (See section 2.1.2 for details.)

Because of the different attraction acting on sites of the surface planes, these planes have to be subdivided into two groups. Since the central region is bounded by these two groups, it subdivides into two groups as well (see figure 2.5). Again following the modular principle, we can determine the grand potential by juxtaposing (in the x -direction) two modules corresponding to the previous, simpler one: the lattice gas between homogeneous attractive substrates. Thus, we can write the grand potential as

$$\Omega_{\text{het}} = \Omega_{\text{hom}}^{[w]} + \Omega_{\text{hom}}^{[s]} + \Delta\Omega \quad (2.39)$$

where from (2.36)

$$\Omega_{\text{hom}}^{[u]} = n_u n_y \psi_u, \quad u = s, w \quad (2.40)$$

and from (2.37)

$$\psi_u = 2(\omega_1^u + \epsilon_{\text{ff}} \hat{s}_1^u \hat{s}_1^u) + (n_z - 2)\omega_0^u + \epsilon_{\text{ff}} \hat{s}_0^u \hat{s}_0^u - 2\epsilon_{\text{ff}} \hat{s}_0^u \hat{s}_1^u, \quad u = s, w. \quad (2.41)$$

$\Omega_{\text{hom}}^{[s]}$ and $\Omega_{\text{hom}}^{[w]}$ are the grand potentials of the lattice gas between strongly attractive substrates of width n_s and weakly attractive substrates of width $n_w = n_x - n_s$, respectively. Note that the regions of the composite module now carry two indices, one denoting the strength of the attraction (w or s) and the other denoting the particular slab of the “homogeneous” module (0 referring to the central slab and 1 to the outer slabs).

The correction in (2.39) can be derived as follows. We must first create surfaces by breaking bonds between nearest neighbors across a plane (parallel with the y - z -plane) in the “homogeneous” module. This process increases

Ω by the amounts $n_y \epsilon_{\text{ff}} [2\hat{s}_1^u \hat{s}_1^u + (n_z - 2) \hat{s}_0^u \hat{s}_0^u]$ for weak ($u = w$) and strong ($u = s$) substrates. We must then join the strong and weak “homogeneous” modules by forming bonds across the interfaces. This joining decreases H^{LG} by $n_y \epsilon_{\text{ff}} [2\hat{s}_1^w \hat{s}_1^s + (n_z - 2) \hat{s}_0^w \hat{s}_0^s]$. Thus, the total grand potential for the “heterogeneous” module can be expressed

$$\Omega_{\text{het}} = n_y [n_s \psi_s + n_w \psi_w + \chi_{ss} + \chi_{ww} - 2\chi_{sw}] \quad (2.42)$$

where

$$\begin{aligned} \chi_{uu} &= \epsilon_{\text{ff}} [2\hat{s}_1^u \hat{s}_1^u + (n_z - 2) \hat{s}_0^u \hat{s}_0^u], \quad u = s, w \\ \chi_{sw} &= \epsilon_{\text{ff}} [2\hat{s}_1^w \hat{s}_1^s + (n_z - 2) \hat{s}_0^w \hat{s}_0^s] \end{aligned} \quad (2.43)$$

A consequence of the lower symmetry of the prototype is a larger number of possible morphologies. Inspection of (2.41)–(2.43) reveals that the grand potential is determined by the set $\mathcal{M} := \{\hat{s}_0^w, \hat{s}_0^s, \hat{s}_1^w, \hat{s}_1^s\}$, where each block occupation number can independently assume the value 0 or 1. Thus, 16 different morphologies are possible *in principle* according to (2.27). This fairly large number can be reduced substantially on physical grounds (i.e. by taking into account the relative magnitudes of ϵ_{fs} , ϵ_{fw} , and ϵ_{ff}). For example, if both ϵ_{fs} and ϵ_{fw} are small compared to ϵ_{ff} , the morphology characterized by $\mathcal{M} = \{0, 0, 1, 1\}$ is physically not sensible because it refers to a situation where sites at which the lattice gas is exposed to a reduced total attraction (i.e., in the immediate vicinity of the substrate) are occupied whereas energetically more favorable $(n_z - 2)$ bulk sites remain empty. By similar considerations most of the remaining morphologies can be ruled out, without the necessity of actually calculating their grand potentials.

2.2.3 Thermodynamically stable morphologies at $T=0$

The analysis of potentially possible morphologies of the prototype in section 2.2.2 can now be employed to construct the phase diagram at $T = 0$. Henceforth we employ the customary dimensionless units (distance in units of ℓ , energy in units of ϵ_{ff} , temperature in units of ϵ_{ff}/k_B). As an example we consider the case $n_s = n_w = 10$ ($n_x = 20$), $n_z = 10$, $\epsilon_{\text{fw}} = 0.0$, and $0.0 \leq \epsilon_{\text{fs}} \leq 2.0$. With the aid of figures 2.5 and 2.6 it can be seen that the only physically

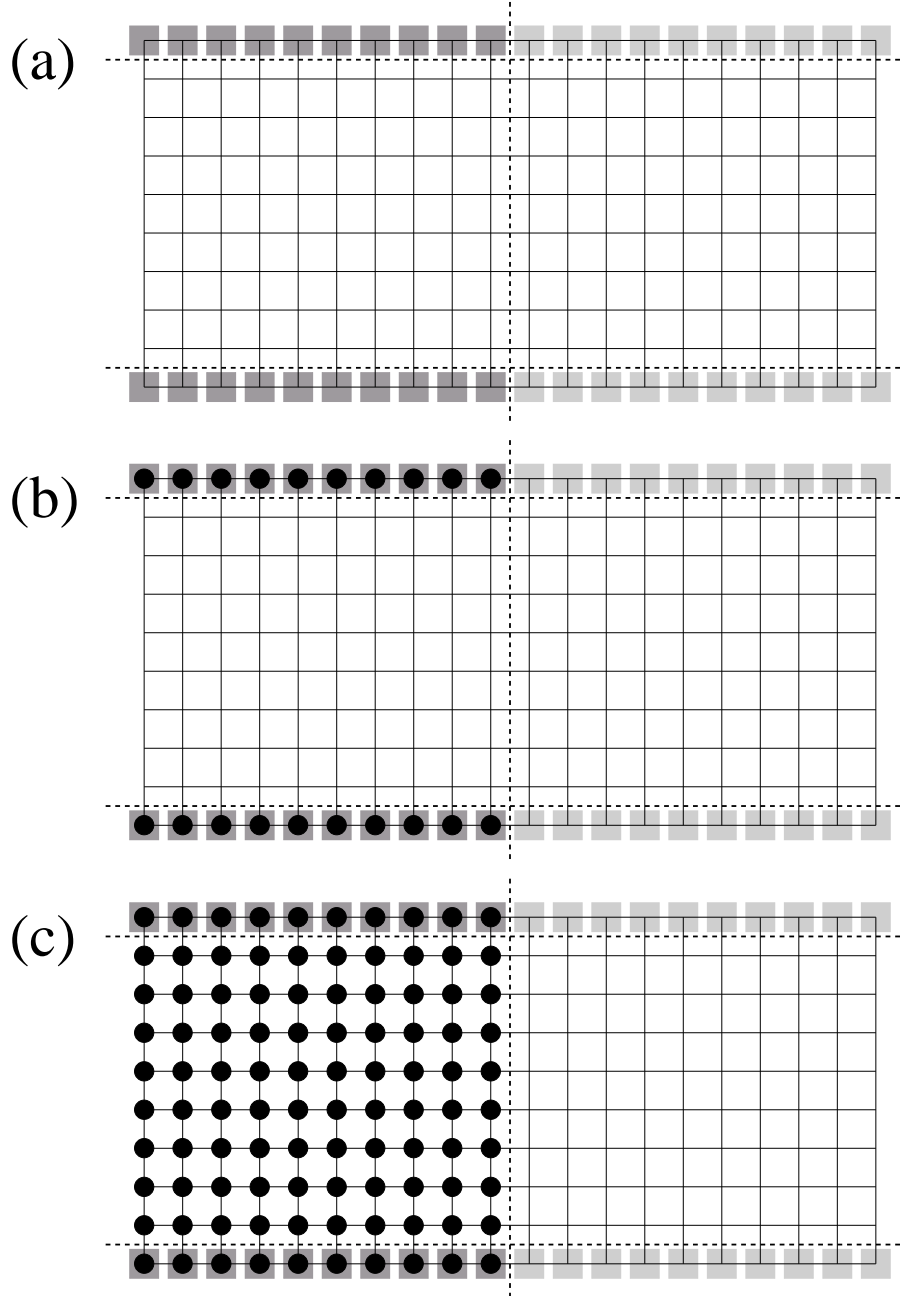


Figure 2.6: Subset of morphologies of the prototype $\mathcal{M} := \{\hat{s}_0^w, \hat{s}_0^s, \hat{s}_1^w, \hat{s}_1^s\}$. Black dots indicate occupied sites. a) gas $\mathcal{M}^g = \{0, 0, 0, 0\}$, b) droplet $\mathcal{M}^d = \{0, 0, 0, 1\}$, c) bridge $\mathcal{M}^b = \{0, 1, 0, 1\}$, d) vesicle $\mathcal{M}^v = \{1, 1, 0, 1\}$, e) liquid $\mathcal{M}^l = \{1, 1, 1, 1\}$

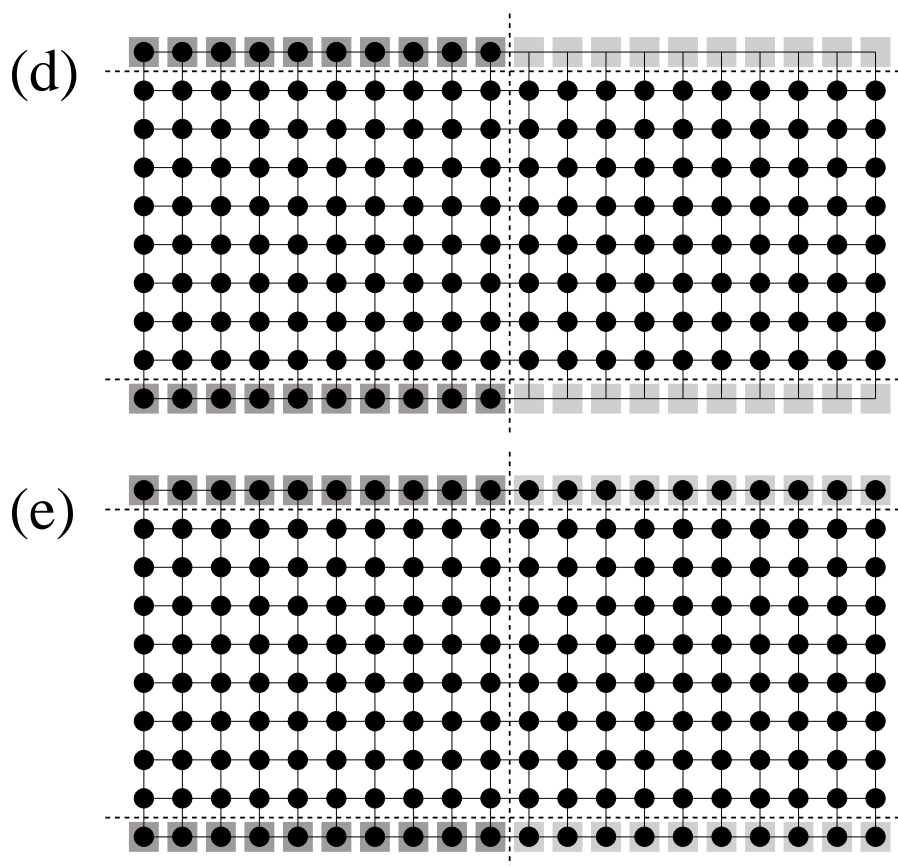


Figure 2.6: (Continued)

sensible morphologies are characterized by $\mathcal{M}^g = \{0, 0, 0, 0\}$ [empty lattice, i.e. “gas” morphology, figure 2.6(a)], $\mathcal{M}^l = \{1, 1, 1, 1\}$ [full lattice, i.e. “liquid” morphology, figure 2.6(e)], $\mathcal{M}^d = \{0, 0, 0, 1\}$ [liquid-filled lanes stabilized by the strongly adsorbing stripes, i.e. “droplet” morphology, figure 2.6(b)], $\mathcal{M}^b = \{0, 1, 0, 1\}$ [fluid “bridge” morphology connecting strongly adsorbing stripes, figure 2.6(c)], and $\mathcal{M}^v = \{1, 1, 0, 1\}$ [gas-filled lanes immersed in high-density fluid, i.e. “vesicle” morphology, figure 2.6(d)].

Using (2.41), (2.42), and (2.43), we derive expressions for the grand potential of these morphologies. The trivial one is the “gas”, that is the empty lattice $\mathcal{M}^g = \{0, 0, 0, 0\}$, for which

$$\Omega^g(\mu) \equiv 0. \quad (2.44)$$

The simplest nontrivial morphology is the “droplet” $\mathcal{M}^d = \{0, 0, 0, 1\}$. Its grand

potential is given by

$$\Omega^d(\mu) = n_y \left[-2n_s \left(\frac{\nu-2}{2} + \mu \right) + 2 - 2n_s \epsilon_{fs} \right], \quad (2.45)$$

where $\nu (= 6)$ is the number of nearest neighbors (of the bulk). Eventually, a “bridge” morphology $\mathcal{M}^b = \{1, 0, 1, 0\}$ characterized by

$$\Omega^b(\mu) = n_y \left[-n_s n_z \left(\frac{\nu}{2} + \mu \right) + n_z + n_s - 2n_s \epsilon_{fs} \right] \quad (2.46)$$

may form connecting the strongly attractive stripes of the substrates along the z -direction. It is also conceivable that under favorable conditions a “vesicle” $\mathcal{M}^v = \{1, 1, 1, 0\}$ may exist. Its grand potential is given by

$$\Omega^v(\mu) = n_y \left[(2n_w - n_x n_z) \left(\frac{\nu}{2} + \mu \right) + 2 + n_x - 2n_s \epsilon_{fs} \right]. \quad (2.47)$$

Eventually, all lattice sites may be occupied to yield a morphology to which we refer as “liquid” $\mathcal{M}^l = \{1, 1, 1, 1\}$. The grand potential of this liquid is given by

$$\Omega^l(\mu) = n_y \left[-n_x n_z \left(\frac{\nu}{2} + \mu \right) + n_x - 2n_s \epsilon_{fs} - 2n_w \epsilon_{fw} \right]. \quad (2.48)$$

To construct the phase diagram we must identify the morphology having the lowest value of the grand potential for a specific chemical potential. Therefore we consider the grand-potential curve $\Omega^\alpha(\mu)$. Its slope is given by the partial derivative of the grand potential with respect to the chemical potential.

$$\left(\frac{\partial \Omega}{\partial \mu} \right)_{T=0} = - \sum_{i=1}^{\mathcal{N}} s_{i0} = N \leq \mathcal{N} \quad (2.49)$$

where N is the number of occupied sites. Evidently, N is independent of μ at $T = 0$. In other words, because each morphology is in its ground state, there are no density fluctuations (see also section 2.2.1) implying

$$\left(\frac{\partial^2 \Omega}{\partial \mu^2} \right)_{T=0} = 0 \quad (2.50)$$

which is also obtained directly from (2.49). Thus, for $T = 0$, $\Omega^\alpha(\mu)$ is a straight line with negative slope. Of course, because of (2.49) all grand potential curves may have different slopes and intersect the ordinate at different values $\Omega^\alpha(0)$, $\alpha = g, d, b, v, l$ (see figure 2.7).

The phase having the lowest value of Ω for a given μ is thermodynamically stable (all other parameters fixed). Two morphologies are coexisting phases at

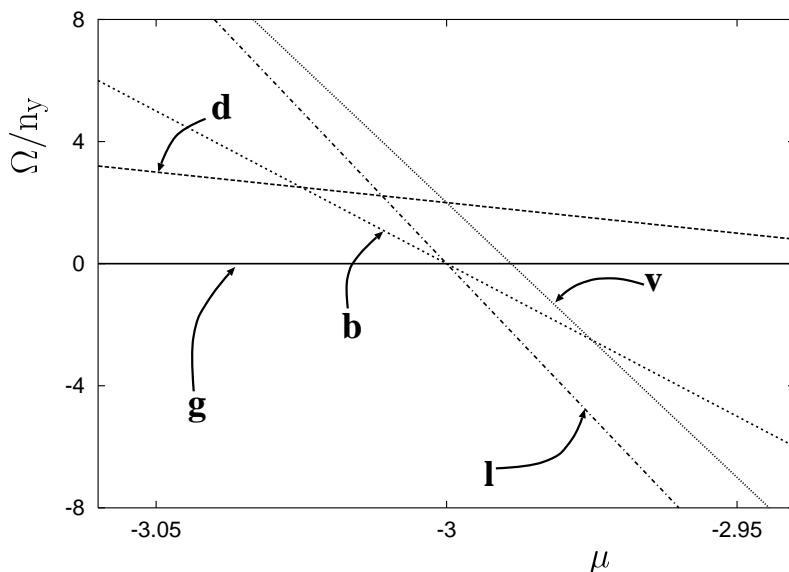


Figure 2.7: Line density of the grand potential $\Omega^\alpha(\mu)/n_y$ versus chemical potential μ for various morphologies $\alpha = g$ (gas), d (droplet), b (bridge), v (vesicle), and l (liquid) indicated in the figure. For all systems $\epsilon_{fs} = 1.0$, $\epsilon_{fw} = 0.0$, $T = 0$.

a chemical potential $\mu_x^{\alpha\beta}$ obtained as a solution of

$$\Omega^\alpha(\mu_x^{\alpha\beta}) = \Omega^\beta(\mu_x^{\alpha\beta}), \quad (2.51)$$

where $\Omega^{\alpha,\beta}(\mu_x^{\alpha\beta})$ is the absolute minimum of the grand potential for the given temperature. Figure 2.7 shows $\Omega^\alpha(\mu)/n_y$ obtained from (2.44)-(2.48). If μ is sufficiently low the gas morphology is thermodynamically stable. At $\mu^{gl} = -3$, $\Omega^g(\mu^{gl})$ intersects with $\Omega^l(\mu^{gl})$ where $\mu^{gl} = \mu_x^{gl}$ is a solution of (2.51). Beyond that intersection the liquid is thermodynamically stable. Moreover, at μ_x^{gl} , Ω^b is equal to both Ω^g and Ω^l . Thus, we have three-phase-coexistence at $\mu_x^{gl} \equiv \mu_{tr}^{gbl}$, defined by

$$\Omega^g(\mu_{tr}^{gbl}) = \Omega^b(\mu_{tr}^{gbl}) = \Omega^l(\mu_{tr}^{gbl}) \quad (2.52)$$

and therefore a triple point $\{T_{tr}^{gbl}, \mu_{tr}^{gbl}\}$. The “width” of the one-phase region of bridge morphologies vanishes for $T = 0$, that is it consists of the triple point only.

Based upon (2.49) and (2.50) and taking into account the different values of

$\Omega^\alpha(0)$ several characteristics of the phase behavior are readily deduced. From (2.44)-(2.48) it is obvious that $\Omega^g(\mu)$ has the largest slope of all grand potential curves. Thus, if one decreases the chemical potential sufficiently the gas will eventually become thermodynamically stable, i.e. the gas phase is stable over the region $-\infty < \mu \leq \mu_x^{g\alpha}$. Similarly the stability region of the liquid phase is given by $\mu_x^{\beta l} \leq \mu < +\infty$. In other words, for $T = 0$ the phase diagram always consists of stable gas and liquid regimes, with associated mean densities $\bar{\rho}^g = N^g/\mathcal{N} = 0$ and $\bar{\rho}^l = N^l/\mathcal{N} = 1$, respectively. Any other stable phase β must have a mean density $\bar{\rho}^\beta$ such that $\bar{\rho}^g < \bar{\rho}^\beta < \bar{\rho}^l$. The stability region of phase β is bounded by coexistence ‘‘points’’ $(\mu_x^{g\beta}, \mu_x^{\beta l})$ on both ‘‘sides’’. Extending this argument to more than 3 phases one realizes that phases associated with lower densities are stable at lower values of the chemical potential than higher-density phases. This behavior at $T = 0$ is universal and extendable to other lattice geometries.

From the explicit expressions for $\Omega^\alpha(\mu)$ given in (2.44)-(2.48) one can calculate $\mu^{\alpha\beta}$ analytically for all morphologies. Comparing the associated grand potentials at $\mu^{\alpha\beta}$ one identifies points of phase coexistence $\mu_x^{\alpha\beta}$ and therefore the range over which a given phase α is thermodynamically stable. Since each pair of grand-potential lines has exactly one intersection, 10 such intersections are possible for the 5 grand-potential curves given in (2.44)-(2.48). A subset is given by the following equations

$$\mu^{gd} = -2 + \frac{1}{n_s} - \epsilon_{fs} \quad (2.53)$$

$$\mu^{gb} = -3 + \frac{1}{n_s} + \frac{1}{n_z} - \frac{2}{n_z}\epsilon_{fs} \quad (2.54)$$

$$\mu^{gl} = -3 + \frac{1}{n_z} \frac{-2n_s\epsilon_{fs} - 2n_w\epsilon_{fw}}{n_x n_z} \quad (2.55)$$

$$\mu^{db} = -3 + \frac{1}{n_s} - \frac{1}{n_z - 2} \quad (2.56)$$

$$\mu^{dl} = -3 + \frac{(n_w - n_s) - 2(1 + n_w\epsilon_{fw})}{n_w n_z + n_s(n_z - 2)} \quad (2.57)$$

$$\mu^{bl} = -3 - \frac{1}{n_w} + \frac{1}{n_z} - \frac{2}{n_z}\epsilon_{fw} . \quad (2.58)$$

From (2.55) – (2.58) one notices that some of the expressions are independent of certain system parameters. For example, μ^{gb} in (2.54) does not depend on ϵ_{fw} and n_w . This is an important and useful result to understand the dependence of

the phase diagram on certain system parameters at higher temperatures ($T > 0$, see section 2.4).

2.3 Mean-Field Theory

In the preceding section the phase behavior of the prototype was analyzed based upon an analytical solution of the grand canonical ensemble partition function at $T = 0$. Unfortunately, for nonzero temperatures, such an exact solution is not known. Thus, there is no way to calculate the phase diagram of the prototype analytically for $T > 0$. However, several numerical techniques have been developed which can be employed in principle.

A direct (and formally exact) method is based upon Monte Carlo simulation. In Monte Carlo properties of the system of interest are calculated as ensemble averages over a sufficiently long Markov chain of configurations such that in the limit of an infinite number of configurations, these are distributed according to probability densities characteristic of the specific statistical physical ensemble in question. Calculating such quantities as the mean density or internal energy as functions of thermodynamic state variables, one may employ thermodynamic integration techniques to obtain the variation of, say, the grand potential along a suitably chosen path in thermodynamic state space. If these paths are chosen such that the *absolute* value of Ω can be calculated at the starting point, this procedure allows one to determine the phase behavior numerically as shown by Binder for the bulk Ising magnet in three dimensions [75].

However, there are essentially two drawbacks of this method. First, it is rather time consuming since several Monte Carlo simulations have to be carried out to determine *one* point on the phase diagram. This is particularly cumbersome for the prototype if one wishes to explore its phase behavior in the multidimensional space of model parameters. Second, and more importantly, thermodynamic integration works only if the path chosen in state space does not accidentally cross a line of first-order phase transitions at which ensemble averages change discontinuously by an a priori undetermined amount. This, in turn, implies that one needs to have at least a rough idea of the phase diagram prior to determining it by Monte Carlo. Since the discussion in section 2.2

indicated that a large number of phases may exist for the prototype even for nonzero temperatures, choosing a suitable path in state space beforehand seems hopeless.

An alternative to Monte Carlo simulations is to *approximate* Ω^{LG} in (2.7). To obtain such an approximation we utilize Bogoliubov’s theorem [76] which provides the possibility of finding the “best” approximation within a number of constraints imposed on the system in a controlled and transparent manner. This approach will be discussed in the following section.

2.3.1 Variational treatment of the mean field model

We begin again with the Hamiltonian of the nearest neighbor lattice gas given in equation (2.5). Let us also introduce the Hamiltonian of a system having no intermolecular attractions [nonattractive (NA) lattice gas, $\epsilon_{\text{ff}} = 0$, see (2.5)]

$$H^{\text{NA}} = - \sum_{i=1}^{\mathcal{N}} \mu_i^{\text{NA}} s_i \quad (2.59)$$

where μ_i^{NA} is the associated intrinsic chemical potential. Intermolecular repulsion is still accounted for because of the double-valued occupation numbers s_i [see (2.2)]. The purpose of (2.59) is to determine μ_i^{NA} such that the system of nonattracting lattice-gas molecules, which can be treated analytically at all temperatures, becomes the best approximation to the lattice gas *with* intermolecular interactions governed by H^{LG} in (2.5). To obtain this best approximation we employ Bogoliubov’s theorem.

Suppose a system with Hamiltonian H which can be split according to

$$H = H_0 + \Delta H \quad (2.60)$$

where H_0 is the Hamiltonian of a reference system and ΔH is difference between the latter and H . In the present context we identify H with H^{LG} and take the nonattractive lattice gas as reference system ($H_0 = H^{\text{NA}}$). Therefore ΔH accounts for attractive interactions between lattice-gas molecules. Let us define

$$H(\lambda) = H^{\text{NA}} + \lambda \Delta H \quad , \quad 0 \leq \lambda \leq 1 \quad (2.61)$$

where $H(\lambda = 0) \equiv H^{\text{NA}}$ and $H(\lambda = 1) \equiv H^{\text{LG}}$. Thus, by increasing the value of the dimensionless coupling parameter λ from 0 to 1 (“turning on” the

perturbation ΔH) one can vary $H(\lambda)$ smoothly between H^{NA} and H^{LG} . The grand potential of a system governed by $H(\lambda)$ is given by

$$-\beta\Omega(\lambda) = \ln \Xi = \ln \sum_{\mathbf{s}} \exp[-\beta H(\mathbf{s}, \lambda)] \quad . \quad (2.62)$$

Let us now differentiate (2.62) to obtain

$$\begin{aligned} \frac{d\Omega(\lambda)}{d\lambda} &= \Xi^{-1} \sum_{\mathbf{s}} \Delta H \exp[-\beta H(\mathbf{s}, \lambda)] \\ &= \langle \Delta H \rangle_{\lambda} \end{aligned} \quad (2.63)$$

and

$$\frac{d^2\Omega(\lambda)}{d\lambda^2} = -\beta \left\langle (\Delta H - \langle \Delta H \rangle_{\lambda})^2 \right\rangle_{\lambda} \leq 0 \quad \forall \lambda \quad (2.64)$$

which is negative semidefinite for all λ . Thus, $\Omega(\lambda)$ is concave for $0 \leq \lambda \leq 1$. Since the perturbation ΔH is assumed to be small, we approximate $\Omega(\lambda)$ by a Taylor series around $\lambda = 0$, that is

$$\Omega^{\text{LG}} \simeq \Omega^{\text{NA}} + \left(\frac{d\Omega(\lambda)}{d\lambda} \right)_{\lambda=0} \lambda + \dots \quad (2.65)$$

Because $\Omega(\lambda)$ is concave [see (2.64)], it follows that $\Omega(\lambda)$ lies below its tangent at $\lambda = 0$, that is the right side of (2.65) must always be larger or equal to Ω^{LG} . Thus, from (2.63) and (2.65) one arrives at the Bogoliubov inequality ($\lambda = 1$)

$$\Omega^{\text{LG}} \leq \Omega^{\text{NA}} + \langle \Delta H \rangle_{\lambda=0} \quad . \quad (2.66)$$

This last expression can be interpreted the following way. The exact grand potential of the system of interest, i.e. H^{LG} (perturbed system) is always lower or equal to the grand potential of the unperturbed system plus the perturbation (averaged over the states of the unperturbed system). Thus, $\Omega^{\text{NA}} + \langle \Delta H \rangle_{\lambda=0}$ is an upper bound of Ω^{LG} . For the present system we may therefore write

$$\Omega^{\text{LG}} \leq \Omega^{\text{NA}} + \langle H^{\text{LG}} - H^{\text{NA}} \rangle_{\lambda=0} \quad . \quad (2.67)$$

Now we are in a position to solve our initial problem, that is to determine the best choice of μ_i^{NA} in (2.59). Since the right side of (2.67) is an upper bound of Ω^{LG} we minimize $\Omega^{\text{NA}} + \langle H^{\text{LG}} - H^{\text{NA}} \rangle_{\lambda=0}$ with respect to μ_i^{NA} . To derive

expressions for Ω^{NA} and $\langle H^{\text{LG}} - H^{\text{NA}} \rangle_{\lambda=0}$ as functions of μ_i^{NA} we start from

$$\begin{aligned} \Xi^{\text{NA}} &= \sum_{\mathbf{s}} \exp \left(\beta \sum_{i=1}^{\mathcal{N}} \mu_i^{\text{NA}} s_i \right) \\ &= \prod_{i=1}^{\mathcal{N}} \sum_{s_i=0}^1 \exp(\beta \mu_i^{\text{NA}} s_i) = \prod_{i=1}^{\mathcal{N}} [1 + \exp(\beta \mu_i^{\text{NA}})] \end{aligned} \quad (2.68)$$

where the second line follows from absence of attractive interactions between molecules located at different sites. The grand potential is then given by [see (2.62)]

$$\Omega^{\text{NA}} = -\beta^{-1} \ln \Xi^{\text{NA}} = -\beta^{-1} \sum_{i=1}^{\mathcal{N}} \ln [1 + \exp(\beta \mu_i^{\text{NA}})] \quad (2.69)$$

From (2.5) and (2.59) we calculate

$$\begin{aligned} \langle H^{\text{LG}} - H^{\text{NA}} \rangle_{\lambda=0} &= \left\langle -\frac{\epsilon_{\text{ff}}}{2} \sum_{i=1}^{\mathcal{N}} \sum_j^{\nu_i} s_i s_j - \sum_{i=1}^{\mathcal{N}} (\mu_i^{\text{LG}} - \mu_i^{\text{NA}}) s_i \right\rangle_{\lambda=0} \\ &= -\frac{\epsilon_{\text{ff}}}{2} \sum_{i=1}^{\mathcal{N}} \sum_j^{\nu_i} \langle s_i s_j \rangle_{\lambda=0} - \sum_{i=1}^{\mathcal{N}} (\mu_i^{\text{LG}} - \mu_i^{\text{NA}}) \langle s_i \rangle_{\lambda=0} \\ &= -\frac{\epsilon_{\text{ff}}}{2} \sum_{i=1}^{\mathcal{N}} \sum_j^{\nu_i} \langle s_i \rangle_{\lambda=0} \langle s_j \rangle_{\lambda=0} - \sum_{i=1}^{\mathcal{N}} (\mu_i^{\text{LG}} - \mu_i^{\text{NA}}) \langle s_i \rangle_{\lambda=0} \\ &= -\frac{\epsilon_{\text{ff}}}{2} \sum_{i=1}^{\mathcal{N}} \sum_j^{\nu_i} \rho_i \rho_j - \sum_{i=1}^{\mathcal{N}} (\mu_i^{\text{LG}} - \mu_i^{\text{NA}}) \rho_i \end{aligned} \quad (2.70)$$

where the local densities are defined by $\rho_i \equiv \langle s_i \rangle_{\lambda=0}$. The third line of (2.70) follows because in the nonattracting system there are no intermolecular correlations

$$\langle s_i s_j \rangle_{\lambda=0} - \langle s_i \rangle_{\lambda=0} \langle s_j \rangle_{\lambda=0} = 0 \quad (2.71)$$

Since $\Omega^{\text{NA}} + \langle H^{\text{LG}} - H^{\text{NA}} \rangle_{\lambda=0}$ is a functional of μ_i^{NA} we seek solutions of the variational expression

$$\frac{\delta (\Omega^{\text{NA}} + \langle H^{\text{LG}} - H^{\text{NA}} \rangle_{\lambda=0})}{\delta \mu_i^{\text{NA}}} \stackrel{!}{=} 0 \quad (2.72)$$

Equation (2.72) determines the local density in terms of the optimum intrinsic chemical potential μ_i^{NA} of the corresponding nonattractive system, namely

$$\rho_i = \frac{1}{1 + \exp(-\beta \mu_i^{\text{NA}})} \quad (2.73)$$

which can be rearranged to give

$$\exp(-\beta \mu_i^{\text{NA}}) = \frac{\rho_i}{1 - \rho_i} \quad (2.74)$$

Inserting now (2.74) into (2.70) together with (2.67) gives us the optimized grand potential

$$\begin{aligned} \Omega^{\text{LG}} &\leq -\beta^{-1} \sum_{i=1}^{\mathcal{N}} [\rho_i \ln \rho_i + (1 - \rho_i) \ln(1 - \rho_i)] \\ &\quad - \frac{\epsilon_{\text{ff}}}{2} \sum_{i=1}^{\mathcal{N}} \sum_j^{\nu_i} \rho_i \rho_j - \sum_{i=1}^{\mathcal{N}} \mu_i^{\text{LG}} \rho_i \\ &=: \Omega^{\text{MF}} \end{aligned} \quad (2.75)$$

to which we refer as the grand potential in mean-field approximation, since it explicitly neglects intermolecular correlations [see (2.70)].

From (2.75) it is furthermore clear that Ω^{MF} is a functional of the local density. The discussion in [77] makes it clear that for given intrinsic chemical potential $\boldsymbol{\mu} := \{\mu_i\}$ (we shall drop the superscript “MF” henceforth to simplify notation) and fixed T , Ω is minimum if the set $\boldsymbol{\rho} := \{\rho_i\}$ corresponds to the local density at thermodynamic equilibrium. The latter can be determined as a solution of the variational expression

$$\frac{\delta \Omega[\boldsymbol{\rho}]}{\delta \rho_i} \stackrel{!}{=} 0 \quad (2.76)$$

from which we obtain a set of coupled transcendental equations (i.e., Euler-Lagrange equations), namely

$$\beta^{-1} \ln \frac{\rho_i}{1 - \rho_i} - \epsilon_{\text{ff}} \sum_j^{\nu_i} \rho_j - \mu_i = 0 \quad i = 1, \dots, \mathcal{N} . \quad (2.77)$$

The set of equations (2.77) can be solved numerically by applying an iterative procedure discussed in detail in appendix A.

2.3.2 Bulk phase diagram of the mean-field lattice gas

As an illustration and as a useful reference system we apply the above considerations to the bulk lattice gas where it is convenient to introduce the grand potential density

$$\omega = \frac{\Omega}{\mathcal{N}} \quad (2.78)$$

where \mathcal{N} is the “volume” (number of lattice sites). The bulk is characterized by $\Phi_i = 0$, $i = 1, \dots, \mathcal{N}$. We employ a simple cubic lattice so that $\nu_i = 6$ regardless

of the lattice site considered. Therefore, the bulk lattice gas is uniform, that is $\rho_i = \rho$, $i = 1, \dots, \mathcal{N}$. In that case (2.75) simplifies to

$$\omega(T, \rho) = T[\rho \ln \rho + (1 - \rho) \ln(1 - \rho)] - \frac{\nu}{2}\rho^2 - \mu\rho \quad (2.79)$$

where we have employed the same dimensionless units already introduced in section 2.2.3. Since ω is a function of the uniform density, (2.76) simplifies to

$$\left(\frac{\partial\omega}{\partial\rho}\right)_{T,\mu} \stackrel{!}{=} 0 \quad (2.80)$$

from which

$$T \ln \frac{\rho}{1-\rho} - \nu\rho - \mu = 0 \quad (2.81)$$

follows with the aid of (2.77). From stability considerations one knows, that any two systems are in thermodynamic equilibrium if their respective sets of intensive variables have the same values [78]. These equilibrium constraints can be utilized to determine coexisting states as follows. Let “ α ” and “ β ” denote different thermodynamic states whose intensive variables satisfy the equations

$$T^\alpha = T^\beta \quad (2.82)$$

$$\mu^\alpha = \mu^\beta \quad (2.83)$$

$$P^\alpha = P^\beta \quad (2.84)$$

where P stands for the pressure. Since we are exclusively concerned with isothermal conditions $T = T^\alpha = T^\beta$ is satisfied *a priori* and does no longer need to be listed explicitly. From (2.81) it is clear that bulk phases are characterized by their densities ρ . Thus, to identify coexisting phases (say, α and β), we are seeking densities ρ^α and ρ^β satisfying the constraints (2.83) and (2.84). From (2.81) we have

$$\mu(\rho) = T \ln \frac{\rho}{1-\rho} - \nu\rho. \quad (2.85)$$

or equivalently

$$\mu(x) = T \ln \frac{\left(\frac{1}{2} + x\right)}{\left(\frac{1}{2} - x\right)} - \nu \left(\frac{1}{2} + x\right). \quad (2.86)$$

where the transformation $\rho = x + 1/2$ is introduced to make symmetry properties of μ transparent. Moreover, we introduce

$$\mu'(x) := \mu(x) + \frac{\nu}{2} = T \left[\ln \left(\frac{1}{2} + x\right) - \ln \left(\frac{1}{2} - x\right) \right] - \nu x \quad (2.87)$$

which is an odd function of x . Suppose x^α and x^β solve (2.83). Then $-x^\alpha$ and $-x^\beta$ are solutions as well. In particular, x_*^α and x_*^β may be solutions where $x_*^\alpha = -x_*^\beta$. In this special case the two solutions are identical such that the far right side of (2.87) must be zero for symmetry reasons. Thus,

$$\mu(x_*^\alpha) = \mu(-x_*^\alpha) = -\frac{\nu}{2} . \quad (2.88)$$

To reduce the manifold of solutions of (2.83) we employ the pressure

$$P(\rho) = -\omega(\rho) = -T \ln(1 - \rho) - \frac{\nu}{2} \rho^2 \quad (2.89)$$

where we have used (2.79) and (2.85) to derive the far right side. Replacing ρ by x as before we obtain after some straightforward algebra

$$\begin{aligned} P(x) &= -T \left[\ln \frac{(\frac{1}{2} - x)}{(\frac{1}{2} + x)} + \ln \left(\frac{1}{2} + x \right) \right] - \left(\frac{\nu}{2} x^2 + \frac{\nu}{2} x + \frac{\nu}{8} \right) \quad (2.90) \\ &= \mu(x) + P(-x) + \frac{\nu}{2} \end{aligned}$$

where we have used (2.85) and (2.89) to arrive at the last line, which may be recast as

$$P(x) - \mu(x) = P(-x) + \frac{\nu}{2} . \quad (2.91)$$

This last expression satisfies the constraint (2.84) only if $\mu(x)$ is given by (2.88) so that only the single solution $x_*^\alpha = -x_*^\beta$ is compatible with both constraints (2.83) and (2.84). Thus, at coexistence

$$\mu_x^{\alpha\beta} = -\frac{\nu}{2} \quad (2.92)$$

and the phase diagram

$$\mu_x(T) = -\frac{\nu}{2} , \quad 0 \leq T \leq T_c \quad (2.93)$$

is a straight line parallel to the T -axis starting at $T = 0$ and ending at the critical temperature T_c to be specified shortly [see figure 2.8(b)]. From (2.85) and (2.92)

$$\mu(\rho) = T \ln \frac{\rho}{1 - \rho} - \nu \rho = -\frac{\nu}{2} \quad (2.94)$$

can be obtained immediately. Equation (2.94) has a trivial solution $\rho = 1/2$ as one can easily verify. For this solution to be thermodynamically stable

$$\left(\frac{\partial^2 \omega}{\partial \rho^2} \right)_T = \frac{T}{\rho(1 - \rho)} - \nu \geq 0 \quad (2.95)$$

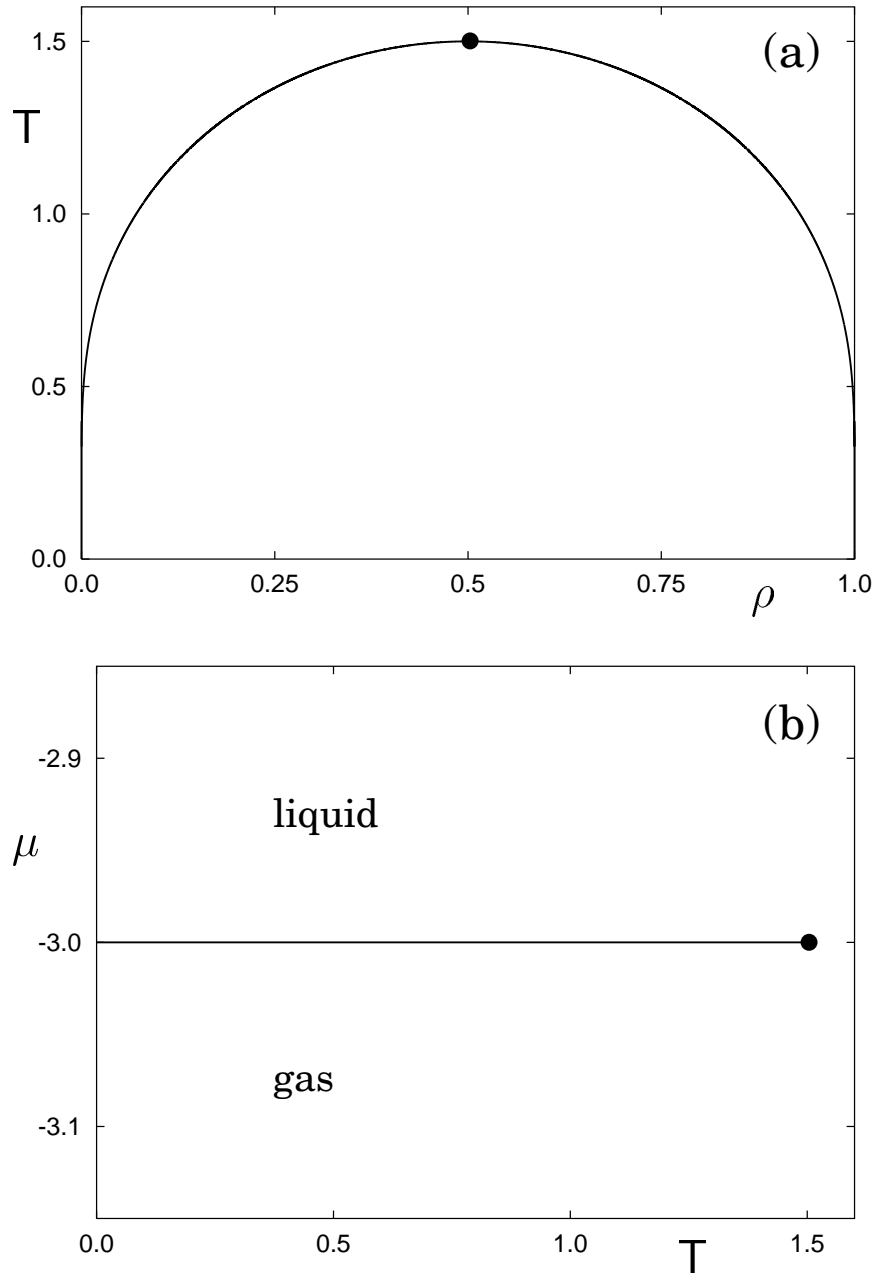


Figure 2.8: Bulk phase diagram: (a) T - ρ representation (b) μ - T representation. The critical point ($T_c = 3/2$, $\mu_c = -\nu/2 = -3$) is indicated by the black dot.

has to be satisfied. Rearranging (2.95) gives ($\nu = 6$)

$$T \geq |\nu\rho(1-\rho)|_{\rho=1/2} = \frac{3}{2} \quad (2.96)$$

where the equality holds for the critical temperature $T = T_c = 3/2$. Thus, $\rho = 1/2$ is a thermodynamically stable solution only if $T \geq T_c$. Since for $T = T_c$, $\rho = \rho_c = 1/2$ satisfies (2.80) and the equality in (2.95) simultaneously we associate with it the density at the bulk critical point. Hence, from (2.92), $\mu_c = -3$ is readily obtained. For $T < T_c$, $\rho = 1/2$ does not satisfy the inequality in (2.95) and therefore corresponds to a maximum of ω . Hence, the two other solutions x_*^α and x_*^β must correspond to minima of ω and therefore represent metastable morphologies or thermodynamically stable phases of the bulk lattice gas (see figure 2.8).

2.3.3 The limit $T=0$

An interesting limiting situation of the mean-field treatment is the limit of vanishing temperature ($T = 0$) where the lattice gas may be treated analytically according to the discussion in section 2.2.3. Let us begin by examining the bulk system ($\Phi_i = 0, \nu_i = \nu = 6$) whose equation of state is given by [see (2.81)]

$$T \ln \frac{\rho}{1-\rho} - \nu\rho - \mu = 0 \quad (2.97)$$

Setting μ to $\mu_x(T)$ [see (2.93)], (2.97) is an equation for the densities of coexisting phases. Unfortunately, (2.97) cannot be solved in closed form for ρ . Instead we apply a graphical method recasting (2.97) as

$$\rho = \frac{1}{\nu}(T\tilde{x} - \mu_x) \quad (2.98)$$

where we have introduced the definition

$$\rho =: \frac{1}{1 + \exp(-\tilde{x})} \quad (2.99)$$

Plotting (2.98) and (2.99) versus \tilde{x} for $T < T_c$ we find that (2.97) has three real roots $-\tilde{x}_0, 0$, and \tilde{x}_0 corresponding to the densities $1 - \rho_0, 1/2$ and ρ_0 , respectively. This result is in accordance with the one obtained in section 2.3.2, where we have also shown that $\rho = 1/2$ is an unstable solution of (2.97) below T_c . The remaining solutions must therefore be minima associated with coexisting

gas ($1 - \rho_0$) and liquid (ρ_0) phases. To determine the densities of the coexisting phases in the limit $T \rightarrow 0$ we replace $\mu_x(T)$ by $-\nu/2$ [see (2.93)]. After some straightforward algebraic manipulations this leads to

$$\tilde{x} = \nu \left(\rho - \frac{1}{2} \right) \frac{1}{T} \quad (2.100)$$

which shows that for $0 \leq \rho^g < 1/2$ (gas branch) \tilde{x} goes to negative infinity if T goes to zero. If, on the other hand, \tilde{x} is in the range $1/2 < \rho^l \leq 1$ (liquid branch) then \tilde{x} diverges to positive infinity. With the help of (2.99), which is temperature independent, one obtains

$$\lim_{T \rightarrow 0} \rho_0 = \begin{cases} 0 \\ 1 \end{cases} \quad (2.101)$$

If the chemical potential is *not* equal to the chemical potential at liquid gas coexistence, (2.100) must be written

$$\tilde{x} = (\nu\rho - \mu) \frac{1}{T}. \quad (2.102)$$

In that case

$$\lim_{T \rightarrow 0} \tilde{x} = \begin{cases} -\infty & , 0 \leq \rho \leq \mu/\nu \\ +\infty & , \mu/\nu \leq \rho \leq 1 \end{cases} \quad (2.103)$$

such that (2.101) is again recovered. Thus, in the limit of vanishing temperature the grand-potential density (2.79) simplifies to

$$\omega_0 \equiv \omega(T = 0) = -\frac{\nu}{3}\rho_0^2 + \mu\rho_0. \quad (2.104)$$

Because of (2.101), (2.104) is equivalent to

$$\omega_0 = -\frac{\nu}{3}s_0^2 + \mu s_0. \quad (2.105)$$

where the (mean) density has been replaced by the occupation number s_0 . We thus arrive at the gratifying result that, for the bulk system, the mean-field approximation of the lattice gas agrees with the exact result at $T = 0$ given in (2.28).

The above reasoning can be extended to the situation of primary interest, namely the prototype (see section 2.1.2) where the analogue of (2.97) is given by the Euler-Lagrange equations (2.77). Defining a parameter η_i

$$\eta_i := \mu_i + \sum_j^{\nu_i} \rho_j \quad (2.106)$$

(2.77) simplifies to

$$T \ln \frac{\rho_i}{1 - \rho_i} - 2\rho_i - \eta_i = 0. \quad (2.107)$$

Since (2.107) has exactly the same form as (2.97) for the bulk system, the same reasoning can be applied to conclude

$$\lim_{T \rightarrow 0} \rho_i = \rho_{0,i} = \begin{cases} 0 \\ 1 \end{cases} \quad i = 1, \dots, \mathcal{N} \quad (2.108)$$

meaning that all lattice sites are either filled or empty irrespective of the value of η_i . Thus, at $T = 0$ densities in (2.75) can be replaced by occupation numbers

$$\Omega_0 = - \sum_{i=1}^{\mathcal{N}} \sum_j^{\nu_i} s_{0,i} s_{0,j} - \sum_{i=1}^{\mathcal{N}} \mu_i s_{0,i} . \quad (2.109)$$

Again, this result is in accordance with the exact grand potential at vanishing temperature [see (2.21)]. The set of stable solutions of (2.109) or, equivalently (2.21), constitute the “morphologies” at $T = 0$. Thus, we have demonstrated that in the limit $T = 0$, the mean-field treatment becomes exact. This is also reflected by (2.23) because fluctuations vanish in that limit.

2.4 Phase behavior for $T > 0$

The mean-field approximation of the grand canonical potential introduced in the preceding section is now used to investigate the phase diagram of the confined lattice gas for $T > 0$.

2.4.1 Grand potential curves

By solving (2.77) numerically one obtains a set of equilibrium densities

$$\boldsymbol{\rho}^\alpha := \{\rho_1^\alpha, \rho_2^\alpha, \dots, \rho_N^\alpha\} \quad (2.110)$$

where the superscript α is introduced to indicate that for a given T and μ several solutions of (2.77) may exist. Using (2.75) we calculate values $\Omega^\alpha = \Omega[\boldsymbol{\rho}^\alpha, T, \mu]$ under isothermal conditions. Similar to (2.49)

$$\left(\frac{\partial \Omega^\alpha(\mu)}{\partial \mu} \right)_{T > 0} = -N^\alpha(\mu) \leq 0 \quad (2.111)$$

where, unlike the case $T = 0$, N^α is no longer independent of μ . Thus, for $T > 0$ the grand-potential curves in figure 2.9 are characterized by a nonvanishing curvature. A measure of this curvature is the isothermal compressibility κ_T^α associated with ρ^α , that is

$$\left(\frac{\partial^2 \Omega^\alpha(\mu)}{\partial \mu^2}\right) = -\frac{(N^\alpha)^2}{\mathcal{N}} \kappa_T^\alpha < 0 \quad (2.112)$$

where the inequality is a consequence of thermodynamic stability [78], disregarding explicitly the “vacuum” (i.e., $\langle N \rangle = 0, \kappa_T = 0$). From the above consideration one realizes that the grand potential is a monotonically decaying function with slope $-N^\alpha(\mu)$ and a curvature determined by the isothermal compressibility. Coexisting phases are identified by intersections of grand-potential curves having the lowest value of Ω as detailed in section 2.2.3. Unfortunately, finding these intersections is complicated even in relatively simple systems since one has to make sure that one takes into account *all* solutions of (2.77). Appendix A presents a strategy to overcome this difficulty.

To investigate the effects of varying T we consider the case $\epsilon_{fw} = 0.0$ and $\epsilon_{fs} = 1.0$, where the interaction of a molecule with the “weak” stripe is purely repulsive (i.e., hard substrate) and the interaction with the “strong” stripe is characterized by $\epsilon_{fs} \equiv \epsilon_{ff}$. Thus, for molecules located at sites in the planes $z = 1$ and $z = n_z$, the interaction with the “strong” stripes exactly compensates the interaction with the nearest neighbor that has been lost on account of the creation of the “surfaces” of the hard-substrate module (section 2.2.2). Figure 2.9 presents grand potential curves at different temperatures. The figures show that $\{\Omega^\alpha(\mu)\}$ are only slightly bent. Curvature increases with increasing temperature, indicating a larger κ_T at higher T [see (2.112)]. Moreover, with increasing temperature one observes a pronounced shift to lower values of the grand potential. In addition, the number of stable phases and the total number of solutions of (2.77) varies with T as well. Figure 2.9(a) shows that for $T = 0$ a triple point $\mu_{tr}^{gbl} = -3$ exists at which gas, liquid and bridge phases coexist. Following the evolution of $\Omega^\alpha(\mu)$ one notices from the plot in figure 2.9(b) that for $T = 0.6$ the triple point has given way to a narrow one-phase region $-3.004 < \mu < -2.998$ in which bridge phases are thermodynamically stable. Hence, for $\{(T, \mu) | T = 0.6, \mu < -3.004\}$ gas phases are thermodynamically stable whereas this is the case for liquid phases over the

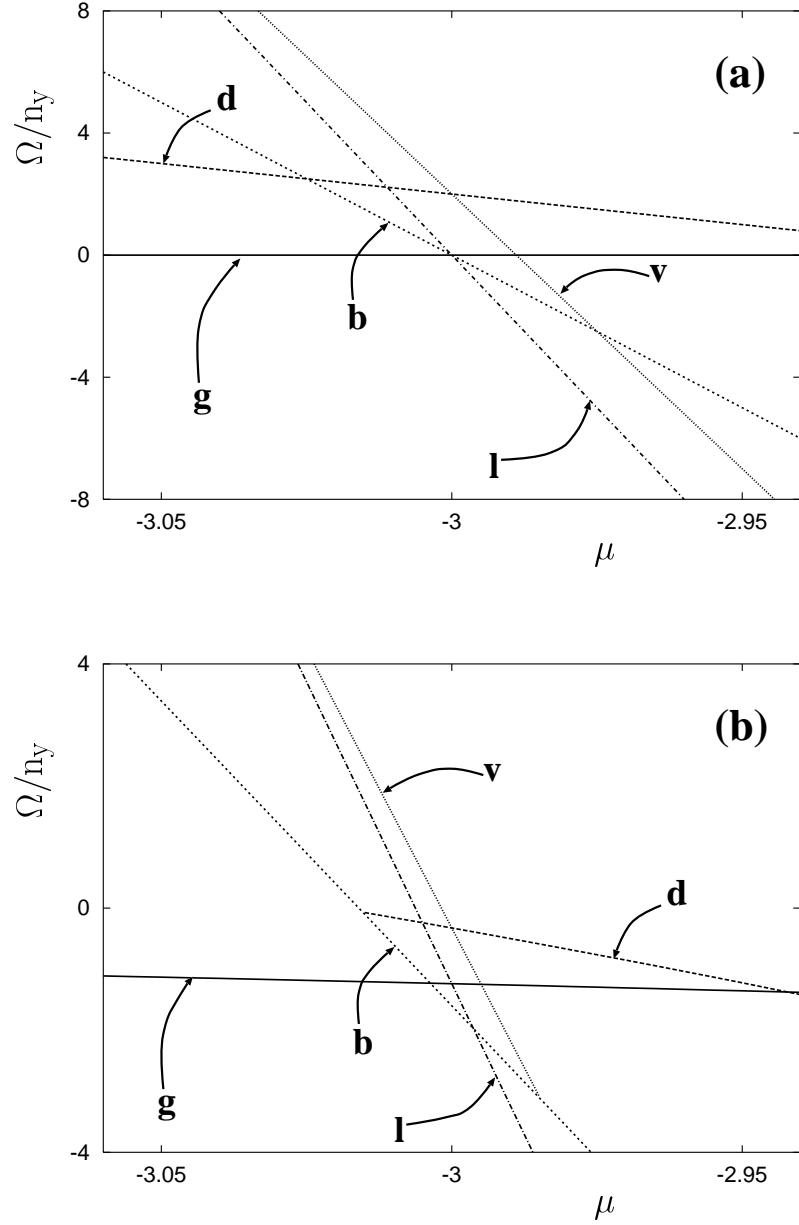


Figure 2.9: The grand potential $\Omega^\alpha(\mu)/n_y$ versus chemical potential μ for various morphologies $\alpha = g$ (gas), d (droplet), b (bridge), v (vesicle), and l (liquid) indicated in the figure. In all cases, $n_w = n_s = 10$ ($n_x = 20$), $n_z = 10$, $\epsilon_{fs} = 1.0$ and $\epsilon_{fw} = 0.0$. (a) $T = 0$ (for comparison), (b) $T = 0.6$, (c) $T = 0.9$, (d) $T = 1.2$.

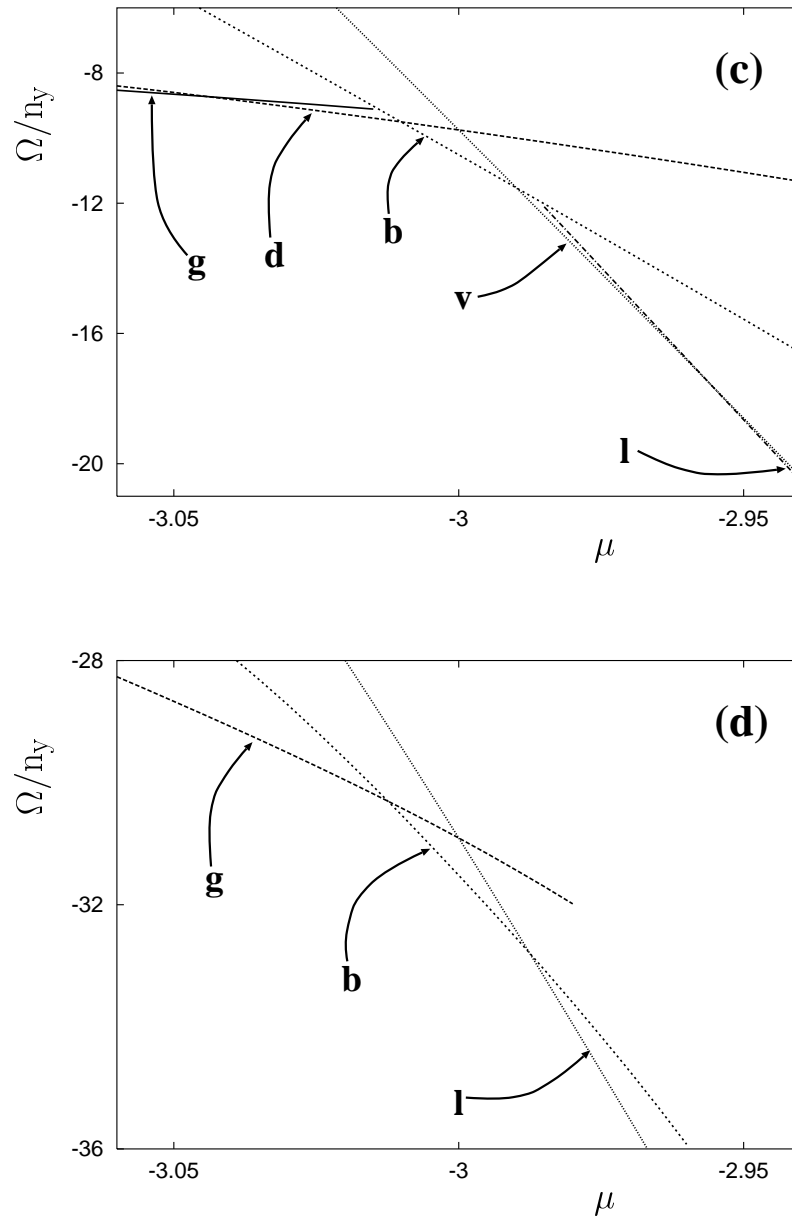


Figure 2.9: (Continued)

range $\{(T, \mu) | T = 0.6, \mu > -2.998\}$.

This picture changes substantially for $T = 0.9$ [figure 2.9(c)]. Now the gas phases are stable for thermodynamic states $\{(T, \mu) | T = 0.9, \mu < -3.044\}$. Over the range $\{(T, \mu) | T = 0.9, -3.044 < \mu < -3.010\}$ droplet morphologies ($\mathcal{M}^d = \{0, 0, 0, 1\}$ for $T = 0$) represent thermodynamically stable phases. At $\mu_x^{gd} = -3.044$ gas and droplet phases coexist. The region of bridge phases, $\{(T, \mu) | T = 0.9, -3.010 < \mu < -2.990\}$ has considerably widened compared with $T = 0.6$ [figure 2.9(b)]. Bridge and droplet phases coexist at $\mu_x^{db} = -3.010$ whereas bridge and vesicle phases ($\mathcal{M}^v = \{1, 1, 0, 1\}$ for $T = 0$) coexist at $\mu_x^{bv} = -2.990$. Vesicle phases are thermodynamically stable over the range $\{(T, \mu) | T = 0.9, -2.990 < \mu < -2.956\}$, eventually coexisting with liquid at $\mu_x^{vl} = -2.956$, which is then stable for all larger chemical potentials.

For the highest temperature $T = 1.2$ one deduces from figure 2.9(d) that only gas, bridge and liquid phases are thermodynamically stable over the respective ranges $\{(T, \mu) | T = 1.2, \mu < -3.013\}$, $\{(T, \mu) | T = 1.2, -3.013 < \mu < -2.988\}$, and $\{(T, \mu) | T = 1.2, \mu > -2.988\}$ where $\mu_x^{gb} = -3.013$ and $\mu_x^{bl} = -2.988$.

2.4.2 Phase diagrams

From the consideration of grand-potential curves in section 2.4.1 we are now in a position to determine lines of discontinuous phase transitions (i.e., coexistence lines) through the analogue of (2.51), that is

$$\Omega^\alpha [\mu_x^{\alpha\beta}(T)] = \Omega^\beta [\mu_x^{\alpha\beta}(T)] \quad (2.113)$$

where $\mu_x^{\alpha\beta}(T)$ stands for the coexistence line, that is the set of values of the chemical potential at which phases α and β coexist at a given temperature T . The phase diagram can then be represented by

$$\mu_x(T) = \bigcup_{\alpha, \beta} \mu_x^{\alpha\beta}(T), \quad \forall \alpha \neq \beta \quad (2.114)$$

that is, the union of all coexistence lines between all pairs of phases. Thus, one can perceive $\mu_x(T)$ as a “web” of coexistence lines, whose structure depends implicitly on system parameters ϵ_{fw} , ϵ_{fs} , n_w , n_s , and n_z . As these parameters vary, the web evolves. The next two paragraphs give an impression of the mean-field phase diagrams of a confined lattice gas. We especially focus on the

impact of the external potential of the prototype, which is characterized by the strength of attraction of the two different substrate parts denoted by ϵ_{fw} and ϵ_{fs} , respectively. We split the discussion into two parts. The first one focuses on the influence of ϵ_{fs} on the phase diagram while holding ϵ_{fw} fixed; the second one discusses the variation of ϵ_{fw} at fixed ϵ_{fs} .

The impact of ϵ_{fs} Figure 2.10 illustrates the impact of increasing attraction between the lattice gas and the “strong” stripe. For $\epsilon_{\text{fs}} = 0.5$, figure 2.10(a) reveals a tiny one-phase region for bridge phases indicated by the bifurcation in $\mu_{\text{x}}(T)$ at $T \simeq 1.375$. The coexistence lines involving bridge phases terminate at the respective critical temperatures $T_{\text{c}}^{\text{gb}} \simeq 1.461$ and $T_{\text{c}}^{\text{bl}} \simeq 1.440$. One also notes a bifurcation in $\mu_{\text{x}}(T)$ at $T \simeq 0.980$, indicating the existence of a vesicle phase. The vesicle-liquid coexistence line ends at its critical temperature $T_{\text{c}}^{\text{vl}} \simeq 1.005$.

Increasing the fluid-substrate interaction to $\epsilon_{\text{fs}} = 1.0$ [see figure 2.10(b)] causes $\mu_{\text{x}}(T)$ to move down to lower chemical potentials compared with the plot in figure 2.10(a). The gas-bridge-liquid triple point has also shifted all the way to $T = 0$ [see also figure 2.9(a)] so that the one-phase region of bridge phases is now much wider compared with the case $\epsilon_{\text{fs}} = 0.5$. At the same time T_{c}^{vl} has not changed at all but the coexistence line $\mu_{\text{x}}^{\text{vl}}(T)$ is longer now. However, a new bifurcation appears at $T \simeq 0.815$, corresponding to the appearance of a droplet phase that can coexist with gas or bridge phases. We note that the phase diagram is symmetric with respect to $\mu_{\text{c}} = -3$, as it must be on account of the symmetry of the grand potential.

For even larger $\epsilon_{\text{fs}} = 1.1$ one sees from figure 2.10(c) that the gas-bridge-liquid triple point vanishes, that is even for $T = 0$ a range of chemical potentials exists over which bridges are the thermodynamically stable phases. This effect results from a lowering of the temperature at which the “droplet” bifurcation occurs, along with a shift of $\mu_{\text{x}}^{\text{gb}}(T)$ and $\mu_{\text{x}}^{\text{gd}}(T)$ toward lower values of μ for $T < T_{\text{c}}^{\text{gd}}$. As before, however, all four critical temperatures remain unaltered.

A slight further increase of the strength of the fluid-substrate attraction to $\epsilon_{\text{fs}} = 1.2$ eventually causes $\mu_{\text{x}}^{\text{gd}}(T)$ to become detached from the other coexistence lines as the plot in figure 2.10(d) clearly shows. The remainder of the phase diagram appears to be unaffected by the increase of ϵ_{fs} . Consequently,

one finds three chemical potentials for $T = 0$ at which pairs of phases (i.e., gas–droplet, droplet–bridge, bridge–liquid) coexist. The one–phase region of droplet phases is already quite large. It increases further if the interaction of the lattice gas with the “strong” stripe is increased to $\epsilon_{fs} = 1.5$ [see figure 2.10(e)]. For this value of ϵ_{fs} one notices the appearance of a very short additional coexistence line beginning at $T_{tr}^{bd2} \simeq 1.001$ and $\mu \simeq -3.027$ with negative slope. An inspection of the local densities indicates that this coexistence line reflects layering transitions between droplet phases and new bilayer droplet phases (2) localized at the “strong” stripe. The layering transitions disappear at a critical temperature $T_c^{d2} \simeq 1.035$.

The impact of ϵ_{fw} Plots in figure 2.11 illustrate variations of $\mu_x(T)$ with increasing interaction between lattice gas and the “weak” stripe. Comparing figure 2.11(a) with figure 2.11(b) one notices that $\mu_x^{gd}(T)$ starting at $\mu = -3.400$ for $T = 0$ remains unaffected. However, the vesicle and layered phases, both visible in figure 2.11(a), disappear. At the same time the triple–point temperature corresponding to droplet–bridge–liquid coexistence is significantly raised to $T_{tr}^{dbl} \simeq 1.310$.

As ϵ_{fw} increases further to 1.0, plots in figure 2.11(c) show that $\mu_x^{gd}(T)$ is still unaffected. On the other hand, the bifurcation appearing in figure 2.11(b) apparently shifts to a temperature of about 0.817. However, an inspection of the phase diagrams in the equivalent T – ρ representation in figure 2.12(a) and figure 2.12(b) shows that the bifurcation temperature is actually not associated with bridge phases, which have already become metastable for this ϵ_{fw} [see figure 2.12(b)]. Instead the coexistence line branching off at $T_{tr}^{dml} \simeq 0.817$ corresponds to a line of discontinuous transitions between droplet phases and monolayer (m) phases adsorbed on the *entire* substrate [see figure 2.13(a), figure 2.13(b)] and may thus be regarded as a different type of layering transition triggered predominantly by the “weak” part of the substrate.

If $\epsilon_{fw} = 1.5$ the decorated substrate of the prototype degenerates to a chemically homogeneous one wetted by the lattice gas. In this case $\mu_x(T)$ consists of $\mu_x^{gm}(T)$ ending at $T_c^{gm} \simeq 1.018$ and $\mu_x^{ml}(T)$ terminating at its respective critical temperature $T_c^{ml} \simeq 1.452 < T_c^{bulk} = \frac{3}{2}$ on account of confinement where we use superscript “m” to indicate that the droplet phase has been replaced by

the monolayer as indicated by the representative plot of local density in figure 2.13(b). However, in the present case the local density in this monolayer no longer depends on x .

The phase diagrams presented in figure 2.11 exhibit yet another interesting characteristic. From that figure one immediately realizes that, for example, $\mu_x^{\text{gd}}(T)$ is almost independent of the special choice of ϵ_{fw} . This is also the case at $T = 0$. From the equation for the intersection point of the grand-potential curves of the gas and the droplet morphologies [see (2.53)]

$$\mu^{\text{gd}}(T = 0) = -\frac{2}{n_z}\epsilon_{\text{fs}} + \frac{1}{n_s} + \frac{1}{n_z} - \frac{\nu}{2} \quad (2.115)$$

it is obvious that $\mu^{\text{gd}}(T = 0)$ does not depend on ϵ_{fw} . The origin of this independence is, that lattice sites exposed to the weak parts of the fluid-wall potential i.e., (ϵ_{fw}) are not involved in the gas-droplet phase transition [see figure 2.6(a),(b)].

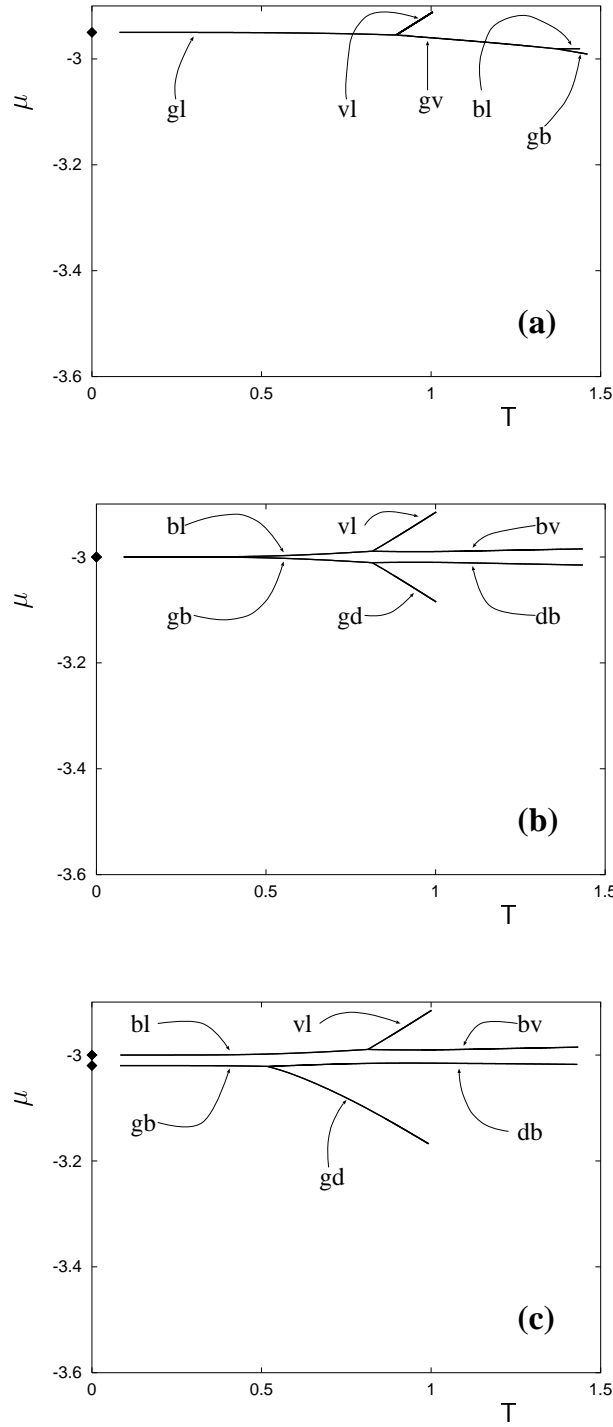


Figure 2.10: Phase diagrams in μ - T representation for $n_w = n_s = 10$ ($n_x = 20$), $n_z = 10$ and $\epsilon_{fw} = 0.0$ (a) $\epsilon_{fs} = 0.5$, (b) $\epsilon_{fs} = 1.0$, (c) $\epsilon_{fs} = 1.1$, (d) $\epsilon_{fs} = 1.2$, (e) $\epsilon_{fs} = 1.5$. (♦) analytical solution for $T = 0$.

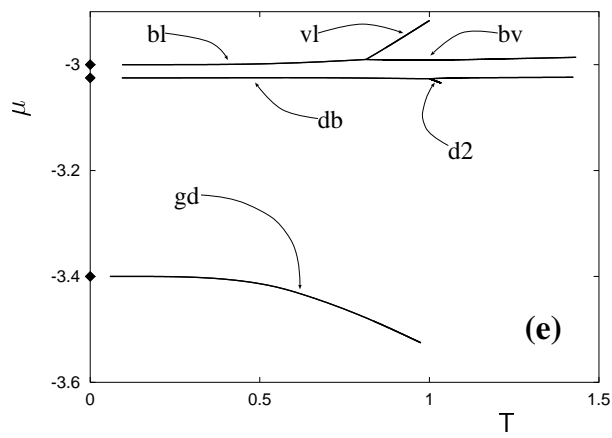
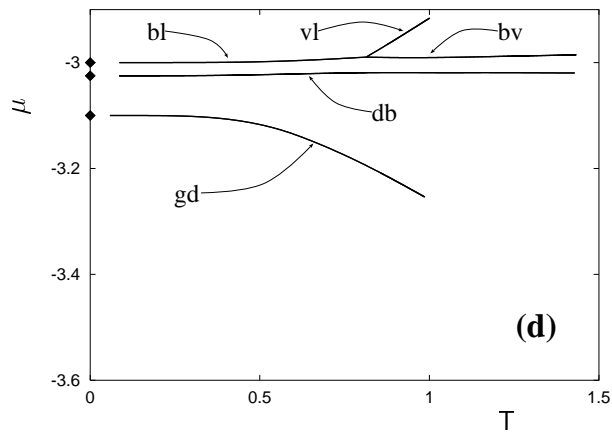


Figure 2.10: (Continued)

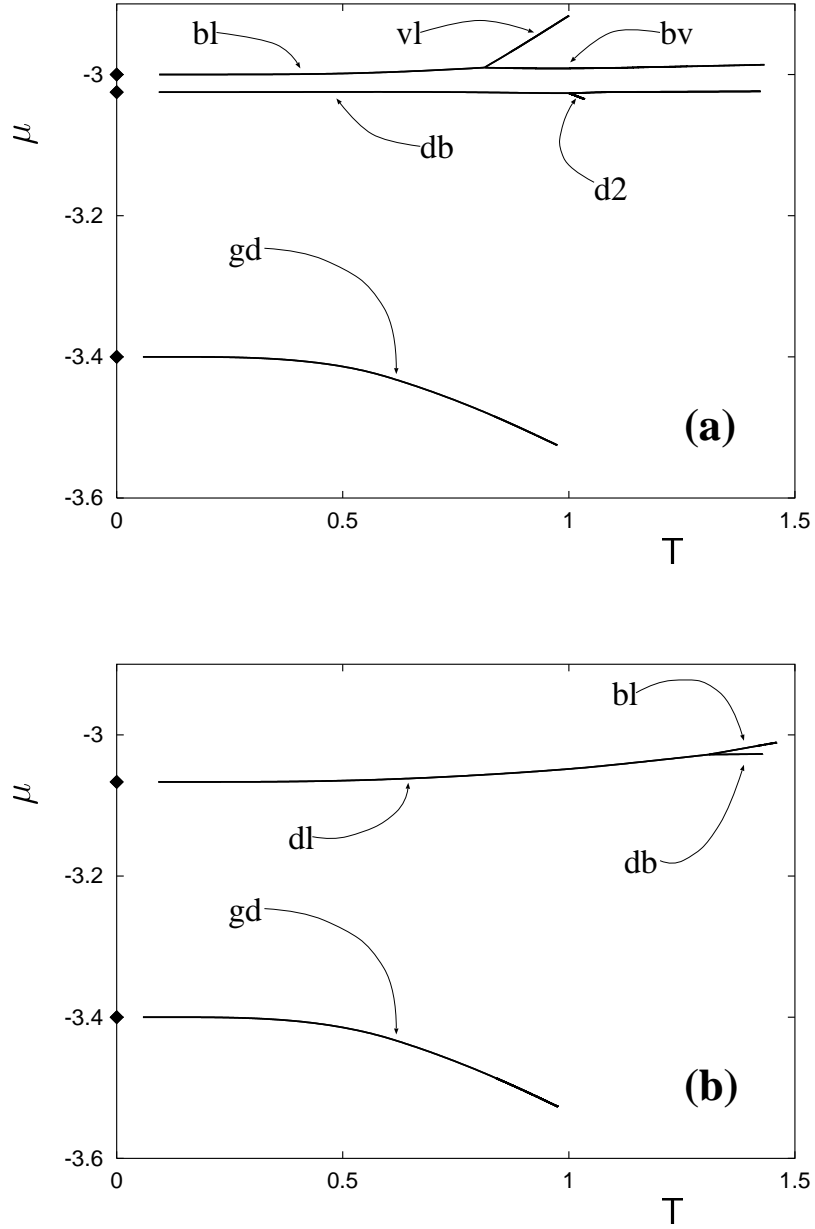


Figure 2.11: As figure 2.10, but for $\epsilon_{fs} = 1.5$. (a) $\epsilon_{fw} = 0.0$, (b) $\epsilon_{fw} = 0.5$, (c) $\epsilon_{fw} = 1.0$, (d) $\epsilon_{fw} = 1.5$. Open and filled circles in figure 2.11(c) signify thermodynamic states for which local densities are plotted in figure 2.13(a) and figure 2.13(b), respectively. (\blacklozenge) analytical solution for $T = 0$.

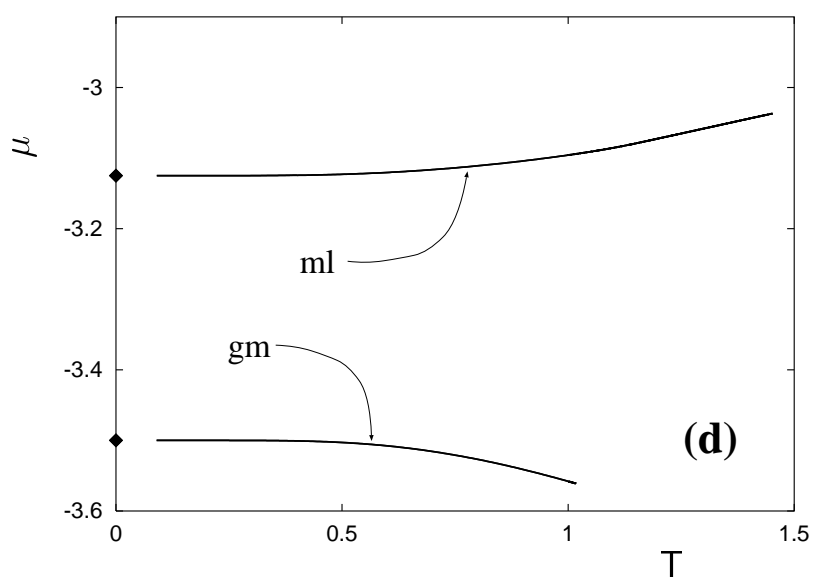
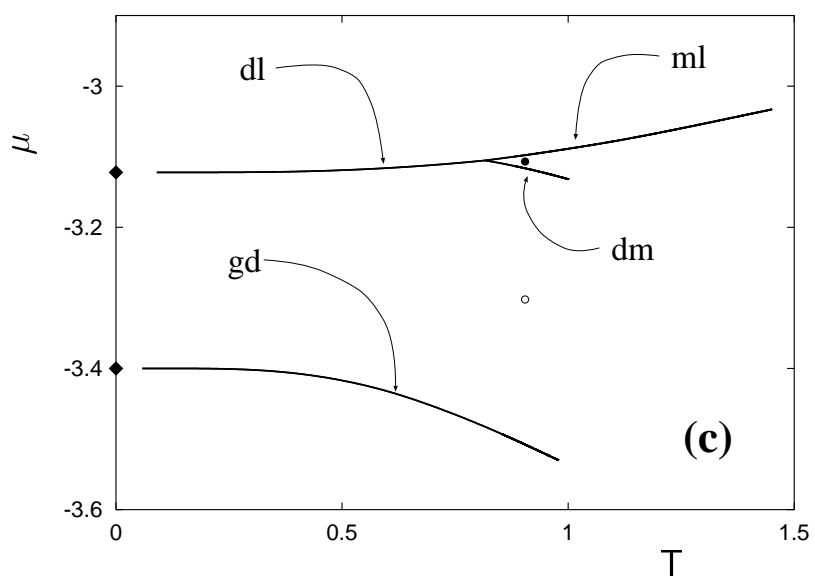


Figure 2.11: (Continued)

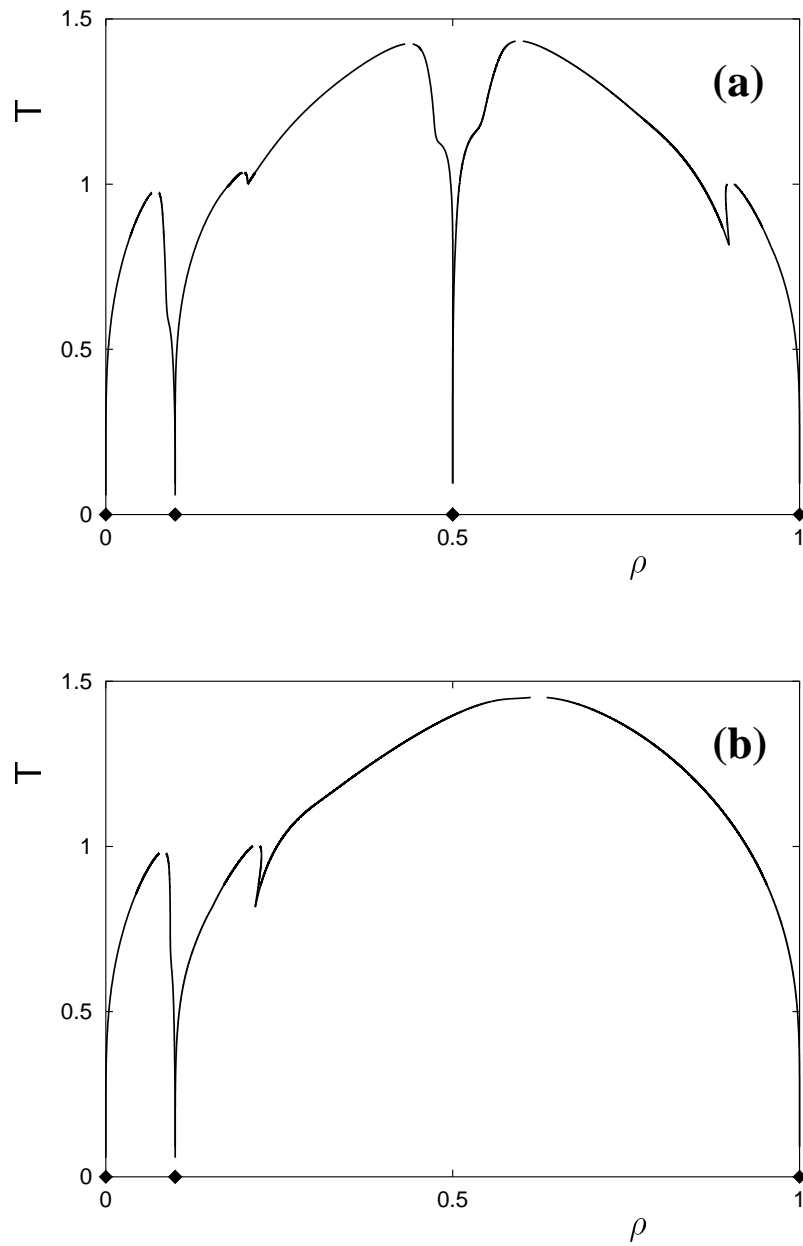


Figure 2.12: Phase diagrams in T - ρ representation for $\epsilon_{fs} = 1.5$. (a) $\epsilon_{fw} = 0.0$, (b) $\epsilon_{fw} = 1.0$ corresponding to figure 2.11(a) and figure 2.11(c), respectively. (\blacklozenge) analytical solution for $T = 0$. Note that in the immediate vicinity of the critical points the phase diagram could not be determined because of failure of numerical method to converge (see appendix A).

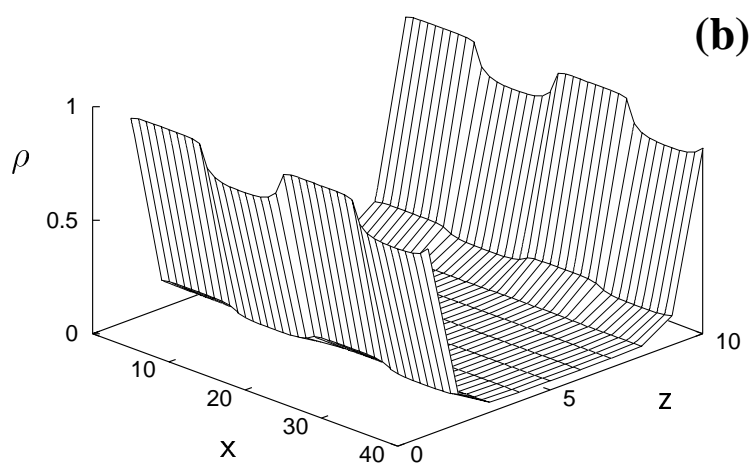
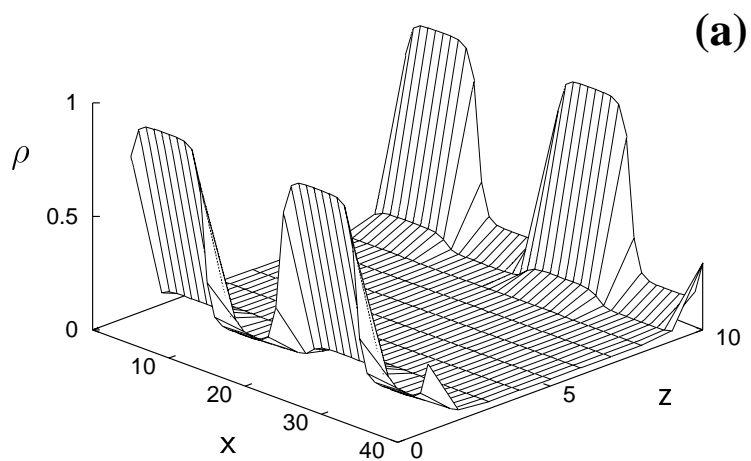


Figure 2.13: The local density $\rho(x, z)$ of lattice gases between prototypical chemically decorated substrates (see figure 2.1) where $\epsilon_{fw} = 1.0$, $\epsilon_{fs} = 1.5$, and $T = 0.9$ [see figure 2.11(c)]. (a) $\mu = -3.30$, (b) $\mu = -3.11$.

Chapter 3

The continuous model

In the preceding chapter we introduced the lattice gas as a convenient model to determine phase diagrams of fluids confined between chemically decorated surfaces at limited computational expense. However, the lattice-gas has several shortcomings. Its main disadvantage is perhaps the restriction of fluid molecules to discrete lattice sites. Thus, the maximum number of neighbors of a molecule is constant and the distance between nearest neighbors is fixed (and determined by the lattice structure). This is fairly unrealistic as far as real fluids are concerned, in which molecules move continuously in space. Moreover, we neglect correlations altogether within the mean-field approach employed in section 2.3.1. However, the latter may be abandoned in favor of more sophisticated treatments culminating eventually in more complex free-energy functionals than the one given in (2.75). On the other hand, the apparent simplicity of the present lattice-gas model offers the possibility of calculating phase diagrams with little computational effort. This is particularly useful because of the multidimensional parameter space $\{T, \mu, \epsilon_{fs}, \epsilon_{fw}, n_s, n_w, n_z\}$ governing the present model. However, to gain some insight into the impact of discreteness and the mean-field approximation it seems desirable to compare the lattice-gas results with those obtained for a continuous model incorporating intermolecular correlations.

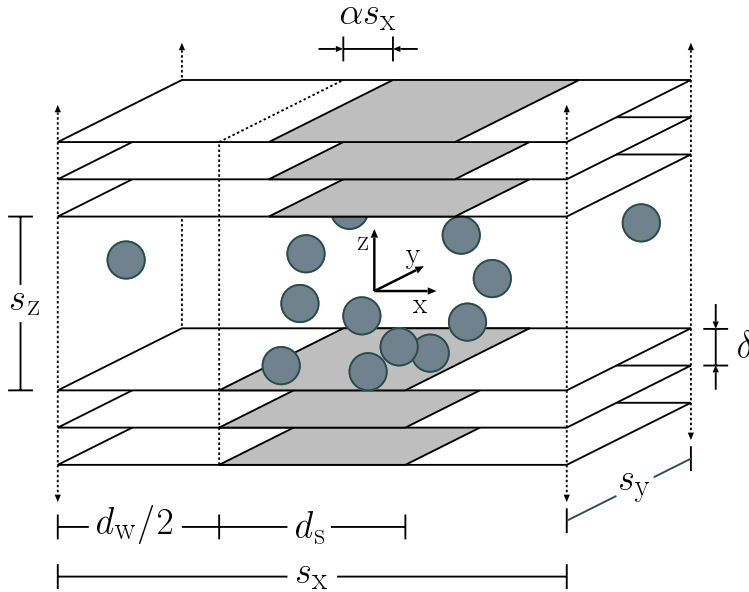


Figure 3.1: A schematic diagram of a simple fluid confined by a chemically heterogeneous model pore. Fluid molecules (gray spheres) are spherically symmetric. Each substrate consists of a sequence of crystallographic planes separated by a distance δ along the z -axis and comprises slabs of wall atoms interacting differently with fluid molecules. “Strong” and “weak” interactions are indicated by gray and white surface areas, respectively. The surface planes of the two opposite substrates are separated by a distance s_z and are misaligned by αs_x .

3.1 The continuous model

The continuous analogue of the lattice gas model (see section 2.1.2) consists of a fluid film composed of spherically symmetric molecules sandwiched between the surfaces of two solid substrates [79] (see figure 3.1). The substrate surfaces are planar, parallel to the x - y -plane and separated by a distance s_z along the z -axis of the coordinate system. We assume *all* interparticle interactions (fluid-fluid and fluid-substrate) to exhibit a distance dependence described by the Lennard-Jones LJ(12,6) potential

$$u(r) = 4\epsilon \left[\left(\frac{\sigma}{r} \right)^{12} - \left(\frac{\sigma}{r} \right)^6 \right] \quad (3.1)$$

where ϵ is the well depth, σ the molecular “diameter”, and r the distance between the centers of a pair of particles (fluid molecules or substrate atoms).

Since the substrates in our model are chemically heterogenous they are made of atoms of two chemical species differing in their respective interaction strength with the film molecules. Thus, in (3.1) $\epsilon \equiv \epsilon_{fs}$ ($u \equiv u_{fs}$) to indicate that the interaction of film molecules with substrate atoms is “strong” and $\epsilon \equiv \epsilon_{fw}$ ($u \equiv u_{fw}$) if the interaction is “weak”, respectively. We assume substrate atoms and film molecules to be of equal size, that is $\sigma = \sigma_{ff} = \sigma_{fs} = \sigma_{fw}$.

Each substrate comprises alternating slabs of atoms of the two species (see figure 3.1). The “strong” and “weak” slabs have widths d_s and d_w , respectively, in the x -direction, are semiinfinite in the z -direction, and infinite in the y -direction. The semiinfinite character in the z -direction is accounted for by an infinite number of crystallographic planes in the half space $s_z/2 \leq |z| < \infty$ separated by a distance δ (see figure 3.1). The substrates are thus periodic in x -direction of period $s_x = d_s + d_w$ and homogeneous in the y -direction along lines $x = \text{const}$, $z = \text{const}$. Substrate atoms are assumed to occupy the sites of the (100) plane of the face-centered-cubic (fcc) lattice. The lattice constant l is taken to be the same for both chemical species.

Since we are concerned with the effect of *chemical heterogeneity* at the nanoscale on the behavior of confined *fluids*, we expect details of the atomic structure not to matter greatly. Therefore, we adopt a mean-field representation of the fluid-substrate interaction [79], which we obtain by averaging u_{fs} and u_{fw} over positions of substrate atoms in the x - y -plane. The resulting coarse-grained potential can be expressed as

$$\begin{aligned} \Phi^{[k]}(x, z) = & n_A \sum_{m=-\infty}^{\infty} \sum_{m'=0}^{\infty} \int_{-\infty}^{\infty} dy' \left\{ \int_{-s_x/2+ms_x}^{-d_s/2+ms_x} dx' u_{fw}(|\mathbf{r} - \mathbf{r}'|) \right. \\ & \left. + \int_{-d_s/2+ms_x}^{d_s/2+ms_x} dx' u_{fs}(|\mathbf{r} - \mathbf{r}'|) + \int_{d_s/2+ms_x}^{s_x/2+ms_x} dx' u_{fw}(|\mathbf{r} - \mathbf{r}'|) \right\} \end{aligned} \quad (3.2)$$

where $n_A = 2/l^2$ is the areal density of the (100) plane of the fcc lattice and \mathbf{r} denotes the position of a film molecule. The position of a wall atom is given by $\mathbf{r}^0 = [x', y', z' + (-1)^k (s_z/2 + m'\delta)]$, where $k = 1, 2$ refers to lower and upper substrate, respectively. Thus, the sum over m' accounts for contributions to Φ from successive crystallographic planes, while the sum over m represents the infinite (periodic) extent of the substrates in $\pm x$ -direction.

Since the substrates comprise periodic heterogeneities in the x -direction we introduce αs_x as a quantitative measure of displacement of the upper substrate relative to the lower. The dimensionless registry parameter $0 \leq \alpha \leq 1/2$ is defined such that for $\alpha = 0$ the substrates are perfectly aligned, that is chemically identical parts of both substrates are exactly opposite each other; for $\alpha = 1/2$ the misalignment is maximum. Introducing the transformations

$$\begin{aligned} x' &\longrightarrow x'' = x - (k-1)\alpha s_x - x' & (3.3) \\ y' &\longrightarrow y'' = y - y' \\ z' &\longrightarrow z'' = z - z' + (-1)^k \left(\frac{s_z}{2} + m'\delta \right) \end{aligned}$$

and interchanging the order of integration, we can evaluate the integrals on the right side of (3.2) analytically [79]. After lengthy algebraic manipulations detailed in [79], one gets

$$\begin{aligned} \int_a^b dx' \int_{-\infty}^{\infty} dy' u(|\mathbf{r} - \mathbf{r}^0|) &= \frac{21\sigma}{32} I_3(x'', z''; d_s, s_x, s_z) \Big|_{x''=x-a}^{x''=x-b} & (3.4) \\ &\quad - \sigma I_4(x'', z''; d_s, s_x, s_z) \Big|_{x''=x-a}^{x''=x-b} \end{aligned}$$

where a and b represent the integration limits in (3.2). In (3.4)

$$I_3 := \frac{x'' \sigma^{10}}{9(z'')^2 \sqrt{R^9}} \left[1 + \frac{8}{7}S + \frac{48}{35}S^2 + \frac{64}{35}S^3 + \frac{128}{35}S^4 \right] , \quad (3.5)$$

$$I_4 := \frac{x'' \sigma^4}{3(z'')^2 \sqrt{R^3}} [1 + 2S] , \quad (3.6)$$

$$R := (x'')^2 + (z'')^2 , \quad (3.7)$$

and

$$S := \frac{R}{(z'')^2} . \quad (3.8)$$

Defining the function

$$\Delta(x'', z'') := \frac{21}{32} I_3(x'', z'') - I_4(x'', z'') \quad (3.9)$$

we can cast the fluid-substrate potential in final form as

$$\begin{aligned} \Phi^{[k]}(x, z) = & - \frac{3\pi}{2} n_A \sigma \sum_{m=-\infty}^{\infty} \sum_{m'=0}^{\infty} & (3.10) \\ & (\epsilon_{fw} - \epsilon_{fs}) \{ \Delta[x''_u(x, d_s), z''] - \Delta[x''_l(x, d_s), z''] \} \\ & + \epsilon_{fw} \{ \Delta[x''_u(x, s_x), z''] - \Delta[x''_l(x, s_x), z''] \} \end{aligned}$$

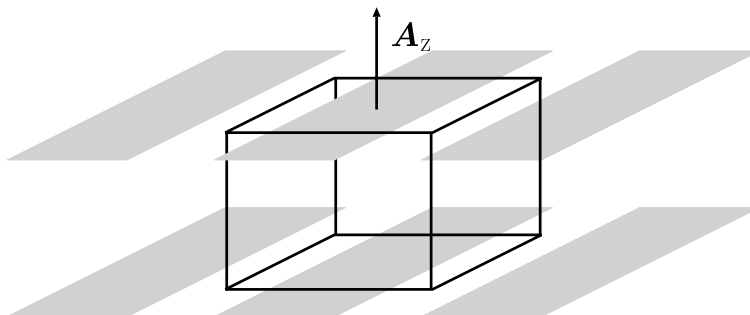


Figure 3.2: A schematic diagram of the fluid film confined by chemically striped substrates. The system of interest, i.e., the lamella is bounded by black lines. \mathbf{A}_z is also shown.(See also figure 3.1.)

where we simplified notation by introducing

$$x_1''(x, d) := x - (k-1)\alpha s_x - \frac{1}{2}d + ms_x \quad (3.11)$$

$$x_u''(x, d) := x - (k-1)\alpha s_x + \frac{1}{2}d + ms_x \quad (3.12)$$

and $d = d_s, s_x$, respectively.

3.2 Thermodynamics

Since equilibrium properties of confined fluids are the focal point of this thesis, (classical) thermodynamics provides the theoretical framework. To apply thermodynamics we have to distinguish between the thermodynamical *system* of interest and its *surroundings* (see figure 3.2). In addition we need to specify their interactions. Here we regard the system to be a finite piece (lamella) of the (infinite) film having dimensions $s_x \times s_y \times s_z$. The environment thus comprises the remainder of the infinite film plus the substrates. The system is bounded in the z -direction by two solid surfaces located at $z = \pm s_z/2$ and in lateral directions by planes at $x = \pm s_x/2$ and $y = \pm s_y/2$, respectively, since we place the origin of the coordinate system at the center of the lamella (see figure 3.1).

By moving the surface planes, which may be viewed as imaginary pistons, the fluid lamella can do work on its surroundings and vice versa. In general me-

chanical work dW_{mech} done by the system on its surroundings is given by

$$-dW_{\text{mech}} = \sum_j \mathbf{A}_j^T \cdot \mathbf{T} \cdot d\mathbf{\Delta}_j. \quad (3.13)$$

where the sum \sum_j in (3.13) extends over planes j having area $A_j = |\mathbf{A}_j|$ and a normal pointing in the j -direction (see figure 3.2). In 3.13, \mathbf{T} is the stress tensor (see chapter 13 in [80]), and $d\mathbf{\Delta}_j$ accounts for the (infinitesimal) displacement of plane j . In the absence of shear strains, \mathbf{T} is diagonal and can be represented by a 3×3 matrix. If on the other hand, a shear strain is applied in the x -direction, say,

$$-dW_{\text{mech}} = T_{xx}A_x ds_x + T_{yy}A_y ds_y + T_{zz}A_z ds_z + T_{zx}A_z d\alpha s_x. \quad (3.14)$$

where we assume the solid substrates to be rigid, so that they cannot be compressed or sheared. In the y -direction a shear strain cannot be applied, because the fluid-substrate potential is translationally invariant in that direction [see (3.10)].

Therefore reversible transformations of the lamella are governed by Gibbs' fundamental equation

$$dU = TdS + \mu dN - dW_{\text{mech}}. \quad (3.15)$$

All variables in (3.15) have their usual meaning: U is the internal energy, T is temperature, S entropy, μ chemical potential, and N the number of fluid molecules. Substituting dW_{mech} in (3.15) by (3.14) we rewrite Gibbs' fundamental equation (3.15) as

$$dU = TdS + \mu dN + T_{xx}A_x ds_x + T_{yy}A_y ds_y + T_{zz}A_z ds_z + T_{zx}A_z d\alpha s_x \quad (3.16)$$

where U depends on the set $\{S, N, s_x, s_y, s_z, \alpha s_x\}$ of natural variables.

However, other thermodynamic potentials will prove to be convenient for our purposes, because they depend on different sets of natural variables. A straightforward way of deriving these potentials is to start from a closed expression for U and replace its natural variables by successive Legendre transformations [81]. A closed form of U is always available if the system in question is homogeneous in at least in one spatial dimension. Take as an example a bulk fluid which is homogeneous in all three spatial dimensions. Therefore,

$$U(\lambda S, \lambda N, \lambda s_x, \lambda s_y, \lambda s_z) = \lambda U(S, N, s_x, s_y, s_z) \quad \lambda \in \mathbb{R}, \quad (3.17)$$

that is U is a homogeneous function of degree one of *all* its extensive variables. For the system of interest (3.17) is no longer valid because the confined fluid is subject to an external potential whose dependence on x and z causes the fluid to be inhomogeneous in general in these two directions [see (3.10) and figure 3.1]. Therefore, we replace (3.17) by

$$U(\lambda S, \lambda N, \lambda s_y) = \lambda U(S, N, s_y) \quad \lambda \in \mathbb{R} \quad (3.18)$$

where we have dropped s_x , s_z and αs_x keeping in mind that these strains are supposed to remain fixed. Equation (3.18) expresses the homogeneity of the fluid (i.e., the translational invariance of system properties) in the y -direction. Because U in (3.18) is a homogeneous function of degree one in its *remaining* extensive variables, we apply Euler's theorem [81] to obtain a Gibbs-Duhem equation

$$U(S, N, s_y) = \frac{\partial U}{\partial S} S + \frac{\partial U}{\partial N} N + \frac{\partial U}{\partial s_y} s_y = TS + \mu N + T_{yy} A_y s_y \quad (3.19)$$

where we have identified the partial differentials with the help of (3.16). The differential form of the Gibbs-Duhem equation is obtained by inserting (3.16) into the exact differential of (3.19), that is

$$0 = -SdT - Nd\mu + A_y s_y dT_{yy} + T_{xx} A_x ds_x + T_{zz} A_z ds_z + T_{zx} A_z d\alpha s_x \quad (3.20)$$

Equation (3.20) expresses the fact that of the six variables $\{T, \mu, T_{yy}, s_x, s_z, \alpha s_x\}$ only five may be varied independently in a reversible transformation of the confined fluid.

From (3.19) two other useful potentials can be derived. For example, the Legendre Transformation

$$\Omega = U - TS - \mu N = T_{yy} A_y s_y \quad (3.21)$$

defines the grand potential Ω , whose exact differential is given by

$$\begin{aligned} d\Omega(T, \mu, s_z, s_y, s_x, \alpha s_x) = \\ -SdT - Nd\mu + T_{xx} A_x ds_x + T_{yy} A_y ds_y + T_{zz} A_z ds_z + T_{zx} A_z d\alpha s_x \end{aligned} \quad (3.22)$$

where (3.16) has also been used. From (3.21)

$$\Psi = \Omega - T_{zz} A_z s_z = U - TS - \mu N - T_{zz} A_z s_z = (T_{yy} - T_{zz}) A_y s_y. \quad (3.23)$$

is introduced as the grand mixed isostress-isostrain potential, where from (3.23) and (3.22)

$$\begin{aligned} d\Psi(T, \mu, s_x, s_y, T_{zz}, \alpha s_x) = & \quad (3.24) \\ -SdT - Nd\mu + T_{xx}A_x ds_x + T_{yy}A_y ds_y + A_z s_z dT_{zz} + T_{zx}A_z d\alpha s_x & \end{aligned}$$

follows. This latter potential will turn out to be useful in section 3.3 where confined fluids are exposed to shear strains under fixed normal load, i.e. fixed T_{zz} .

3.3 Statistical Thermodynamics

Thermodynamic considerations detailed in the preceding paragraph led to closed expressions for both grand (3.21) and grand mixed isostress–isostrain potentials (3.23), that is expressions for Ω and Ψ in terms of stresses and conjugate strains. However, in order to use (3.21) or (3.23) molecular expressions for T_{yy} and T_{zz} are needed. That is, we are seeking expressions for stress tensor components in terms of the interaction potentials given in (3.1) and (3.10). This can be done within the framework of statistical thermodynamics which combines the notion of molecules and their properties with the principles of thermodynamics [76].

Consider the fluid lamella, introduced in section 3.2, at fixed T and μ . We assume the “shape” of the lamella to be fixed, that is s_x , s_y , and αs_x (see figure 3.1) remain constant. Let us furthermore consider the lamella to be under fixed normal load, i.e. we maintain T_{zz} in addition to the other variables. The thermodynamic state of the lamella can thus be specified by the set $\{T, \mu, s_x, s_y, T_{zz}, \alpha s_x\}$. In other words, the lamella is thermally and materially coupled to its environment and exchanges work due to compression (expansion) in the normal z -direction against a constant (external) load T_{zz} . This implies that the number of molecules N as well as the distance s_z between the confining walls may vary during the course of evolution of the lamella.

3.3.1 Partition function of the grand mixed isostress-is-strain ensemble

From a molecular perspective the lamella is assumed to be in a microstate specified by variables $\{s_z, N, j\}$ where j accounts for a collection of suitable quantum numbers necessary to specify the discrete microstate of energy $E(s_z, N, j)$ of a system containing N molecules confined by substrates separated by distance s_z . Since we are exclusively concerned with thermodynamic equilibrium, $E(s_z, N, j)$ can be obtained (at least in principle) by solving the (time-independent) Schrödinger equation [78], such that $|j\rangle$ is a stationary eigenstate of the N -molecule system. For sufficiently large N one can envisage a large number of microstates $\{s_z, N, j\}$ having energy $E(s_z, N, j)$ consistent with the macrostate of the lamella determined by $\{T, \mu, s_x, s_y, T_{zz}, \alpha s_x\}$. Consider now a large number of \mathcal{N} (virtual) replicas of the lamella each of which may be in one of the available microstates. The ensemble of replicas is perfectly isolated such that its total energy

$$E_t = \sum n(s_z, N, j)E(s_z, N, j) \quad (3.25)$$

is fixed. In (3.25), \sum stands for $\sum_{s_z} \sum_N \sum_j$ and $n(s_z, N, j)$ is the number of replicas in microstate j comprising N molecules between substrates separated by s_z , that is the occupation number of this microstate. Perfect isolation of the super-system of replicas (i.e., the ensemble) furthermore implies

$$\mathcal{N} = \sum n(s_z, N, j) \quad (3.26)$$

$$N_t = \sum n(s_z, N, j)N \quad (3.27)$$

$$A_z s_{z,t} = \sum n(s_z, N, j)A_z s_z \quad (3.28)$$

where N_t and $A_z s_{z,t}$ are the total number of molecules and total volume of the ensemble, respectively. From the above it is clear that there are many sets of occupation numbers (i.e., distributions) consistent with the four constraints (3.25)-(3.28). A particular distribution $\{n\}$ can be realized

$$W(\mathbf{n}) = \frac{\mathcal{N}!}{\prod_{s_z} \prod_N \prod_j n(s_z, N, j)!} \quad (3.29)$$

times. On account of perfect isolation of the ensemble the principle of equal *a priori* probabilities applies to all microstates [82]. Thus, we may define a mean

occupation number of a particular microstate as

$$\bar{n}_{s_z, N, j} = \frac{\sum_{\{\mathbf{n}\}} n(s_z, N, j) W(\mathbf{n})}{\sum_{\{\mathbf{n}\}} W(\mathbf{n})} \quad (3.30)$$

where the sums run over all distributions $\{\mathbf{n}\}$. Therefore, the probability of finding an arbitrarily selected replica in a specific microstate is given by

$$P_{s_z, N, j} = \frac{\bar{n}_{s_z, N, j}}{\mathcal{N}} = \frac{1}{\mathcal{N}} \frac{\sum_{\{\mathbf{n}\}} n(s_z, N, j) W(\mathbf{n})}{\sum_{\{\mathbf{n}\}} W(\mathbf{n})} . \quad (3.31)$$

To proceed beyond (3.31) we invoke as a key assumption the existence of a most probable distribution \mathbf{n}^* overwhelming all others such that the maximum-term method [83] applies and (3.31) can be recast as

$$P_{s_z, N, j} = \frac{n^*(s_z, N, j)}{\mathcal{N}} . \quad (3.32)$$

The assumption that no term except \mathbf{n}^* contributes to the sum in (3.31) is not per se justified. It may, however, be shown *a posteriori* that the distribution of \mathbf{n} around \mathbf{n}^* is essentially given by a δ -function provided $\mathcal{N} \rightarrow \infty$ [83]. This δ -function-like character of the distribution of \mathbf{n} can, on the other hand, be demonstrated independently invoking function-theoretical arguments put forward by Darwin and Fowler [84]. In this latter case no assumption concerning existence of \mathbf{n}^* is required.

Within the framework of the present approach, \mathbf{n}^* is the distribution of microstates maximizing $W(\mathbf{n})$, or equivalently $\ln W(\mathbf{n})$. By introducing a set of Lagrangian multipliers $\{\lambda_i\}$ we account for the constraints (3.25)-(3.28). Maximizing $\ln W(\mathbf{n})$ subject to the constraints (3.25)-(3.28) we eventually obtain

$$n_{s_z, N, j}^* = \exp(-\lambda_0) \exp(-\lambda_1 A_z s_z) \exp(-\lambda_2 N) \exp[-\lambda_3 E(s_z, N, j)] . \quad (3.33)$$

where the set $\{\lambda_i\}$ remains yet to be determined. Strictly speaking \mathbf{n}^* is the distribution making W extreme. However, on physical grounds it can be demonstrated that this extremum is indeed a maximum. Summing (3.33) over all microstates and utilizing (3.26) we can immediately replace λ_0 so that (3.32) becomes

$$P_{s_z, N, j} = \frac{1}{\chi} \exp[-\lambda_1 A_z s_z - \lambda_2 N - \lambda_3 E(s_z, N, j)] . \quad (3.34)$$

where

$$\chi := \sum \exp[-\lambda_1 A_z s_z - \lambda_2 N - \lambda_3 E(s_z, N, j)] \quad (3.35)$$

is the partition function of the grand mixed isostress-isostrain ensemble. Following Schoen [72] one may calculate the exact differential

$$d\langle E(s_z, N, j) \rangle = \sum [E(s_z, N, j) dP_{s_z, N, j} + P_{s_z, N, j} dE(s_z, N, j)]. \quad (3.36)$$

with aid of (3.34) and (3.35). After a sequence of tedious but straightforward manipulations detailed in [72] one may eventually compare (3.36) with Gibbs' fundamental equation (3.16) to arrive at

$$dU \equiv d\langle E(s_z, N, j) \rangle = \frac{1}{\lambda_3} dS + \frac{\lambda_1}{\lambda_3} A_z d\langle s_z \rangle + \frac{\lambda_2}{\lambda_3} d\langle N \rangle + dW \quad (3.37)$$

where dW is the work required to alter the shape of the lamella (see above). Comparison with (3.16) also permits one to deduce (see [83])

$$\lambda_3 \equiv \beta = \frac{1}{k_B T} \quad (3.38)$$

where k_B is Boltzmann's constant,

$$\lambda_2 = -\beta \mu \quad (3.39)$$

and

$$\lambda_1 = -\beta T_{zz} \quad (3.40)$$

With the help of these identification we obtain from (3.35) [72]

$$-k_B T \ln \chi = U - TS - T_{zz} A_z \langle s_z \rangle - \mu \langle N \rangle \quad (3.41)$$

so that by comparison with the thermodynamic equation (3.23)

$$-k_B T \ln \chi = \Psi \quad (3.42)$$

is derived as the desired expression relating the thermodynamic potential Ψ of the lamella to the properties of its individual molecules *via* χ .

3.3.2 The classical limit

So far the treatment of the grand mixed isostress-isostrain ensemble is quantum-mechanically exact. However, here we are concerned with classical fluids, that

is fluids in a temperature range such that typical intermolecular separations r_{ij} are large compared to the thermal de Broglie wavelength $\Lambda = (h^2/2\pi mk_B T)^{1/2}$ where h is Planck's constant and m is the mass of a fluid molecule. Under these conditions one may employ Kirkwood's method [78] to show that in (3.35)

$$\sum_j \exp(-\beta E(s_z, N, j)) \xrightarrow{\Lambda/r_{ij} \rightarrow 0} \frac{1}{h^{3N} N!} \int \int \exp[-\beta H(\mathbf{p}^N, \mathbf{q}^N)] d\mathbf{p}^N d\mathbf{q}^N \quad (3.43)$$

where

$$H = \sum_{i=1}^N \frac{\mathbf{p}_i^2}{2m} + U(\mathbf{r}^N, N, s_z) \quad (3.44)$$

is the classical Hamiltonian of an N -particle fluid and \mathbf{p}_i is the momentum of the i -th molecule. Because of (3.44), integration over momentum subspace in (3.43) can be carried out analytically to give [see (3.35)]

$$\chi = \sum_{s_z} \sum_N \exp(\beta T_{zz} A_z s_z) \exp(\beta \mu N) Q(s_z, N) \quad (3.45)$$

where

$$Q(s_z, N) = \frac{Z(s_z, N)}{N! \Lambda^{3N}} \quad (3.46)$$

and

$$Z(s_z, N) = \int_{V^N} d\mathbf{r}^N \exp[-\beta U(\mathbf{r}^N, N, s_z)] \quad (3.47)$$

is the configuration integral. The total potential energy $U(\mathbf{r}^N, N, s_z)$ of the system of interest can be expressed as

$$U(\mathbf{r}^N, N, s_z) = U_{\text{FF}} + U_{\text{FS}} \quad (3.48)$$

In (3.48), U_{FF} represents the fluid–fluid contribution of the potential energy given by

$$U_{\text{FF}} = \frac{1}{2} \sum_{i=1}^N \sum_{j=1 \neq i}^N u_{\text{ff}}(r_{ij}) \quad (3.49)$$

where

$$r_{ij} = |\mathbf{r}_{ij}| = \sqrt{(x_i - x_j)^2 + (y_i - y_j)^2 + (z_i - z_j)^2} \quad (3.50)$$

is the distance between molecules i and j . The fluid–substrate contribution can be expressed as [see (3.10)]

$$U_{\text{FS}} = U_{\text{FS}}^{[1]} + U_{\text{FS}}^{[2]} = \sum_{k=1}^2 \sum_{i=1}^N \Phi^{[k]}(x_i, z_i) \quad (3.51)$$

A macroscopic (thermodynamic) quantity O of the system of interest can now be identified with the ensemble average $\langle O \rangle$ of its microscopic analogue $O(\mathbf{r}^N, N, s_z)$. In the grand mixed isostress-isostrain ensemble $\langle O \rangle$ is given by [see (3.34),(3.35)]

$$\begin{aligned} O = \langle O \rangle &= \frac{1}{\chi} \sum_{s_z} \sum_N \exp(\beta T_{zz} A_z s_z) \exp(\beta \mu N) \\ &\times \frac{1}{N! \Lambda^{3N}} \int_{V^N} d\mathbf{r}^N O(\mathbf{r}^N, N, s_z) \exp[-\beta U(\mathbf{r}^N, N, s_z)] \\ &=: \sum_{s_z} \sum_N \int_{V^N} d\mathbf{r}^N O(\mathbf{r}^N, N, s_z) f_0(\mathbf{r}^N, N, s_z) \end{aligned} \quad (3.52)$$

where $f_0(\mathbf{r}^N, N, s_z)$ is the probability density of the grand mixed isostress-isostrain ensemble in the classical limit. Consider, for example, the simple case $O(\mathbf{r}^N, N, s_z) = N$. From (3.52) $\langle O \rangle = \langle N \rangle$ follows then immediately. For other quantities of interest, for example, the stress tensor components $O = T_{zx}$ and $O = T_{yy}$, the functional form of $O(\mathbf{r}^N, N, s_z)$ is more complicated as we shall demonstrate in the following section.

3.3.3 Molecular expressions for stress tensor components

In this section we derive microscopic expressions for the three stress tensor components T_{zx} , T_{yy} and T_{zz} and for the shear modulus c_{44} (associated with T_{zx}) which are key quantities here. From (3.24) it is evident that the shear stress T_{zx} is given by

$$T_{zx} = \frac{1}{A_z} \left(\frac{\partial \Psi}{\partial(\alpha s_x)} \right)_{T, \mu, s_x, s_y, T_{zz}}. \quad (3.53)$$

Using (3.42) we can rewrite (3.53) as

$$\begin{aligned} T_{zx} &= -\frac{1}{\beta A_z \chi} \frac{\partial \chi}{\partial(\alpha s_x)} \\ &= -\frac{1}{\beta A_z \chi} \sum_{s_z} \exp(\beta T_{zz} A_z s_z) \sum_N \exp(\beta \mu N) \frac{1}{N! \Lambda^{3N}} \frac{\partial Z(s_z, N)}{\partial(\alpha s_x)}. \end{aligned} \quad (3.54)$$

where we have also used (3.45)-(3.47). The partial derivative on the second line of (3.54) can be rewritten more explicitly as

$$\begin{aligned} \frac{\partial Z(s_z, N)}{\partial(\alpha s_x)} &= \frac{\partial}{\partial(\alpha s_x)} \prod_{i=1}^N \int_{-s_y/2}^{s_y/2} dy_i \int_{-s_z/2}^{s_z/2} dz_i \int_{-s_x/2+(\alpha s_x)(z_i/s_z+1/2)}^{s_x/2+(\alpha s_x)(z_i/s_z+1/2)} dx_i \\ &\times \exp\{-\beta[U_{FF}(\{\mathbf{r}\}^N) + U_{FS}(\{\mathbf{r}\}^N)]\} \end{aligned} \quad (3.55)$$

where we have assumed that the lamella is sheared homogeneously. To solve (3.55) it is convenient to interchange the order of integration and differentiation. Therefore both operations must be independent, which can be achieved by introducing dimensionless variables [85]

$$x \longrightarrow \tilde{x} = \frac{x}{s_x} - \alpha \left(\tilde{z} + \frac{1}{2} \right) \quad (3.56)$$

$$y \longrightarrow \tilde{y} = \frac{y}{s_y} \quad (3.57)$$

$$z \longrightarrow \tilde{z} = \frac{z}{s_z} \quad (3.58)$$

following Hill [83] and McQuarrie [82]. The distance between molecules i and j in dimensionless variables is therefore given by [85]

$$r_{ij} = \sqrt{s_x^2(\tilde{x}_i - \tilde{x}_j + \alpha(\tilde{z}_i - \tilde{z}_j))^2 + s_y^2(\tilde{y}_i - \tilde{y}_j)^2 + s_z^2(\tilde{z}_i - \tilde{z}_j)^2} . \quad (3.59)$$

Using (3.56) to (3.58), (3.55) may be recast as

$$\begin{aligned} \frac{\partial Z}{\partial(\alpha s_x)} &= -\beta(s_x s_y s_z)^N \prod_{i=1}^N \int_{-1/2}^{1/2} d\tilde{x}_i \int_{-1/2}^{1/2} d\tilde{y}_i \int_{-1/2}^{1/2} d\tilde{z}_i \\ &\times \exp\{-\beta[U(\{\mathbf{r}\}^N)]\} \frac{\partial}{\partial(\alpha s_x)} [U_{FF}(\{\mathbf{r}\}^N) + U_{FS}(\{\mathbf{r}\}^N)] . \end{aligned} \quad (3.60)$$

Replacing in (3.54), $\partial Z/\partial(\alpha s_x)$ by (3.60) and comparing the result with (3.52) we find that

$$T_{zx} = T_{zx}^{\text{FF}} + T_{zx}^{\text{FS}} \quad (3.61)$$

where

$$T_{zx}^{\text{FF}} := \frac{1}{A_z} \left\langle \frac{\partial}{\partial(\alpha s_x)} U_{FF}(\{\mathbf{r}\}^N) \right\rangle \quad (3.62)$$

and

$$T_{zx}^{\text{FS}} := \frac{1}{A_z} \left\langle \frac{\partial}{\partial(\alpha s_x)} U_{FS}(\{\mathbf{r}\}^N) \right\rangle . \quad (3.63)$$

Using (3.49)

$$\begin{aligned} T_{zx}^{\text{FF}} &= \frac{1}{A_z} \left\langle -\frac{1}{2s_z} \sum_{i=1}^N \sum_{j=1 \neq i}^N u'_{FF}(r_{ij}) \frac{x_{ij} z_{ij}}{r_{ij}} \right\rangle \\ &=: \frac{1}{A_z} \left\langle -\frac{1}{2s_z} W_{zx} \right\rangle \end{aligned} \quad (3.64)$$

where the last equality defines Clausius' virial W_{zx} [83]. Similarly, From (3.63) and (3.51) one has (see [85] for details)

$$T_{zx}^{\text{FS}} = -\frac{1}{A_z} \left\langle \frac{1}{s_z} \sum_{k=1}^2 \sum_{i=1}^N f_x^{[k]}(x_i, z_i) \left(z_i + \frac{s_z}{2} \right) \right\rangle \quad (3.65)$$

where $f_x^{[k]}(x_i, z_i)$ is the x -component of the force exerted by wall k on a fluid molecule i located at (x_i, z_i) . This force is given by [see (3.10) and appendix B]

$$f_x^{[k]}(x_i, z_i) = -\frac{\partial\Phi(x_i, z_i)}{\partial x} . \quad (3.66)$$

Thus, equations (3.64) and (3.65) provide the “virial” route to T_{zx} .

Alternatively, it is possible to differentiate $Z(s_z, N)$ in (3.54) directly [85], by applying Leibniz’s rule for the differentiation of an integral [81]. Since the integrations over x_i and z_i are independent of αs_x one may rewrite (3.55)

$$\frac{\partial Z}{\partial(\alpha s_x)} = \prod_{i=1}^N \int_{-s_y/2}^{s_y/2} dy_i \int_{-s_z/2}^{s_z/2} dz_i \frac{\partial}{\partial(\alpha s_x)} g \quad (3.67)$$

where

$$g := \int_{-s_x/2+(\alpha s_x)(z_i/s_z+1/2)}^{s_x/2+(\alpha s_x)(z_i/s_z+1/2)} dx_1 g_1 \quad (3.68)$$

and

$$g_1 := \prod_{i=2}^N \int_{-s_x/2+(\alpha s_x)(z_i/s_z+1/2)}^{s_x/2+(\alpha s_x)(z_i/s_z+1/2)} dx_i \exp[-\beta U(\{\mathbf{r}\}^N)] . \quad (3.69)$$

With aid of Leibniz’s rule one obtains

$$\begin{aligned} \frac{\partial}{\partial(\alpha s_x)} g &= \int_{-s_x/2+(\alpha s_x)(z_i/s_z+1/2)}^{s_x/2+(\alpha s_x)(z_i/s_z+1/2)} dx_1 \frac{\partial}{\partial(\alpha s_x)} g_1 \quad (3.70) \\ &+ g_1 \left[x_1 = +\frac{s_x}{2} + \alpha s_x \left(\frac{z_i}{s_z} + \frac{1}{2} \right) \right] \left(\frac{z_i}{s_z} + \frac{1}{2} \right) \\ &- g_1 \left[x_1 = -\frac{s_x}{2} + \alpha s_x \left(\frac{z_i}{s_z} + \frac{1}{2} \right) \right] \left(\frac{z_i}{s_z} + \frac{1}{2} \right) . \end{aligned}$$

Because the system is periodic in the x -direction of period s_x it follows from (3.69) that the last two terms in the integrand of (3.70) are identical and thus cancel. Applying Leibniz’s rule N times we eventually obtain

$$\begin{aligned} \frac{\partial Z}{\partial(\alpha s_x)} &= \prod_{i=1}^N \int_{-s_y/2}^{s_y/2} dy_i \int_{-s_z/2}^{s_z/2} dz_i \int_{-\frac{s_x}{2} + \alpha s_x \left(\frac{z_i}{s_z} + \frac{1}{2} \right)}^{\frac{s_x}{2} + \alpha s_x \left(\frac{z_i}{s_z} + \frac{1}{2} \right)} dx_i \quad (3.71) \\ &\times \frac{\partial}{\partial(\alpha s_x)} \exp[-\beta U(\mathbf{r}^N)] . \end{aligned}$$

Since the fluid–fluid interaction is independent of αs_x , $\partial U_{FF}/\partial(\alpha s_x) \equiv 0$ [see (3.1), (3.50)]. From (3.3) it is furthermore clear that the interaction of fluid

molecules with the lower wall [k=1 in (3.51)] is also independent of αs_x , that is $\partial U_{FS}^{[1]}/\partial(\alpha s_x) \equiv 0$. Thus we arrive at

$$T_{zx} = -\frac{1}{A_z} \left\langle \sum_{i=1}^N f_x^{[2]} \right\rangle =: -\frac{1}{A_z} \langle F_x^{[2]} \rangle . \quad (3.72)$$

The last line of (3.72) gives T_{zx} as the x -component of the total force exerted *by* the fluid lamella *on* the walls. Consequently, we refer to it as the “force” expression. “Force” [see (3.72)] and “virial” [see (3.61), (3.64),(3.65)] routes to T_{zx} are useful since they provide a check on internal consistency of the simulation results to be presented below.

By analogy with the derivation of the shear stress molecular expressions for T_{yy} can also be derived. Since the fluid–substrate potential $\Phi^{[k]}(x, z)$ (3.10) is translationally invariant in y -direction the partial derivative of $\Phi^{[k]}(x, z)$ with respect to y vanishes. Thus, T_{yy} is given by

$$T_{yy} = -\frac{1}{\beta A_z} \left\langle \frac{N}{s_z} \right\rangle + \frac{1}{A_z} \left\langle \frac{1}{2s_z} \sum_{i=1}^N \sum_{j=1 \neq i}^N u'_{FF}(r_{ij}) \frac{y_{ij}^2}{r_{ij}} \right\rangle . \quad (3.73)$$

A force expression for T_{yy} similar to (3.72) does not exist since the system does not contain a solid substrate in the y -direction. Consequently, arguments similar to the one between (3.69) and (3.70) do not exist. Similarly, one may derive a molecular expression for T_{yy} in the grand canonical ensemble, that is

$$T_{yy} = -\frac{1}{\beta V} \langle N \rangle + \frac{1}{V} \left\langle \frac{1}{2} \sum_{i=1}^N \sum_{j=1 \neq i}^N u'_{FF}(r_{ij}) \frac{y_{ij}^2}{r_{ij}} \right\rangle . \quad (3.74)$$

In the grand canonical ensemble the wall distance s_z is a natural variable of Ω [see (3.21)]. Therefore, a virial expression for T_{zz} can be derived

$$\begin{aligned} T_{zz} &= -\frac{\langle N \rangle}{\beta V} + \frac{1}{V} \left\langle \frac{1}{2} \sum_{i=1}^N \sum_{j=1 \neq i}^N u'_{FF}(r_{ij}) \frac{z_{ij}^2}{r_{ij}} \right\rangle \\ &\quad - \frac{1}{V} \left\langle \sum_{k=1}^2 \sum_{i=1}^N f_z^{[k]}(x_i, z_i) (z_i + (-1)^k \frac{s_z}{2}) \right\rangle . \end{aligned} \quad (3.75)$$

By arguments parallel to the ones above a force expression [see (3.69), (3.70)] (see Ref. [79])

$$T_{zz} = -\frac{1}{2A_z} \left[\langle F_z^{[1]} \rangle - \langle F_z^{[2]} \rangle \right] \quad (3.76)$$

also exists.

Another quantity of interest in the context of this work is the shear modulus

$$c_{44} := \left(\frac{\partial^2 \Psi}{\partial (\alpha s_x)^2} \right)_{T, \mu, s_x, s_y, T_{zz}} = \left(\frac{\partial T_{zx}}{\partial (\alpha s_x)} \right)_{T, \mu, s_x, s_y, T_{zz}} \quad (3.77)$$

in Voigt's notation [80]. By a tedious but straightforward calculation parallel to the one detailed in [86] one can show from (3.45), (3.54) and (3.77) that

$$Ac_{44} = -\beta \left[\langle F_x^{[2]2} \rangle - \langle F_x^{[2]} \rangle^2 \right] + \left\langle \frac{\partial^2 U_{\text{FS}}^{[2]}}{\partial (\alpha s_x)^2} \right\rangle . \quad (3.78)$$

From (3.72), and (3.78) it is clear that

$$\frac{\partial^2 U_{\text{FS}}^{[2]}}{\partial (\alpha s_x)^2} = -\frac{\partial F_x^{[2]}}{\partial (\alpha s_x)} = -\sum_{i=1}^N \frac{\partial f_x^{[2]}(\tilde{x}_i, z_i)}{\partial (\alpha s_x)} . \quad (3.79)$$

The next section introduces Monte Carlo simulations as a method to calculate the required ensemble averages.

3.4 Monte Carlo simulation

As we have seen in the preceding sections, thermodynamic properties of the confined fluid lamella can be calculated from molecular expressions as ensemble averages. This program requires knowledge of the probability density f_0 defined in (3.52). However, f_0 is accessible only if the configuration integral (Z) is known *a priori*. To calculate it one could *in principle* introduce additional simplifying assumptions or resort to numerical techniques instead. Unfortunately, a deeper analysis reveals that even numerical approaches have great difficulty to obtain an estimate of Z (see, for example, Chap.2 of [87]). To circumvent these problems one therefore seeks a numerical method capable of computing ensemble averages *without* requiring knowledge of the configuration integral. This is accomplished by the Monte Carlo (MC) method.

3.4.1 The general method

To calculate ensemble averages in Monte Carlo simulations we need to discretize the space of microstates $\mathbf{\Gamma} = \{\mathbf{r}^N, s_z, N\}$ and replace (3.52) by

$$\langle O \rangle = \lim_{M \rightarrow \infty} \frac{\sum_{k=1}^M O(\mathbf{\Gamma}_k) f_0(\mathbf{\Gamma}_k)}{\sum_{k=1}^M f_0(\mathbf{\Gamma}_k)} \quad (3.80)$$

Within the concept of *importance sampling* [88], where microstates $\{\Gamma_k\}$ are generated according to f_0 (i.e., their “importance”), (3.80) can be simplified further to

$$\langle O \rangle = \lim_{M \rightarrow \infty} \frac{1}{M} \sum'_{m=1}^M O(\Gamma_m) \quad (3.81)$$

where the prime attached to the summation sign to emphasizes generation of microstates with a probability proportional to f_0 . Importance sampling can be realized conveniently if microstate generation proceeds as a (stationary) Markov process [89] Since the implementation of Markov processes in the context of Monte Carlo simulations is well explained in the literature [79, 87, 90], we summarize only briefly the main concepts.

Let $\mathbf{p}(n)$ be the vector of probabilities of all microstates at time $t + 1$. Then the immediately preceding vector $\mathbf{p}(m)$ is related to $\mathbf{p}(n)$ by

$$\mathbf{p}(n) = \mathbf{P}\mathbf{p}(m) \quad (3.82)$$

where \mathbf{P} is the transition matrix. Matrix elements P_{nm} (transition probabilities) represent the probability of a transition from state “m” to state “n”. If we take \mathbf{P} to be time-independent and apply it repeatedly [i.e., $\mathbf{P} \cdots \mathbf{P}\mathbf{p}(m)$] the resulting probability vector will eventually become stationary, that is, it satisfies the equation

$$\boldsymbol{\pi} = \mathbf{P}\boldsymbol{\pi} \quad (3.83)$$

where $\boldsymbol{\pi}$ is the limiting (stationary) probability eigenvector of \mathbf{P} . It can be shown that a sequence of microstates (i.e., a Markov chain) will indeed become stationary and that $\boldsymbol{\pi}$ is unique if \mathbf{P} is constructed such that in principle any state n can be reached in a finite number of steps (i.e., repeated application of \mathbf{P}) from any other state [90]. In practice, we therefore need to construct \mathbf{P} such that $\boldsymbol{\pi}$ is proportional to the probability density of the ensemble in question. This task becomes much simpler if we invoke the principle of microscopic reversibility

$$P_{nm}\pi_m = P_{mn}\pi_n \quad (3.84)$$

which automatically satisfies (3.83). However, it is extremely difficult (if not impossible) to realize transitions between microstates with the correct probability. Instead we perform “trial” transitions between microstates governed by a certain probability α (the “underlying matrix” [91] of the Markov chain) and

then decide whether the trial state is taken as a new state “n” or not; if not, the system remains in its original state “m”. Hence, (3.84) is now given by

$$\alpha_{nm}P_{nm}\pi_m = \alpha_{mn}P_{mn}\pi_n . \quad (3.85)$$

Assuming a symmetric underlying matrix (i.e., $\alpha_{mn} = \alpha_{nm}$), we can rearrange (3.85) to give

$$\frac{P_{nm}}{P_{mn}} = \frac{\pi_n}{\pi_m} . \quad (3.86)$$

In essence, $\alpha_{mn} = \alpha_{nm}$ expresses the assumption that trial state “n” is generated from “m” with the same probability with which trial state “m” would be generated from “n” as the initial state. Equation (3.86) is a formulation of the *principle of detailed balance*. Equation (3.86) can be implemented following Metropolis et al. [92] by choosing

$$P_{nm} = \min\left(1, \frac{\pi_n}{\pi_m}\right) . \quad (3.87)$$

The advantage of (3.87) is that P_{nm} depends only on the ratio π_n/π_m , so that the unknown (and in most cases inaccessible) partition function cancels out, as we shall demonstrate in the following section.

3.4.2 Application and Implementation

According to (3.87) a trial state “n” is immediately accepted if $\pi_n \geq \pi_m$. If on the other hand, $\pi_n < \pi_m$, (3.87) can be written more explicitly as

$$P_{nm} = \frac{\pi_n}{\pi_m} = \frac{f_0(\mathbf{\Gamma}_n)}{f_0(\mathbf{\Gamma}_m)} \quad (3.88)$$

where it is clear from (3.52) that the configuration integral cancels between denominator and numerator so that on the basis of a Markov process the importance–sampling concept [see (3.81)] can indeed be implemented.

Because of the functional form of f_0 in (3.52) it seems sensible to generate a numerical representation of a Markov chain through a sequence of three consecutive and independent processes. In the first of these N and s_z remain constant and a (randomly or sequentially) selected fluid molecule i is displaced at random according to

$$\mathbf{r}_i^{(n)} = \mathbf{r}_i^{(m)} + \delta_r(\mathbf{1} - 2\boldsymbol{\xi}) \quad (3.89)$$

where $\mathbf{1} := (1, 1, 1)$ and $\boldsymbol{\xi}$ is a vector whose three components are (pseudo-) random numbers distributed uniformly on the interval $[0, 1]$. In (3.89), δ_r is the side length of a small cube centered on $\mathbf{r}_i^{(m)}$. Since N and s_z remain constant between initial (m) and new trial configurations (n) it is easy to verify from (3.52) and (3.88) that

$$P_{\text{nm}}^{\text{I}} = \min[1, \exp(-\beta\Delta U_{\text{nm}})] \quad (3.90)$$

where

$$\Delta U_{\text{nm}} = \sum_{j \neq i}^N \left[u_{\text{ff}}(r_{ij}^{(n)}) - u_{\text{ff}}(r_{ij}^{(m)}) \right] + \sum_{k=1}^2 \left[\Phi^{[k]}(x_i^{(n)}, z_i^{(n)}) - \Phi^{[k]}(x_i^{(m)}, z_i^{(m)}) \right] \quad (3.91)$$

is the change in configurational energy associated with the displacement of molecule i . The acceptance ratio for displacement steps generally depends on δ_r . Following standard practice [72] we adjust δ_r during a Monte Carlo simulation to maintain an overall acceptance of roughly 50% of all attempted displacements. Based upon this criterion, δ_r depends on the actual thermodynamic state, that is on T and the average density of the fluid.

In the next process a molecule is either created at a randomly selected position \mathbf{r}_i or a randomly selected, already existing molecule is removed from its present position \mathbf{r}_i . Both processes are attempted with equal probability. Since s_z remains fixed and the spatial positions of all other molecules are unaltered it is a straightforward matter to demonstrate from (3.52) and (3.88) that

$$P_{\text{nm}}^{\text{II}} = \min(1, \exp(r_{\pm})) \quad (3.92)$$

where

$$r_{\pm} = \pm B \mp \ln N \mp \beta U_{\pm} \quad (3.93)$$

$$B = \beta\mu - \ln \left(\frac{\Lambda^3}{V} \right) \quad (3.94)$$

$$U_{\pm} = \sum_{j \neq i}^N u_{\text{ff}}(r_{ij}) + \sum_{k=1}^2 \Phi^{[k]}(x_i, z_i) \quad (3.95)$$

and N is the number of fluid molecules *after* addition (r_+) or *prior to* removal (r_-) of molecule i . Notice that in contrast to the displacement step, where the acceptance ratio can be adjusted through variations of δ_r , no such adjustment

is possible here. The acceptance ratio is solely determined by the physical situation, that is by temperature and density of the fluid.

The third and final process involves compression/expansion of the confined fluid effected by random displacements of the substrates according to

$$s_z^{(n)} = s_z^{(m)} + \delta_s(1 - 2\xi) \quad (3.96)$$

where ξ is a random number uniformly distributed on $[0, 1]$ and δ_s is a small displacement increment again adjusted during the course of the simulation such that roughly 50% of all compression/expansion attempts are accepted. Because of (3.96)

$$z_i^{(n)} = z_i^{(m)} \frac{s_z^{(n)}}{s_z^{(m)}} \quad \forall i = 1, \dots, N \quad (3.97)$$

Since during compression/expansion attempts N remains fixed this process is realized with probability

$$P_{\text{nm}}^{\text{III}} = \min [1, \exp(r_s)] \quad (3.98)$$

where

$$r_s = \beta \left[T_{zz} A_z \left(s_z^{(n)} - s_z^{(m)} \right) - \Delta U_{\text{nm}} \right] + N \ln \left(\frac{s_z^{(n)}}{s_z^{(m)}} \right) \quad (3.99)$$

as one can verify from (3.52) and (3.98). In (3.99)

$$\begin{aligned} \Delta U_{\text{nm}} = & \frac{1}{2} \sum_{i=1}^N \sum_{j \neq i}^N \left[u_{\text{ff}}(r_{ij}^{(n)}) - u_{\text{ff}}(r_{ij}^{(m)}) \right] \\ & + \sum_{k=1}^2 \sum_{i=1}^N \left[\Phi^{[k]}(x_i^{(n)}, z_i^{(n)}) - \Phi^{[k]}(x_i^{(m)}, z_i^{(m)}) \right] \end{aligned} \quad (3.100)$$

The last term in (3.99) (as well as the factor V in (3.94)) arise for reasons detailed in [87].

The three processes are carried out sequentially. Suppose the system contains N_{init} molecules at the beginning of a sequence. Then N_{init} displacements, N_{init} creation/destruction events and one compression/expansion attempt constitute a Monte Carlo cycle in the grand mixed isostress-isostrain ensemble. This ratio is convenient because the last step displaces all N_{init} molecules at once on account of (3.97). Thus, (3.100) involves in principle numerical operations of order N^2 whereas a *single* displacement or creation/destruction attempt requires numerical operation of order N . Monte Carlo results to be presented in

chapter 4 are typically based on 37500 cycles with systems containing roughly 200 to 3000 fluid molecules (depending on the thermodynamic state).

Chapter 4

Phase behavior and thermomechanical properties

In the two preceding chapters mean-field theory and Monte Carlo simulations were introduced, which are now applied to investigate the phase behavior and thermomechanical properties of confined fluids. We already demonstrated (see section 2.4) that fluids confined by chemically corrugated walls can be expected to exhibit a complex phase behavior. In order to unravel the dependence of the phase diagram on the various model parameters $\{n_z, n_s, n_w, \epsilon_{fs}, \epsilon_{fw}, \alpha s_x\}$, we will now employ the mean-field lattice model discussed in chapter 2 to study the influence of variations of individual model parameters in depth. Since the mean-field treatment is based on a number of simplifying assumptions, it seems sensible to verify its predictions independently within the framework of the more realistic continuous model of a fluid confined between nanopatterned substrates which we introduced in chapter 3. As pointed out in section 3.4, this latter model can be treated only by means of (Monte Carlo) computer simulations which are computationally much more demanding than solving the mean-field model. Therefore, we restrict Monte Carlo simulations to a verification of key predictions of the mean-field treatment.

In parallel experiments confined fluids are explored from various points of view. For example, gas adsorption in porous materials [55] demonstrated that the phase behavior is strongly affected by the pore width (wall distance s_z). These experiments provide clear evidence for the impact of confinement on the phase diagram of a fluid adsorbed in a porous medium which differs from that of a corresponding bulk fluid the more the narrower the pores are. Adsorption experiments on chemically nanopatterned substrates showed selective adsorption on substrate regions composed of the chemical compound preferred energetically by the adsorbent [22]. Properties of the adsorbed fluid such as, for instance its evaporation rate [22] depend significantly on the pattern size, i.e. the chemical corrugation (c_r). Influence of pore size and chemical corrugation on the phase behavior of confined fluids will be delineated in this chapter.

With the help of the surface forces apparatus (SFA) [69] mechanical properties of thin fluid films can be measured directly on the nanoscale. In an SFA experiment the fluid is confined between two solid substrates and maintained under constant pressure or load applied in the direction normal to the fluid-substrate interface. Under these conditions a confined fluid of a typical thickness of one to ten molecular diameters can be exposed to a shear strain. The impact of shear strain on both phase behavior and thermomechanical properties like the conjugate shear stress and modulus will be discussed below.

4.1 Phase behavior

4.1.1 Variation of wall distance

The thermodynamic state of a fluid confined between chemically heterogeneous walls depends on various system parameters $\{n_z, n_s, n_w, \epsilon_{fs}, \epsilon_{fw}, \alpha_{sx}\}$. In this multidimensional parameter space the degree of confinement, that is n_z , is particularly important as far as the phase behavior of the confined fluid is concerned. This has been demonstrated by Thommes and Findenegg [55] who determined the coexistence curve of pure SF₆ in controlled-pore glasses (CPG) of nominal pore widths of 31 and 24 nm, respectively. Their results show that the pore critical point shifts to temperatures *below* the bulk critical temperature T_c and to densities *above* the bulk critical density (see figure 7 in [55]).

Consequently, the entire phase diagram of the pore fluid is displaced to higher densities and lower temperatures. This shift was found to be stronger for the narrower pores. Thus, it seems sensible to begin a discussion of confinement effects by investigating the impact of n_z on the phase diagram $\mu_x(T)$ within the framework of the lattice-gas model of a fluid confined by chemically decorated substrate surfaces (see figure 2.1) which we introduced already in section 2.1. The lattice-gas model is particularly convenient for this purpose, because it is numerically not too demanding. To compute phase diagrams for $T > 0$ we utilize the method detailed in section 2.2.3.

Figure 4.1(a) shows plots of phase diagrams in μ - T projection for various degrees of confinement (i.e., n_z). The horizontal line represents the bulk phase diagram which we include for comparison. It consists of a single coexistence curve $\mu_x^{\text{gl}}(T) = \mu_c = -3$ [see (2.92) and figure 2.8]. Along $\mu_x^{\text{gl}}(T)$ gas and liquid (bulk) phases coexist. Thus, $\mu_x^{\text{gl}}(T)$ is a line of first-order phase transitions terminating, of course, at $T = T_c = 3/2$ (2.96). We employ dimensionless units introduced already in section 2.1.1.

More subtle effects are observed if the lattice gas is confined by solid substrates as plots in figure 4.1(a) show. For sufficiently large n_z [see, for example, $n_z = 15$ in figure 4.1(a)] the coexistence line shifts to lower chemical potentials compared with the bulk and is no longer parallel to the temperature axis. Furthermore, the critical point moved to lower T and μ in qualitative agreement with experimental findings [55]. The difference between the bulk gas-liquid coexistence line and that shown for $n_z = 15$ is not solely due to a confinement effect, as we will see shortly.

Figure 4.2 clearly shows that the full phase diagram for the confined fluid consists of more than one coexistence line. This has been overlooked in the past [64, 65, 79, 93, 94, 95, 96]. Detailed investigations reveal that the upper coexistence line (i.e., the one at higher chemical potentials) $\mu_x^{\text{dl}}(T)$ in figure 4.2 refers to first-order phase transitions between droplet and liquid phases (see section 2.4.2). The lower one, on the other hand, is identified as the gas-droplet coexistence line $\mu_x^{\text{gd}}(T)$. The local density $\rho(x_i, z_i) = \rho_i$ (see section 2.3.1) of a typical droplet phase is shown in figure 4.3(a). The droplet phase consists of fluid-filled columns (in the y -direction) adsorbed along the strongly attractive

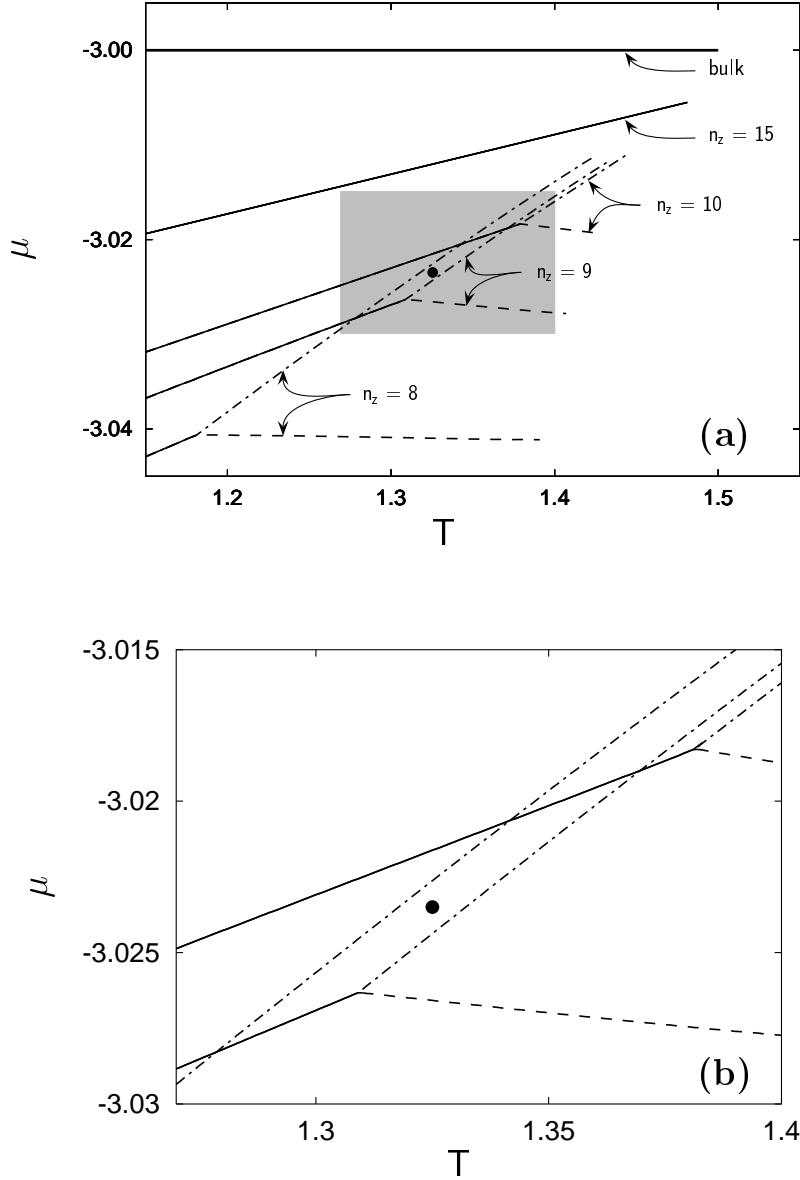


Figure 4.1: (a) Part of phase diagrams in T - μ projection for various confined lattice gases as a function of substrate separation n_z indicated in figure ($\alpha = 0$, $n_x = 14$, $n_s = 8$, $\epsilon_{fs} = 1.4$, $\epsilon_{fw} = 0.3$); (—) $\mu_x^{dl}(T)$, (---) $\mu_x^{db}(T)$, (- · -) $\mu_x^{bl}(T)$. Corresponding bulk coexistence curve is also shown. (b) as (a) but on an enhanced scale showing only coexistence-curve branches in grey box of (a); (●): denotes fixed thermodynamic state of confined $T = 1.325$, $\mu = -3.0235$ see text.

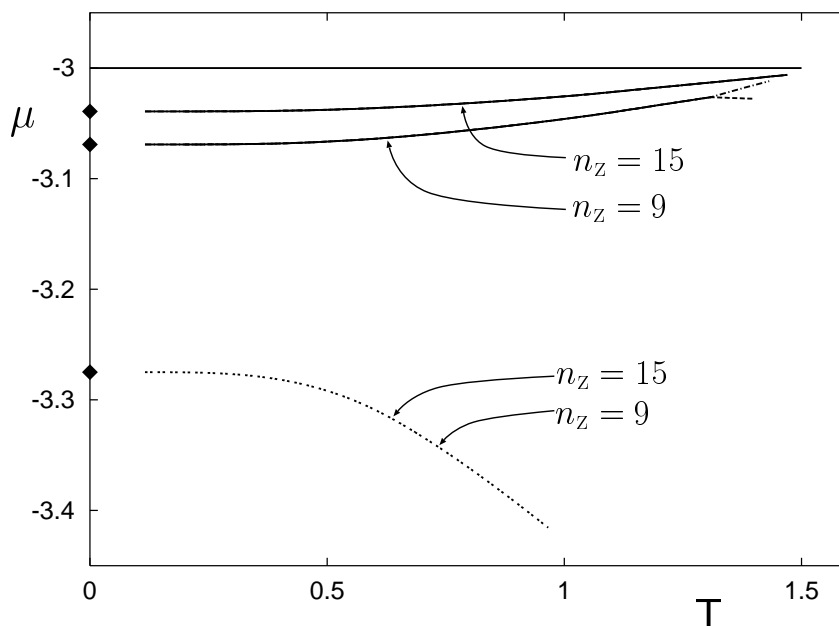


Figure 4.2: As figure 4.1 but here the full phase diagrams for two substrate separations $n_z = 15$ and $n_z = 9$ are shown. Notice, the gas–droplet coexistence line $\mu_x^{\text{gd}}(T)$ (\dots) is independent of n_z (within computational accuracy). Analytic solutions (2.53) for $T = 0$ are indicated by (\blacklozenge).

substrate parts. During a first–order phase transition from the gas (where the system is almost empty) to the droplet phase [that is upon crossing $\mu_x^{\text{gd}}(T)$] the columns fill. Filling is obviously induced by the presence of a single surface and controlled by the strongly attractive substrate parts. Thus, $\mu_x^{\text{gd}}(T)$ is expected to be independent of the wall separation n_z . This notion is supported by plots in figure 4.2 where $\mu_x^{\text{gd}}(T)$ is the same for $n_z = 9$ and 15. This holds all the way down to $T = 0$ where the analytic solution [see (2.53)] is given by

$$\mu_x^{\text{gd}}(T = 0) = -2 - \epsilon_{\text{fs}} - \frac{1}{n_s} \quad (4.1)$$

which is independent of n_z as expected. On the contrary [see (2.58)]

$$\mu_x^{\text{dl}}(T = 0) = -3 + \frac{(n_w - n_s) + 2(1 - n_w \epsilon_{\text{fs}})}{n_w n_z + n_s(n_z - 2)} \quad (4.2)$$

does depend on n_z explicitly. Hence, one expects this dependence to persist even at nonzero temperatures. Plots of $\mu_x^{\text{dl}}(T)$ in figure 4.2 confirm this notion.

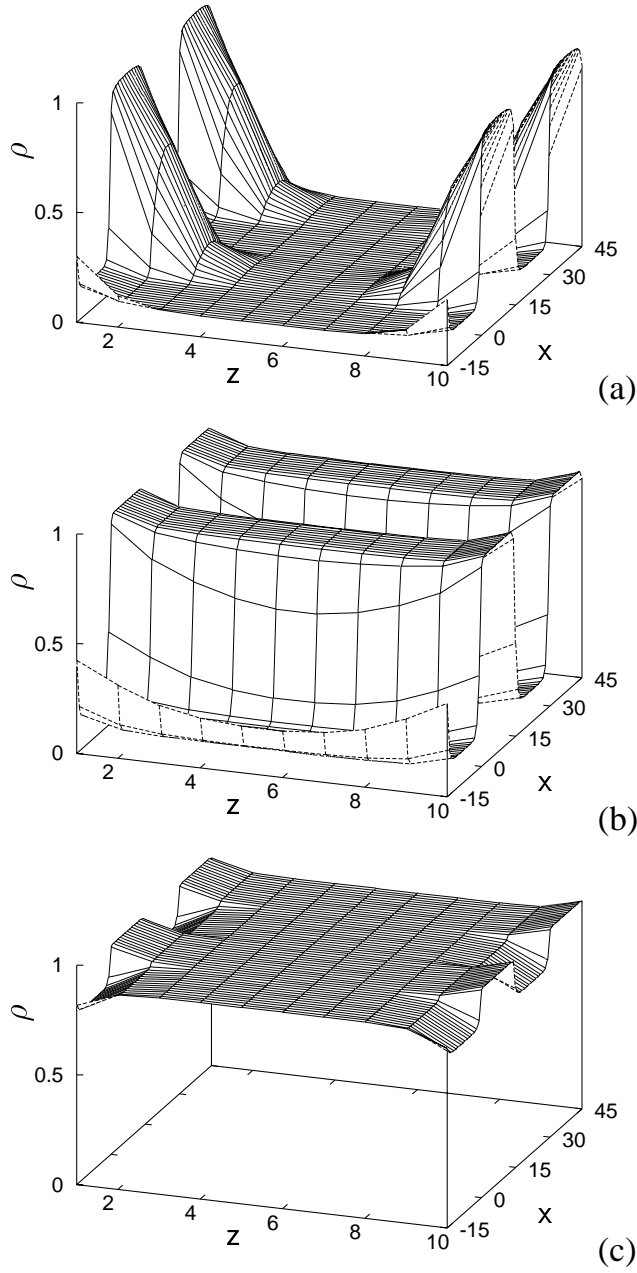


Figure 4.3: Typical microscopic structures of the lattice gas confined between chemically striped substrates (see figure 2.1). Plots show local density $\rho(x_i, z_i)$ as a function of position in the x - z -plane. The thermodynamic state is specified by $T = 1.1$, and (a) droplet phase ($\mu = -3.06$), (b) bridge phase ($\mu = -3.03$), (c) liquid phase ($\mu = -3.01$) (see text). Substrate parameters are $n_s = 15$, $n_w = 15$, $n_z = 8.0$ with $\epsilon_{fs} = 1.6$ and $\epsilon_{fw} = 0.4$.

Moreover, if n_z decreases, a bifurcation appears at $T = T_{\text{tr}}^{\text{dbl}}$. An inspection of the local densities reveals that only (inhomogeneous) liquid [figure 4.3(c)] and droplet phases [figure 4.3(a)] coexist along the line $\mu_x^{\text{dl}} (T < T_{\text{tr}}^{\text{dbl}})$. At $T = T_{\text{tr}}^{\text{dbl}}$ the latter two are in thermodynamic equilibrium with a bridge phase [see figure 4.3(b)]. As can be seen from the plot of local density in figure 4.3(b) the bridge phase consists of a high-density regime spanning the gap between the strongly attractive wall parts surrounded by a low density fluid controlled by the weakly attractive portions of the substrates. As the plot in figure 4.3(b) illustrates, bridge morphologies are inhomogeneous in one lateral direction (x) as reflected by their alternating high- and low-density regimes. Intuitively one would expect the stability of the bridges to depend strongly on the relative position of the substrates and particularly on n_z (we defer a detailed discussion of the impact of misaligning the walls in the x -direction to section 4.1.3 where the effect of exposing fluid bridges to shear deformations is analyzed in depth).

For $T > T_{\text{tr}}^{\text{dbl}}$, the phase diagram $\mu_x(T)$ consists of two branches. The upper one, $\mu_x^{\text{bl}}(T)$, is a line of first-order phase transitions involving liquid and bridge phases whereas the lower one, $\mu_x^{\text{db}}(T)$, corresponds to bridge and droplet phases, respectively. Both branches terminate at their respective critical points $\{\mu_c^{\text{bl}}, T_c^{\text{bl}}\}$ and $\{\mu_c^{\text{db}}, T_c^{\text{db}}\}$. According to (2.92) the phase diagram $\mu_x(T)$ of the lattice gas in the given temperature region is formed by $\mu_x^{\text{gd}}(T)$, $\mu_x^{\text{dl}}(T)$, $\mu_x^{\text{db}}(T)$, $\mu_x^{\text{bl}}(T)$, and the point $\{\mu_{\text{tr}}^{\text{dbl}}, T_{\text{tr}}^{\text{dbl}}\}$.

Comparing in figure 4.1(a) coexistence curves for $n_z = 8$ and 9, we see that the triple point is lowered the more the more severe the confinement is, that is the smaller n_z is. Simultaneously, μ_c^{bl} increases whereas μ_c^{db} decreases such that the one-phase region of the bridges widens. Because of these rather complex variations of $\mu_x(T)$ with n_z the following sequence of discontinuous phase transitions may be envisioned. Suppose $\{\mu, T\}$ is chosen such that the confined fluid in the limit $n_z \rightarrow \infty$ is a ‘‘droplet’’. This is illustrated in figure 4.1(b) where for a specific thermodynamic state determined by $T = 1.325$ and $\mu = -3.0235$ and $n_z = 10$ this state point falls *below* all branches of $\mu_x(T)$. However, as the substrate separation decreases, one notices from the plot corresponding to $n_z = 9$ that the same thermodynamic state now pertains to the one-phase regime of liquid phases, that is it falls *above* all branches of $\mu_x(T)$. Thus, in

going from $n_z = 10$ to $n_z = 9$ the confined lattice gas undergoes a first-order phase transition from a droplet to a liquid phase. For an even smaller substrate separation $n_z = 8$ one sees from figure 4.1(a) that the triple point has shifted to rather small values $\{\mu_{\text{tr}}^{\text{dbl}}, T_{\text{tr}}^{\text{dbl}}\}$ and that the one-phase region of bridge phases has widened considerably. Thus, as can be seen from the parallel plot in figure 4.1(b), the thermodynamic state eventually belongs to the one-phase region of bridge phases where it remains for all smaller n_z . Hence, as one decreases the substrate separation from $n_z = 9$ to $n_z = 8$ an originally liquid phase is transformed into a bridge phase during a first-order phase transition.

To confirm this successive appearance of phase transitions with decreased substrate separation, parallel results for the continuous model were obtained in a sequence of Monte Carlo simulations (see section 3.4) in the grand canonical ensemble where $T = 1.0$, $\mu = -11.50$, $s_x = 12.0$, $d_s = 4.0$, $d_w = 8.0$ with $\epsilon_{\text{fs}} = 1.25$ and $\epsilon_{\text{fw}} = 0.001$ [94] (we deviate from the lattice-gas notation $n_s \rightarrow d_s, n_w \rightarrow d_w, n_x \rightarrow s_x$ to emphasize that these dimensions can be varied continuously). Under these conditions the thermodynamically stable phase of a corresponding bulk system is a gas phase of mean density $\bar{\rho} = \langle N \rangle / V \simeq 0.036$ [97]. As before for the lattice gas we express all quantities in the customary dimensionless (i.e., “reduced”) units. However, here we again deviate from the lattice-gas by expressing length in units of σ [see (3.1)].

Depending on the degree of confinement (s_z) a fluid in the continuous model may form a droplet, liquid or bridge phase similar to the confined lattice gas (see figure 4.3). Typical structures of these three phases are illustrated by plots of the local density in figure 4.4. Within the framework of the continuous model the local density is defined as

$$\rho(x, z) := \frac{\langle N(x, z) \rangle}{\Delta x \Delta z s_y}. \quad (4.3)$$

In (4.3), $N(x, z)$ is the number of fluid molecules in a given configuration that are located in a square prism of dimensions $\Delta x \times s_y \times \Delta z$ centered on a point (x, z) . As in figure 4.3(a), $\rho(x, z)$ in figure 4.4(a) is representative of a typical bridge morphology. In the absence of a shear strain ($\alpha = 0$, see figure 3.1), $\rho(x, z)$ is symmetric with respect to $x = 0$ and $z = 0$ as it must be. As in the lattice-gas model, a bridge phase may condense or evaporate upon varying thermodynamic conditions. The microscopic structure of liquid and droplet

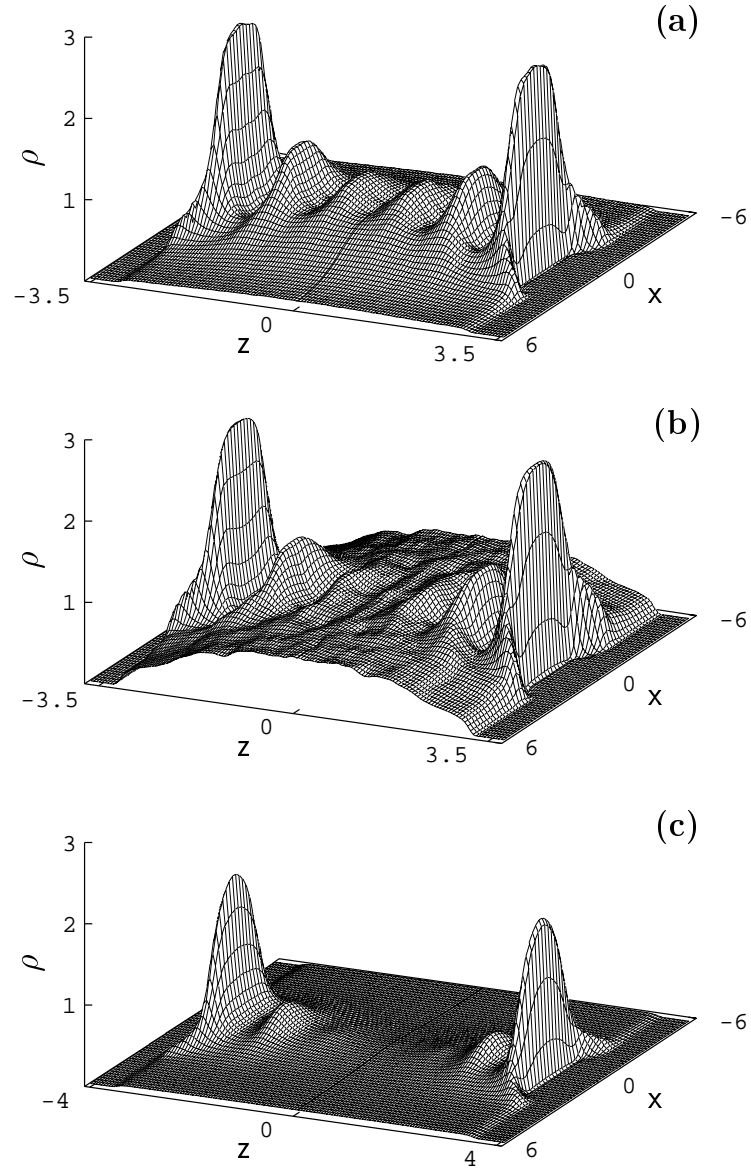


Figure 4.4: Typical microscopic structures of fluids confined between chemically striped substrates (see figure 3.1). Plots show local density $\rho(x, z)$ as a function of position in the x - z -plane. (a) bridge phase ($s_z = 7.2$), (b) liquid phase ($s_z = 7.5$), (c) droplet phase ($s_z = 8.2$) (see text). The thermodynamic state is specified by $T = 1.0$ and $\mu = -11.50$; substrate parameters are $s_x = 12.0$, $d_s = 4.0$, $d_w = 8.0$ with $\epsilon_{fs} = 1.25$ and $\epsilon_{fw} = 0.001$.

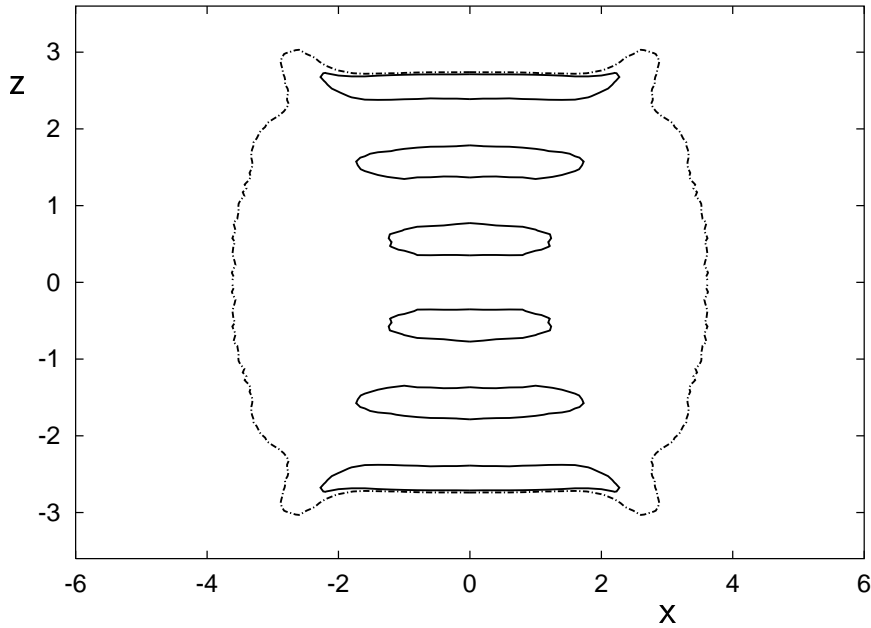


Figure 4.5: Contour lines $\rho(x, z) = 0.25$ (---), 0.70 (—) corresponding to the plot in figure 4.4(a).

phases for $\alpha = 0$ is illustrated by the plots in figure 4.4(b) and figure 4.4(c).

From the plot in figure 4.4(a) one notices that $\rho(x, z)$ is a nonmonotonic function of z along any line $x = \text{const}$ in the high-density regime. Nonmonotonicity of the local density is also clearly visible in plots of contour lines of $\rho(x, z)$ (i.e., lines along which $\rho(x, z) = \text{const}$). The plot in figure 4.5 shows a sequence of “islands” along the z -axis surrounded by a closed line of lower density. Apparently, the islands are resolved and well separated by a distance of approximately $\Delta z \simeq 1$ between centers of neighboring islands. Thus, it seems plausible to associate these islands with molecular strata parallel with the confining substrates. Stratification reflects substrate-mediated intermolecular correlations. With increasing distance from a substrate, stratification diminishes in the continuous model [see figure 4.4(a)] due to the decay of the fluid-substrate potential. This is reflected by a declining amplitude of oscillations in $\rho(x, z)$ with increasing distance from a substrate which can also be seen in figure 4.5 where the islands shrink in transverse (i.e., x -) direction as $|z| \rightarrow 0$. Within the lattice-gas model, stratification cannot be resolved in the local-density plots

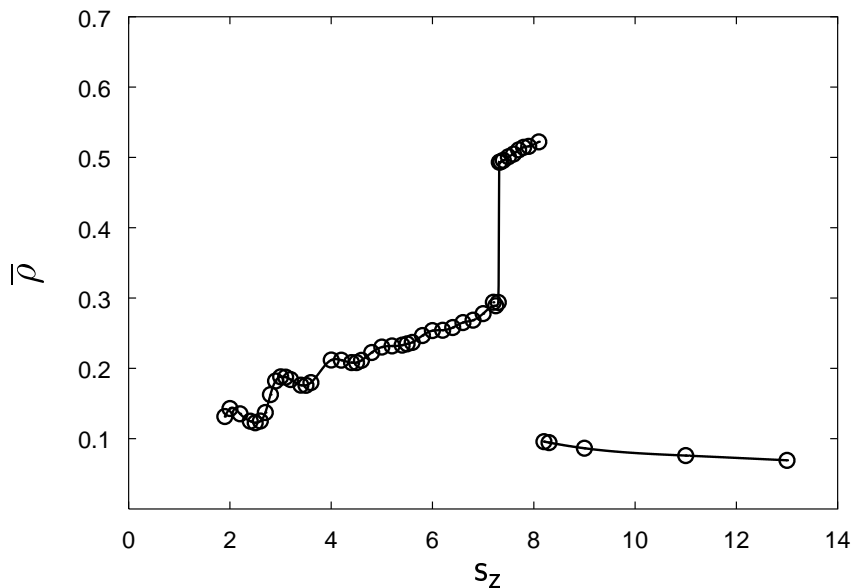


Figure 4.6: Average density $\bar{\rho}$ as function of substrate separation s_z for continuous model. Grand canonical ensemble Monte Carlo simulations were carried out for $T = 1.0$, $\mu = -11.5$, $s_x = 12.0$, $d_s = 4.0$, $\alpha s_x = 0.0$. Solid lines are intended to guide the eye.

(figure 4.3). In the lattice model positions of fluid molecules are restricted to sites of the simple cubic lattice (see section 2.1.2), where the lattice constant ℓ is equivalent to the diameter of a fluid molecule in the continuous model. Thus, we observe the local density only at *discrete* positions whose distances from the substrate surfaces are integer multiples of ℓ . Thus, applying this logic to $\rho(x, z)$ in the continuous model one would have to calculate it at points whose distance from the substrate surfaces is given in integer multiples of σ (provided $s_x/\sigma \in \mathbb{N}$). With such a coarse resolution in the z -direction one would, however, capture only maxima of $\rho(x, z)$ in the stratified region of the bridges therefore inevitably missing the nonmonotonic variation of $\rho(x, z)$ present only on a smaller lengthscale (i.e., a finer grid) as plots in figures 4.4(a) and 4.5 show. Since a lengthscale smaller than ℓ does not exist for the lattice model nothing can be said about stratification by definition.

Morphological changes with decreasing s_z , as illustrated by the sequence of plots in figures 4.4(a) – (c), may be cast in a more compact manner by

calculating the average density

$$\bar{\rho} := \frac{1}{s_x s_z} \int_{-s_x/2}^{s_x/2} dx \int_{-s_z/2}^{s_z/2} dz \rho(x, z) = \frac{\langle N \rangle}{V} \quad (4.4)$$

for various substrate separations s_z . A plot of $\bar{\rho}(s_z)$ in figure 4.6 exhibits two discontinuities. An analysis of $\rho(x, z)$ at $s_z \simeq 8.2$ permits one to conclude that at this substrate separation a first-order phase transition involving droplet and liquid phases occurs whereas the one at $s_z \simeq 7.5$ refers to a transition between a liquid and a bridge phase. Therefore, the sequence of phase transitions in figure 4.6 resembles precisely the scenario observed for the lattice gas shown in figure 4.1(b) and discussed above. Oscillations of $\bar{\rho}$ in figure 4.6 over the range $2 \leq s_z \leq 6$ reflect stratification of the confined fluid which becomes more pronounced the smaller s_z is.

However, investigations of phase transitions by Monte Carlo simulations in the spirit of figure 4.6 are frequently plagued by metastability, that is existence of a sequence of configurations $\{\mathbf{r}_k^N\}_{k=1, \dots, M}$ corresponding only to a *local* minimum of Ω where M can be quite substantial. In other words, the “lifetime” of a metastable thermodynamic state can be large compared with the time over which the microscopic evolution of the system can be pursued on account of limited computational speed. The origin of metastability is lack of ergodicity in the immediate vicinity of a first-order phase transition which arises on account of the microscopically small systems employed in computer simulations [98]. Metastability is manifest as hysteresis in a sorption isotherm (like the one plotted in figure 4.6), that is a range of finite width Δs_z around the true transition point over which for the same T and μ , $\bar{\rho}(s_z)$ is a double-valued function. To distinguish metastable from the thermodynamically (i.e. *globally*) stable phase one needs to compare Ω for the two states pertaining to different branches of the sorption isotherm at the same μ and s_z . The one having lowest Ω is the globally stable phase; the other one is only metastable. In figure 4.6 we plot only data for thermodynamically stable phases identified according to this rationale, where Ω was calculated from (3.21) during the Monte Carlo simulation.

4.1.2 Variation of chemical corrugation

Sorption experiments have clearly demonstrated that the phase behavior of confined fluids depends strongly on the degree of confinement (i.e, pore width) as far as nanoporous media are concerned [55]. It is thus conceivable that the stability of such a confined phase may also depend on the degree of chemical corrugation of the substrate. To investigate its impact on the phase diagram we define

$$c_r = \frac{n_s}{n_s + n_w} \quad (4.5)$$

as a quantitative measure of chemical corrugation.

Figure 4.7 shows phase diagrams for four different substrates of $c_r = 6/8$, $6/10$, $6/12$, $6/14$. In all cases the width of the strongly attractive substrate part $n_s = 6$ is maintained. Different degrees of corrugation, are therefore effected by varying the width of the weakly attractive strip n_w . The most surprising observation from figure 4.7 is that the droplet–bridge coexistence line $\mu_x^{\text{db}}(T)$ does not shift with c_r . Likewise the associated critical point $\{\mu_c^{\text{db}}, T_c^{\text{db}}\}$ remains nearly unaffected by a change of the width of the weakly attractive strip. On the contrary, the triple point $\{\mu_{\text{tr}}^{\text{dbl}}, T_{\text{tr}}^{\text{dbl}}\}$ exhibits a significant dependence on c_r leaving, however, the chemical potential at the triple point $\mu_{\text{tr}}^{\text{dbl}}$ roughly unchanged since $\mu_x^{\text{db}}(T)$ is nearly parallel to the temperature axis. The variation of the triple point temperature $T_{\text{tr}}^{\text{dbl}}$ is related to a shift of the droplet-liquid and the bridge-liquid coexistence lines $\mu_x^{\text{dl}}(T)$ and $\mu_x^{\text{bl}}(T)$, respectively, to lower chemical potentials as n_w decreases. For $c_r = 6/8$, $\mu_x^{\text{dl}}(T)$ eventually shifts to lower chemical potentials compared with the chemical potential at the droplet-bridge critical point, that is $\mu_x^{\text{dl}}(T) < \mu_c^{\text{db}}$. Therefore, this system does not have a thermodynamically stable bridge phase.

The degree of corrugation also affects the succession of phase transitions if the substrate separation is varied at constant c_r following the discussion in section 4.1.1. Consider, for example, the case $c_r = 6/8$. Here the one–phase region of the bridge phase disappeared completely. Suppose T and μ are chosen such that the point $\{T, \mu\}$ is located slightly below $\mu_x^{\text{dl}}(T)$. Decreasing n_z causes $\mu_x^{\text{dl}}(T)$ to move down in chemical potential (see figure 4.1 in section 4.1.1). Thus, the system undergoes a first order phase transition from the droplet to the liquid phase. If n_w is sufficiently small (i.e. c_r is sufficiently large) no stable bridge

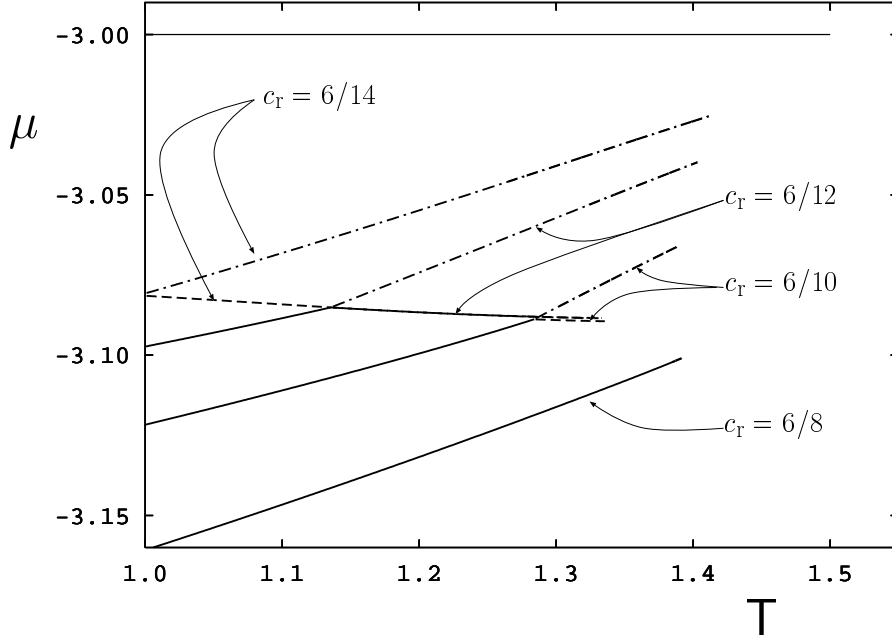


Figure 4.7: As figure 4.1, but for various corrugation c_r indicated in figure (4.1) ($\alpha = 0$, $n_x = 14$, $n_z = 8$, $\epsilon_{fs} = 1.4$ and $\epsilon_{fw} = 0.3$) (—) $\mu_x^{dl}(T)$, (---) $\mu_x^{db}(T)$, (- · -) $\mu_x^{bl}(T)$. Corresponding bulk coexistence curve is also shown.

phase appears in the phase diagram even for smaller n_z . Therefore, the system remains in its liquid state for all smaller values of n_z . For c_r below a certain threshold ($c_r = 6/8$ in figure 4.7) a one-phase region of bridges appears and increases in size with decreasing c_r . Consider now a system where $c_r = 6/14$ and a point $\{T, \mu\}$ below $\mu_x^{db}(T)$. Decreasing n_z then causes the one-phase region of the bridges to widen, while the entire phase diagram moves downward (see figure 4.1). Thus the initial droplet phase is transformed into a bridge phase as the state point $\{T, \mu\}$ crosses the line of first order phase transition, that is $\mu_x^{db}(T)$. Decreasing n_z further results in an even wider one-phase region of bridges. Thus, for all smaller n_z the state point remains in that one-phase region.

To confirm these conjectures we turn to the continuous model where we calculate isotherms $\bar{\rho}(s_z)$ for several systems confined by differently corrugated substrates (see figure 4.8). As before for the lattice model we fix the width of the strongly attractive stripe, $d_s = 4$, and vary the corrugation over the range

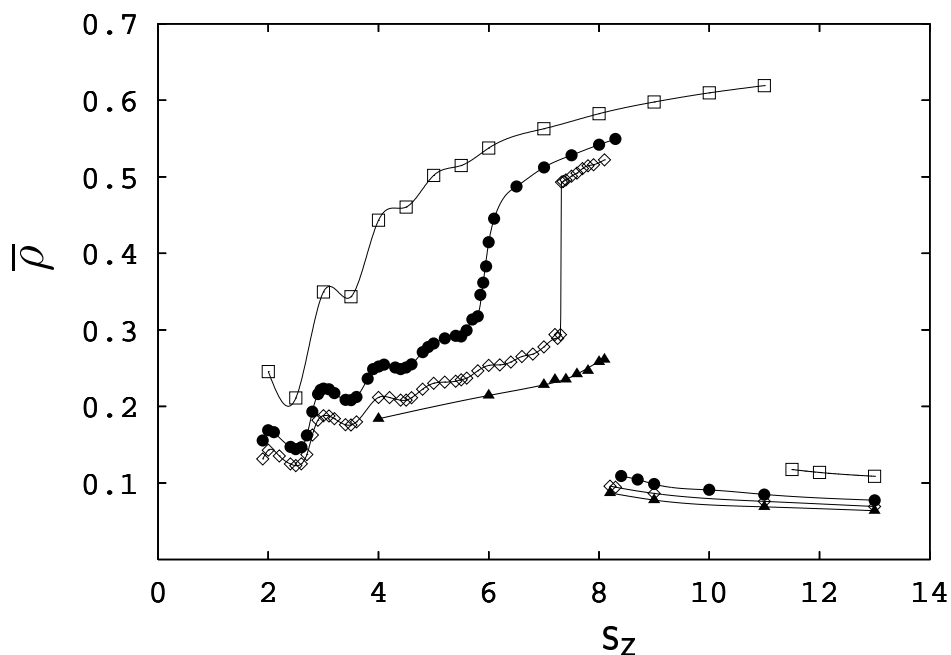


Figure 4.8: Mean density $\bar{\rho}$ as a function of substrate separation s_z and various degrees of chemical corrugation of substrate $c_r = 4/7$ (\square), $c_r = 4/10$ (\bullet), $c_r = 4/12$ (\diamond), and $c_r = 4/14$ (\blacktriangle). Solid lines are intended to guide the eye.

$4/14 \leq c_r \leq 4/7$. At large wall separations $s_z \gtrsim 11$ all systems exhibit similar (low) mean densities $\bar{\rho}$ indicating that the thermodynamically stable state of all systems in that region is the droplet phase. However, as s_z decreases different effects are detected. The system having the highest value $c_r = 4/7$, undergoes a discontinuous phase transition from the droplet to the liquid phase at a wall separation $s_z \simeq 11$, as the plot in figure 4.8 shows. (That the higher density state at the discontinuous change in $\bar{\rho}(s_z)$ is, in fact, liquidlike was confirmed by an inspection of the local density of the confined fluid, see above.) Because of the reduced *net* attraction as c_r decreases, all other systems exhibit this transition (known as capillary condensation) but at smaller s_z . For the system having the lowest value of the corrugation $c_r = 4/14$, only partial condensation is observed. That is at $s_z \simeq 8.3$ the initial droplet phase undergoes a discontinuous phase transition to form a bridge phase, thereby confirming the predictions of the parallel lattice gas calculations.

For $c_r = 4/10$ a steep but continuous decay of $\bar{\rho}$ around $s_z = 6$, is observed.

As shown in [94] the isothermal compressibility exhibits a cusp-like maximum in the vicinity of $s_z \simeq 6$ indicating large density fluctuations. Applying finite-size scaling arguments [79] it was concluded in [94] that over the range $5.5 \leq s_z \leq 6.5$ the thermodynamic state of the confined fluid may be in the vicinity of the bridge-liquid critical point.

4.1.3 The impact of shear strain

The preceding sections clearly illustrate the complex dependence of the stability of bridge phases on both confinement and chemical corrugation. If the substrates are perfectly aligned (i.e. $\alpha s_x = 0$) a bridge phase is characterized by a high-density regime spanning the gap between the strongly attractive parts of the opposing substrates [see figure 4.9(a)]. Intuitively one expects these structures to be capable of resisting shear deformations to a certain degree. A shear strain may be applied to a bridge phase by misaligning the corrugated substrates. The plots in figure 4.9(a) and figure 4.9(b) illustrate the effect of applying a shear strain $\alpha s_x > 0$ to a typical bridge phase. Depending on the thermodynamic state a bridge phase will sustain a maximum shear strain but will eventually be either “torn apart” and undergo a first-order phase transition to a droplet phase [see figure 4.9(c)] or condense and form a liquid phase [see figure 4.9(d)]. Corresponding phase diagrams $\mu_x(T)$ plotted in figure 4.10 show that upon increasing α from its initial value of zero causes the triple point to shift to higher $T_{\text{tr}}^{\text{dbl}}$ and $\mu_{\text{tr}}^{\text{dbl}}$. Simultaneously, the one-phase region of bridge phases shrinks. The one-phase regime of bridge phases may, however, vanish completely for some $\alpha < \alpha_{\text{max}}$ depending on substrate separation (i.e., n_z), chemical corrugation (i.e., c_r), or strength of interaction with the chemically different parts of the substrate (i.e., ϵ_{fw} , ϵ_{fs}). Notice that for the special case $\alpha_{\text{max}} = 1/2$ (i.e., n_x even) the one-phase region of bridge phases *must* vanish in the limit $\alpha = \alpha_{\text{max}}$ for symmetry reasons. In addition, figure 4.10 shows that critical temperatures T_c^{bl} and T_c^{db} depend only weakly on the shear strain unlike μ_c^{bl} and μ_c^{db} such that the critical points are essentially shifted upwards and downwards, respectively, as α increases.

Consider now a specific isotherm $T = \{(\mu, T_T) | T_T = 1.25\}$ in figure 4.10, intersecting with different branches of the (same) phase diagram $\mu_x(T)$ at dif-

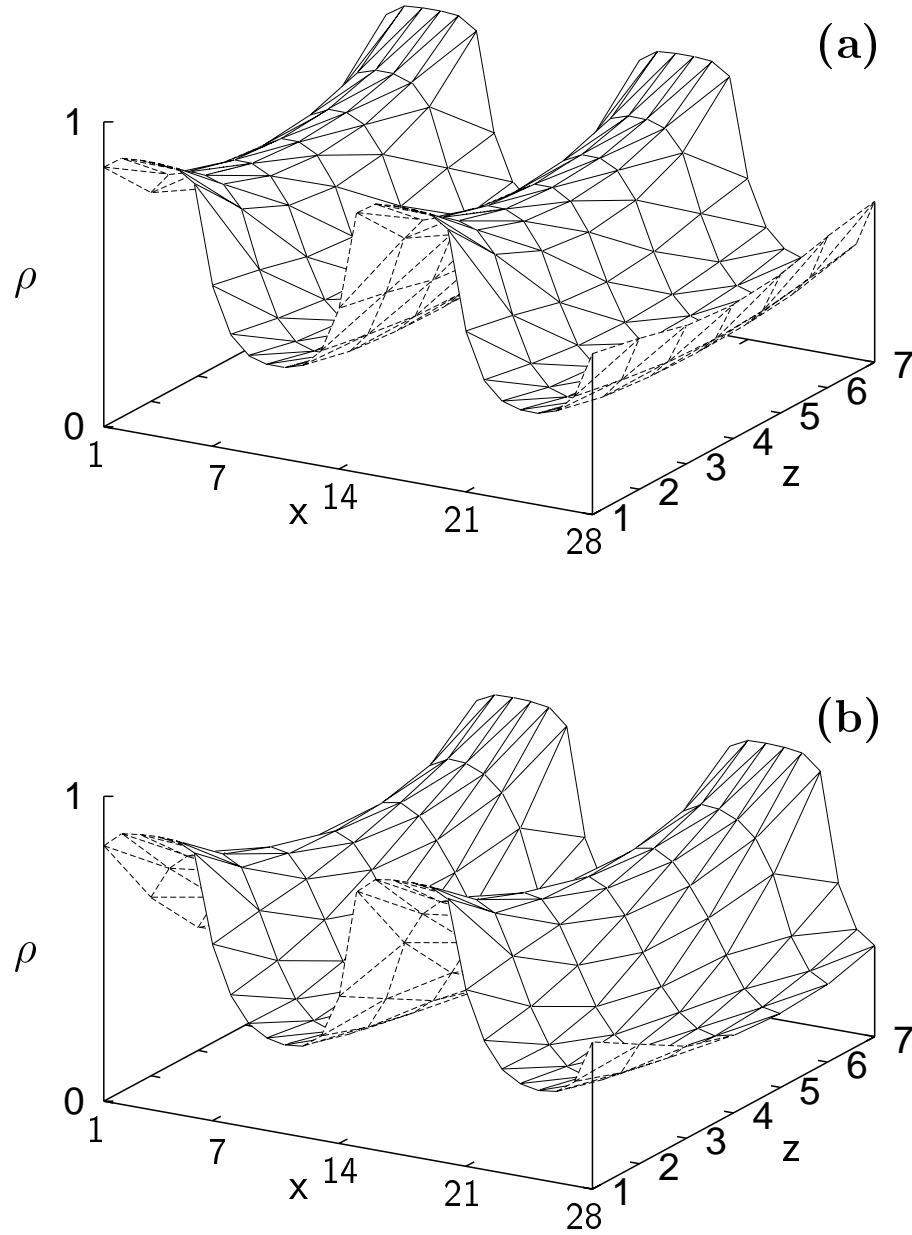


Figure 4.9: Local density $\rho(x, z)$ for confined lattice at $T = 1.25$, $\mu = -3.03658$. Substrates are characterized by $n_x = 14$, $n_z = 7$, $n_w = 8$, $n_s = 6$, $\epsilon_{fw} = 0.4$, and $\epsilon_{fs} = 1.6$. (a) bridge phase ($\alpha = 0$), (b) bridge phase ($\alpha = 5/14$), (c) droplet phase ($\alpha = 1/2$), (d) liquid phase ($\alpha = 1/2$). Plots in (c) and (d) correspond to coexisting phases (see figure 4.10). Two periods of $\rho(x, z)$ in the x -direction are shown because of periodicity of the lattice model (see section 2.1.2).

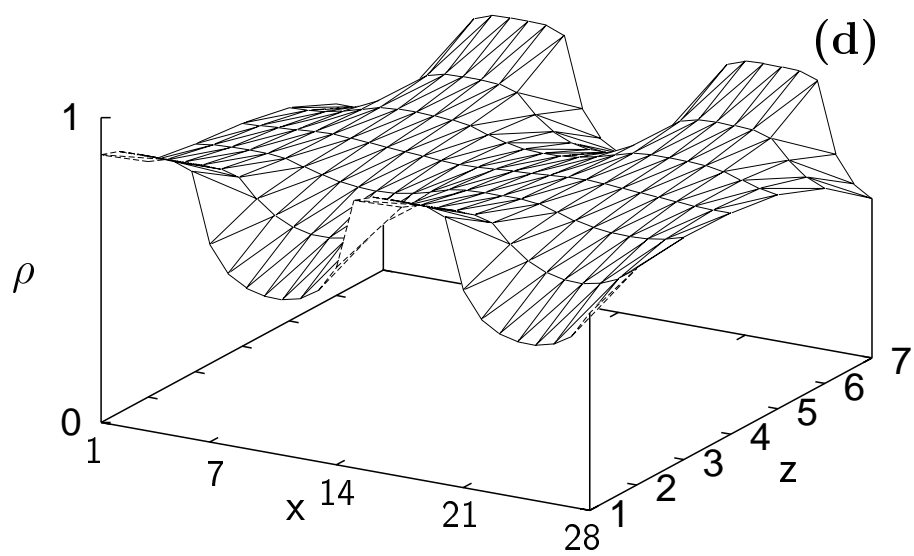
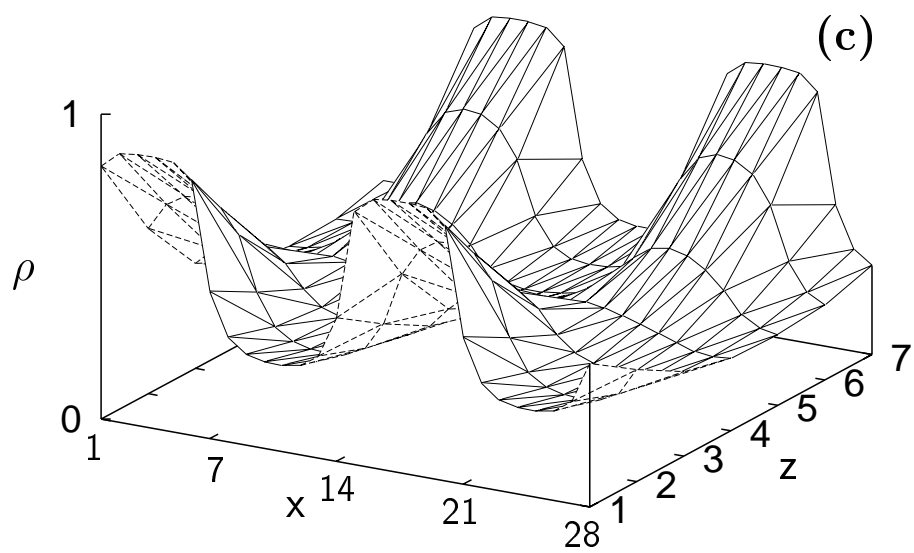


Figure 4.9: (Continued)

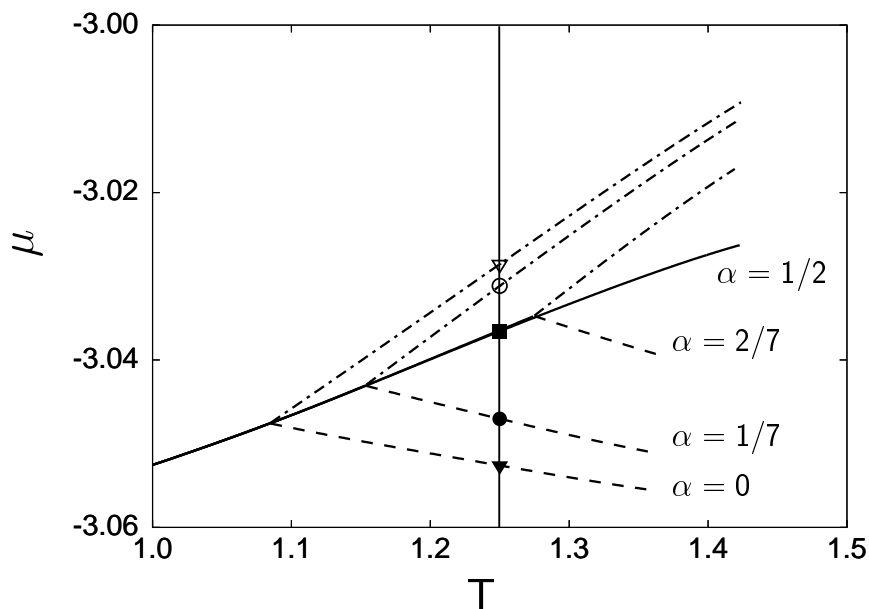


Figure 4.10: As figure 4.1, but for various shear strains α indicated in figure ($n_x = 14$, $n_s = 6$, $n_z = 7$, $\epsilon_{fs} = 1.6$, $\epsilon_{fw} = 0.4$). Intersections between isotherm T (vertical solid line, see text) and coexistence–curve branches represent coexisting phases. (▼) $\mu_x^{gb}(T_T)$, (∇) $\mu_x^{bl}(T_T)$, $\alpha = 0$; (●) $\mu_x^{gb}(T_T)$, (○) $\mu_x^{bl}(T_T)$, $\alpha = 1/7$; (■) $\mu_x^{gl}(T_T)$, $\alpha = 2/7$.

ferent chemical potentials. According to the definition of $\mu_x(T)$, (2.114) each intersection corresponds to a pair of (separately) coexisting phases. For example, at $\mu_x^{db}(T_T) \simeq -3.053$ and $\alpha = 0$ a droplet phase coexists with a (more dilute) bridge phase whereas a (denser) bridge phase coexists with a liquid phase for $\mu_x^{bl}(T_T) \simeq -3.029$. Because the one–phase region of bridge phases shrinks with α (see figure 4.10), the “distance” $\Delta\mu_x(T_T) := |\mu_x^{gb}(T_T) - \mu_x^{bl}(T_T)| \rightarrow 0$ the larger α becomes, that is with increasing shear strain. From the plot in figure 4.10 it is clear that a shear strain exists such that $\Delta\mu_x = 0$, that is $T_T \leq T_{tr}^{dbl}(\alpha n_x)$. For this and larger shear strains only a single intersection remains, corresponding to coexisting droplet and liquid phases (see figure 4.10).

If the confined fluid in the continuous model is exposed to a shear strain, it undergoes structural transformations similar to the ones just discussed for the

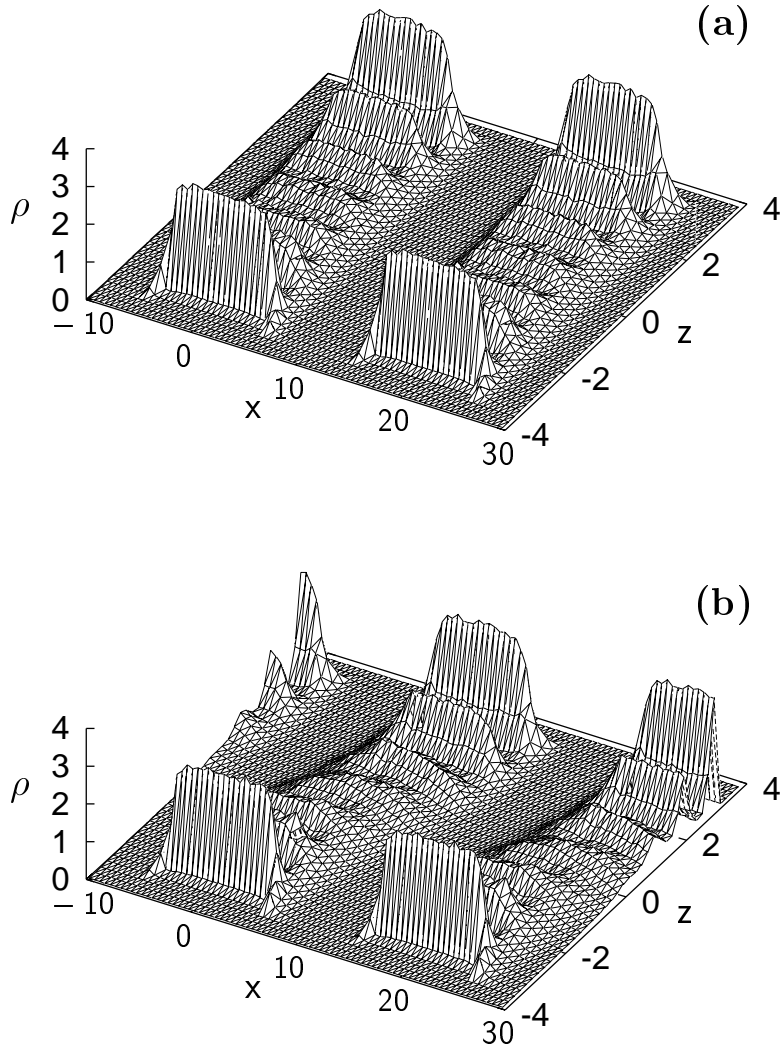


Figure 4.11: As figure 4.9, but for continuous model. Plots show two periods of $\rho(x, z)$ in the x -direction because of periodic boundary conditions. (a) unsheared bridge phase, $\alpha s_x = 0.0$; (b) sheared bridge phase, $\alpha s_x = 7.5$; (c) droplet phase, $\alpha s_x = 10.0$; (d) liquid phase, $\alpha s_x = 10.0$. Plots in (c) and (d) correspond to coexisting phases. In all cases $T = 0.7$, $\mu = -8.15$, $s_x = 20.0$, $d_s = 10.0$, and $s_z = 8.0$.

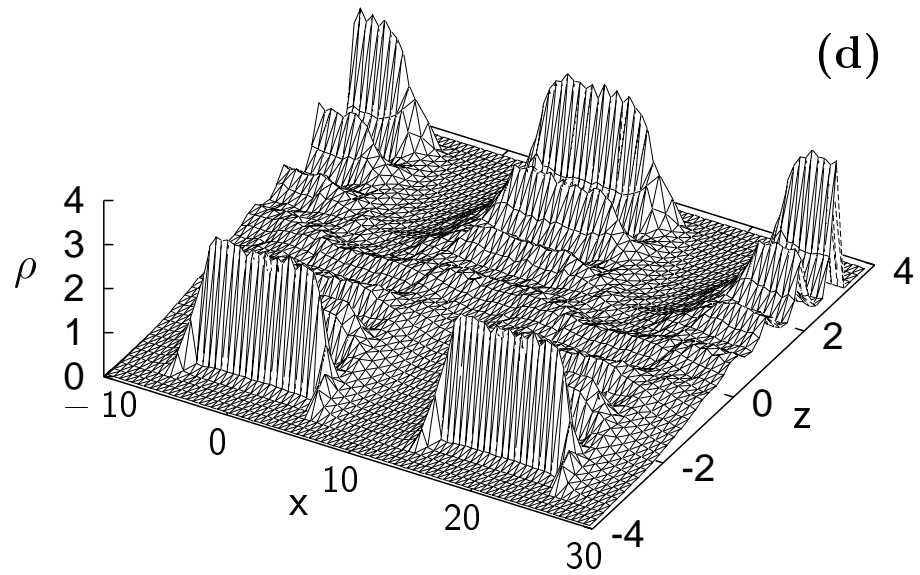
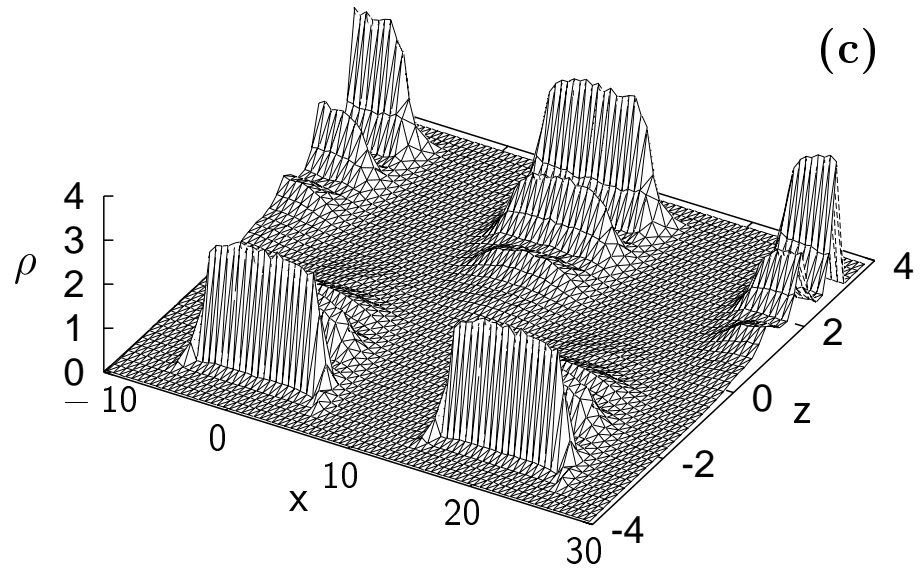


Figure 4.11: (Continued)

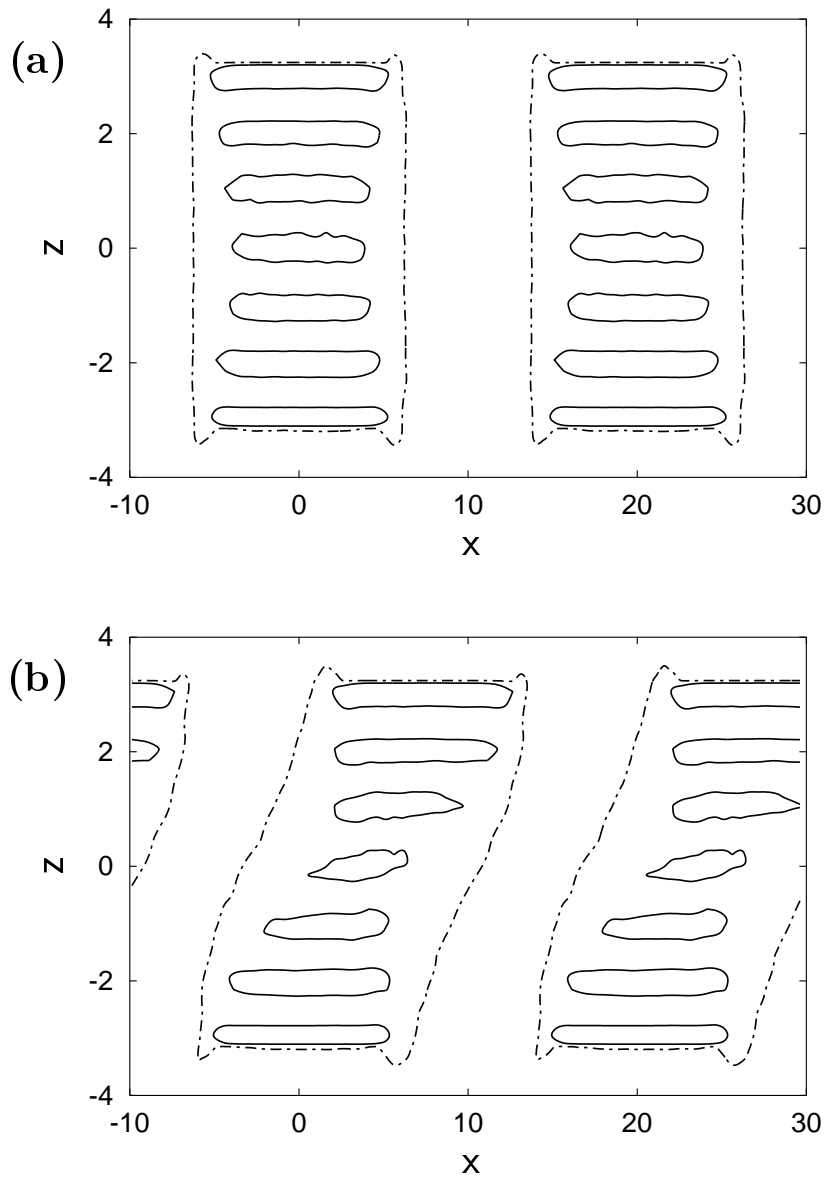


Figure 4.12: Contour lines $\rho(x, z) = 0.10$ ($-\cdot-$), 0.75 ($—$) corresponding to plots in figure 4.11.

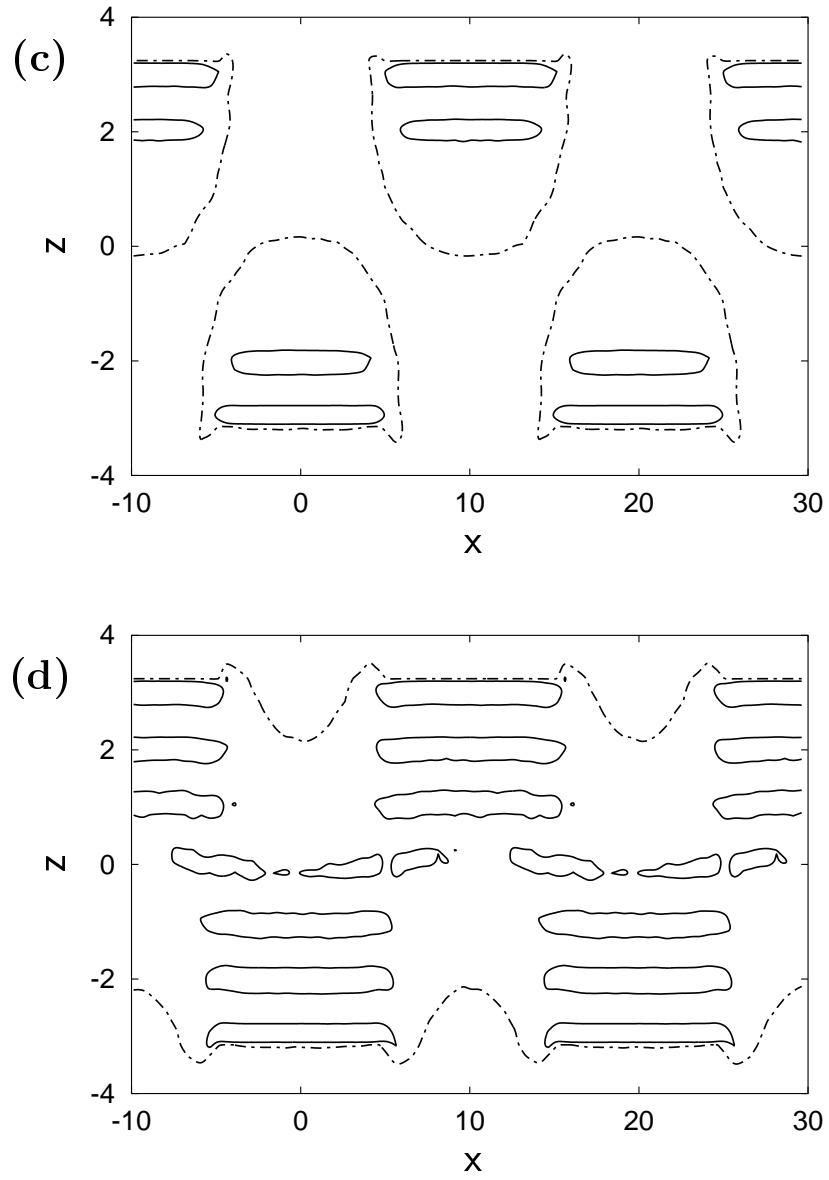


Figure 4.12: (Continued)

lattice gas. For example, a bridge phase can sustain a shear strain [see figure 4.11(a), figure 4.11(b)]. Comparing the corresponding contour plots in figure 4.12(a) and figure 4.12(b) one sees that as a result of the applied deformation, centers of molecular strata are displaced in the $+x$ -direction. If the shear strain exceeds a certain threshold one expects from the lattice-gas results (see figure 4.10) that the bridge phase undergoes a first-order phase transition. Depending on the “position” of the thermodynamic state with respect to $\mu_x^{\text{gb}}(T)$ and $\mu_x^{\text{bl}}(T)$ either a droplet or a liquid phase may form as a result. Both situations are realized as plots in figure 4.11(c) and figure 4.11(d) reveal.

Because of the similarity between the lattice-gas calculations and the Monte Carlo simulations for the continuous model, it seems instructive to study the phase behavior in the latter if the confined fluid is exposed to a shear strain. This may be done conveniently by calculating $\bar{\rho}$ [see (4.4)] as a function of μ and αs_x . Because of the microscopic size of the simulation cell, results are again affected by metastability in the immediate vicinity of a phase transition. To identify coexisting phases along a sorption isotherm we adopt the procedure described above in section 4.1.1.

For sufficiently low $\mu < \mu_x^{\text{dbl}}(T_T)$ one expects a droplet phase to exist along a subcritical isotherm $\mathbb{T} = \{(\mu, T) | T_{\text{tr}} < T_T < \min(T_c^{\text{gb}}, T_c^{\text{bl}}), T_T = \text{const}\}$ (see figure 4.10). At an intersection between \mathbb{T} and $\mu_x^{\text{db}}(T)$ the droplet phase will undergo a spontaneous transformation to a bridge phase. In a corresponding plot of $\bar{\rho}$ versus μ one should see a discontinuous jump to a higher density. Eventually, another intersection between \mathbb{T} and $\mu_x^{\text{bl}}(T)$ exists and a second discontinuous jump to an even higher value of $\bar{\rho}$ should be visible in that plot. Both of these transitions are indeed observed in figure 4.13 for $\alpha s_x = 0$, $\mu \simeq -8.40$, and $\mu \simeq -7.98$, respectively. Notice that in figure 4.13, $\mu_x^{\text{bl}}(T_T)$ for $\alpha s_x = 0.0$ exceeds its bulk counterpart $\mu_x^{\text{bulk}}(T_T)$, that is for $\mu_x^{\text{bl}}(T_T)$ the corresponding bulk phase is liquid. This can be rationalized by noting that the low(er)-density part of a bridge phase is predominantly involved in this second transition. Recall also that this part of a bridge phase is stabilized by the *weak* portions of both (perfectly aligned) substrates characterized by $\epsilon_{\text{fw}} \ll \epsilon_{\text{ff}}$. Hence, the second first-order transition is inhibited rather than supported by the substrates (with respect to the bulk) because of the dominating repulsive interaction of a fluid

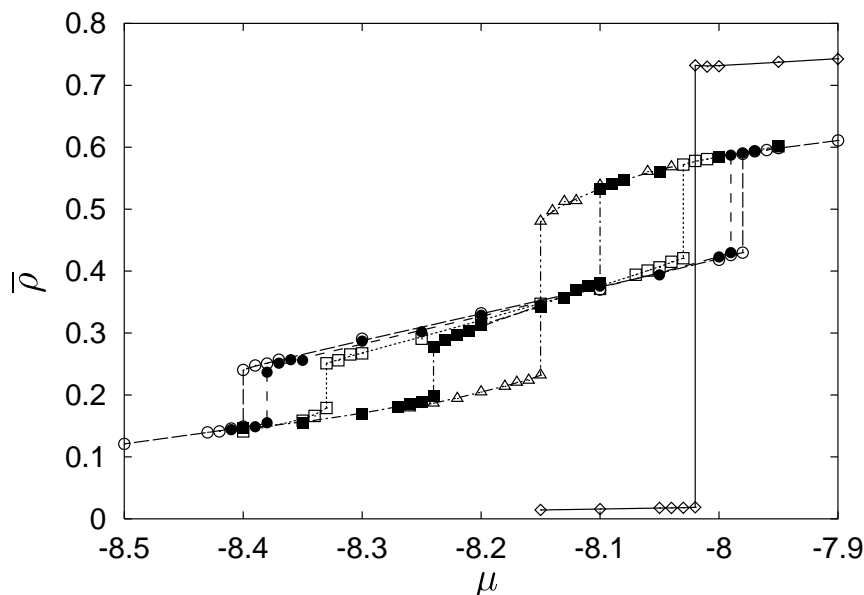


Figure 4.13: Sorption isotherms $\bar{\rho}(\mu)$ from grand canonical ensemble Monte Carlo simulations (continuous model); (\circ), (---) $\alpha s_x = 0.0$; (\bullet), (---): $\alpha s_x = 2.5$; (\square), (\cdots): $\alpha s_x = 5.0$; (\blacksquare), ($-\cdot-$): $\alpha s_x = 7.5$; (\triangle), ($-\cdot-$): $\alpha s_x = 10.0$. Also shown are corresponding bulk data (\diamond), (—). Results were obtained for $T = 0.7$, $s_x = 20.0$, $d_s = 10.0$, and $s_z = 8.0$.

molecule with the weak part of the substrate.

If a shear strain is applied, the region of overlap of the weak substrate parts in the x -direction shrinks [see figure 3.1 and (3.10)] such that a fluid molecule located at $\{x | d_s/2 \leq |x| \leq s_x/2, \alpha s_x = 0.0\}$ is exposed to a stronger net fluid-substrate attraction. Consequently, one expects an associated shift of $\mu_x^{\text{bl}}(T_T)$ to lower values. The plot in figure 4.13 confirms the expectation. In addition, figure 4.10 shows that the one-phase region shrinks because $T_{\text{tr}}^{\text{dbl}}$ shifts to higher temperatures and because the slope of the coexistence lines does not change much. The plot in figure 4.10 therefore suggests that for $\alpha > 0$ the two discontinuities in $\bar{\rho}(\mu)$ approach each other so that the branch of $\bar{\rho}(\mu)$ pertaining to bridge phases becomes narrower with increasing αs_x . This effect is indeed visible in figure 4.13 where the width of the intermediate-density branch of $\bar{\rho}(\mu)$ (corresponding to thermodynamically stable bridge phases) diminishes

from $|\Delta\mu| \simeq 0.42$ ($\alpha s_x = 0.0$) to $|\Delta\mu| \simeq 0.14$ ($\alpha s_x = 7.5$). Finally, if the shear strain is large enough, the lattice-gas results in figure 4.10 suggest that for a given temperature T_T , $T_{\text{tr}}^{\text{dbl}}(\alpha s_x) > T_T$ for sufficiently large shear strains (see the curve for $\alpha = 2/7$ in figure 4.10). Hence, under these circumstances one would expect $\bar{\rho}(\mu)$ to exhibit just a single discontinuity referring to a phase transition between droplet and liquid phases. The plot in figure 4.13 for $\alpha s_x = 10$ confirms this notion.

4.2 Thermo-mechanical properties

4.2.1 Shear stress of confined fluids

Thermodynamic stability of bridge phases turned out to depend on system parameters (c_r , n_z , ϵ_{fs} , ϵ_{fw}) determining the influence of substrate heterogeneity on the fluid film. Now we focus on mechanical stability and thermomechanical properties of the confined phases. From figure 4.12(a) the local density of bridge phases appears to be inhomogeneous in a direction (x) perpendicular to the substrate heterogeneities for all distances between the walls (i.e., along lines $z = \text{const}$). Comparing figure 4.12(a) with figures 4.12(c) and (d) one realizes that fluid and droplet phases differ from bridge phases significantly in that they both exhibit a central region where the respective local densities are approximately independent of x , that is, gas and liquid phases are approximately homogeneous in this central region. Thus, in the latter two phases the walls can slide more or less freely over one another without substantial resistance, because their homogeneous portions cannot sustain shear deformations. If, on the other hand, the confined fluid is capable of connecting only certain parts of the substrates by fluid, as the fluid bridges do (see figure 4.12(a) and (b)), the confined phases may sustain shear deformations, that is exhibit a nonvanishing shear stress (T_{zx}).

To extract thermomechanical properties within the continuous model, we apply Monte Carlo simulations in the grand mixed isostress-isostrain ensemble (see section 3.4). Under the present thermodynamic conditions, $T = 1.0$, $\mu = -11.455$, $T_{zz} = 0.0$, and $2.0 \leq d_s \leq 8.0$ the confined fluid forms a bridge phase for various values of αs_x . The key quantity calculated in the present Monte Carlo simulations is the stress curve $T_{zx}(\alpha s_x)$ accessible *via* (3.64), (3.65) and

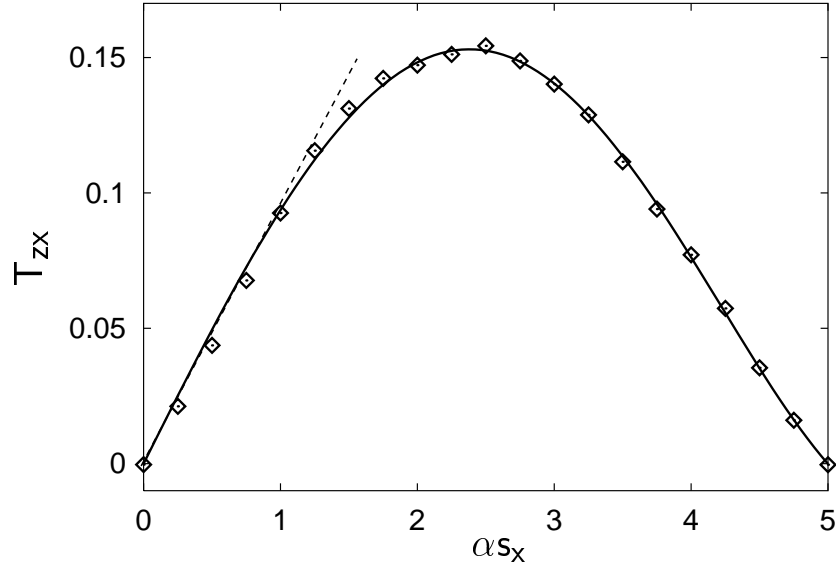


Figure 4.14: Typical stress curve $T_{zx}(\alpha s_x)$ for a monolayer bridge phase and $c_r = 5/10$. Solid line is a least-squares fit of a polynomial to the (discrete) Monte Carlo data points (\diamond) intended to guide the eye. The dashed line has been included to emphasize the Hookean behavior at small strains.

the alternative expressions in (3.72). Regardless of the thermodynamic state and the thickness (i.e., s_z) of a bridge phase, a typical stress curve plotted in figure 4.14 exhibits the following features:

1. For vanishing shear strain (i.e., $\alpha = 0$), $T_{zx}(0) \equiv 0$ for symmetry reasons.
2. $T_{zx}(\alpha s_x)$ depends linearly on the shear strain αs_x in the limit $\alpha \rightarrow 0$, that is the response of the bridge phase to small shear strains follows Hooke's law.
3. For larger shear strains, negative deviations from Hooke's law are observed, eventually leading to a yield point $(\alpha^{yd}, T_{zx}^{yd})$ defined by the constitutive equation

$$\left(\frac{\partial T_{zx}}{\partial (\alpha s_x)} \right)_{T, \mu, s_x, s_y, T_{zz}} \Big|_{\alpha = \alpha^{yd}} = 0 \quad (4.6)$$

or, alternatively using the shear modulus [see (3.78)],

$$c_{44}(\alpha^{yd} s_x) = 0, \quad \text{fixed } T, \mu, s_x, s_y, T_{zz}. \quad (4.7)$$

4. For symmetry reasons, $T_{zx}(s_x/2) \equiv 0$ (i.e., for $\alpha = 1/2$).

These general characteristics of stress curves have also been observed previously in simulations of “simple”-fluid films confined between chemically homogeneous but atomically structured (i.e., discrete) substrates [86, 98, 99, 100, 101, 102, 103, 104, 105, 106, 107, 108]. The substrates were composed of a single layer of Lennard-Jones atoms arranged according to a plane of the face-centered cubic lattice. In the earlier studies the unstrained phase was solidlike on account of a template effect imposed on the confined fluid by the discrete nature of the substrate material. No solidification occurs here under the present thermodynamic conditions.

The impact of substrate corrugation.

However, as far as the present model is concerned, the degree of chemical corrugation of the substrate c_r [see (4.5)] has significant consequences for the yield-point location $(\alpha^{yd}, T_{zx}^{yd})$. Plots of stress curves for various values of c_r are shown in figure 4.15(a). For monolayer bridge phases and fixed $s_x = 10$ one can see from figure 4.15(a) that both T_{zx}^{yd} and α^{yd} are smallest for the smallest $c_r = 2/10$. For $c_r < 2/10$ only droplet phases are thermodynamically stable because the strongly attractive portion of the substrate is too narrow to support formation of denser (bridge) phases. As c_r increases both T_{zx}^{yd} and α^{yd} increase until they reach their maximum values $(\alpha^{yd} s_x, T_{zx}^{yd}) \approx (2.740, 0.169)$ for $c_r = 5/10$. For larger $c_r > 5/10$ the plots in figure 4.15(a) show that both T_{zx}^{yd} and α^{yd} decrease again until $(\alpha^{yd} s_x, T_{zx}^{yd}) \approx (1.550, 0.069)$ for $c_r = 8/10$ which is the largest substrate corrugation for which bridge phases were observed. For $c_r > 8/10$ only thermodynamically stable liquid phases formed in the simulations, incapable of sustaining a shear strain.

One also notices from figure 4.15(a) that stress curves for $c_r = 2/10, 3/10,$ and $4/10$ apparently do not cover the entire range of shear strains. In these cases the bridge phase undergoes a shear-induced phase transition at some threshold $\alpha^c s_x$ to form a droplet phase (see discussion in section 4.1.3). This droplet phase, by virtue of its microscopic structure [see figure 4.12(c)], is incapable of sustaining a shear stress. Thus, at $\alpha^c s_x, T_{zx}$ drops to zero discontinuously such that $T_{zx} \equiv 0$ for all $\{\alpha | \alpha^c \leq \alpha \leq 1/2\}$. For the sake of clarity we do not plot

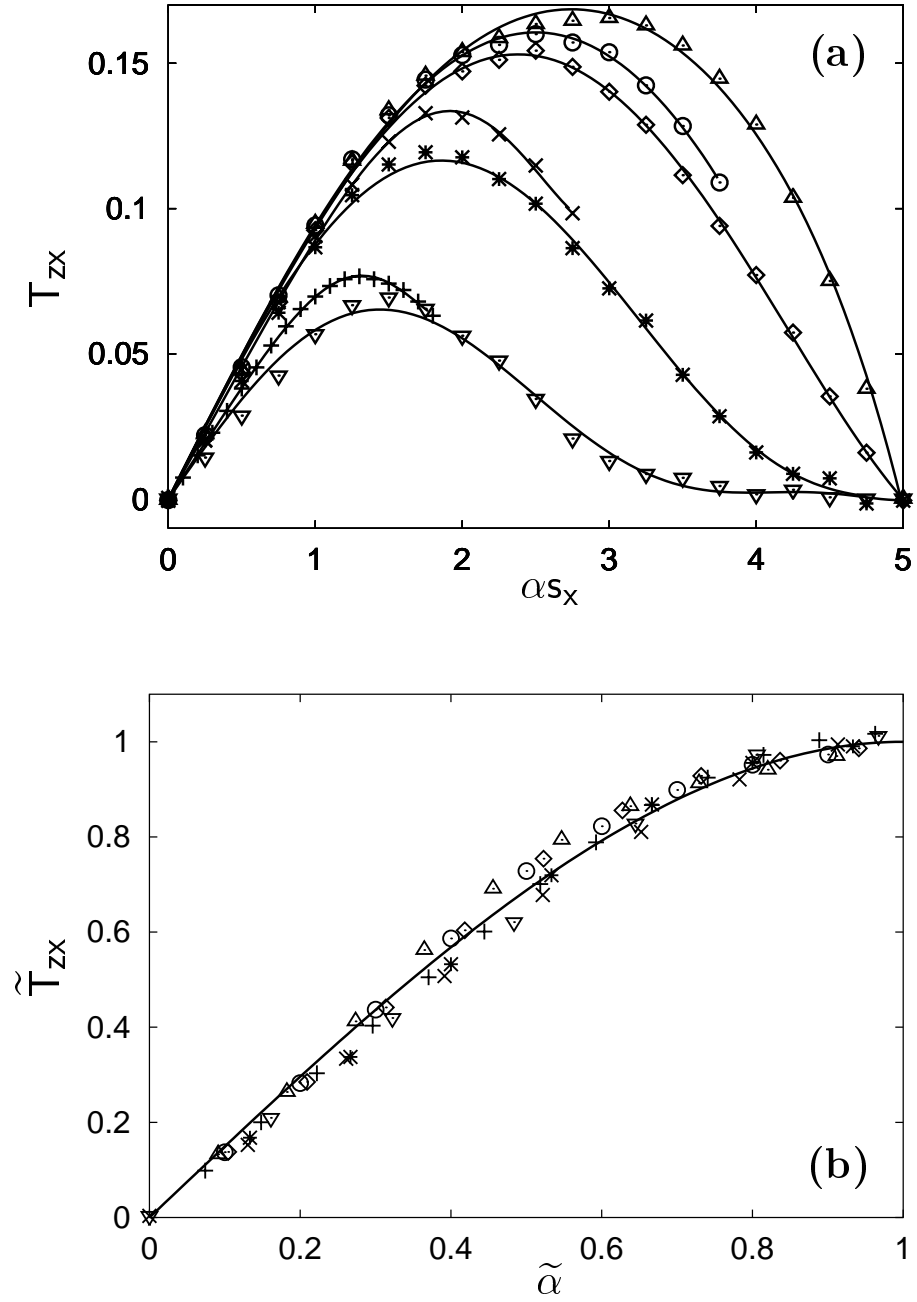


Figure 4.15: (a) Stress curve $T_{zx}(\alpha s_x; c_r)$ for various chemical corrugations $c_r = 2/10$ (+), $3/10$ (\times), $4/10$ (\circ), $5/10$ (Δ), $6/10$ (\diamond), $7/10$ (*), $8/10$ (∇). Solid lines are intended to guide the eye. (b) Reduced stress curve $\tilde{T}_{zx}(\tilde{\alpha}; c_r)$ [see (4.8)] where symbols are referring to data plotted in (a). The solid line is a representation of (4.13).

this part of the stress curves in figure 4.15(a).

Despite this nonmonotonic variation of the yield–point location with c_r it turns out that within the theory of corresponding states (see section 12-7 in [82]) it is feasible to renormalize stress curves such that all data points fall onto a unique master curve. Renormalization is effected by introducing dimensionless variables

$$\begin{aligned} \alpha s_x &\rightarrow \tilde{\alpha} := \frac{\alpha s_x}{\alpha^{yd} s_x} \\ T_{zx} &\rightarrow \tilde{T}_{zx}(\tilde{\alpha}) := \frac{T_{zx}(\tilde{\alpha})}{T_{zx}^{yd}}. \end{aligned} \quad (4.8)$$

Normalization by α^{yd} and T_{zx}^{yd} is consistent with the theory of corresponding states because it was pointed out in [86] that the yield point may be perceived as a shear critical point analogous to the liquid–gas critical point in one–component homogeneous fluids. If the simulation data plotted in figure 4.15(a) are renormalized according to this recipe, they can indeed be represented by a master curve as the plot in figure 4.15(b) shows.

Universality of stress curves.

The remarkable insensitivity of $\tilde{T}_{zx}(\tilde{\alpha})$ in figure 4.15(b) to variations of c_r (3.78) can be rationalized as follows. Because of the Hookean regime in the limit $\alpha s_x \rightarrow 0$, c_{44} should be approximately constant and positive in this limit. A typical plot in figure 4.16 confirms this notion. However, because of (4.7) one expects c_{44} to decline from its Hookean value as $\alpha s_x \rightarrow \alpha^{yd} s_x$ also in agreement with figure 4.16. Furthermore, since figure 4.16 shows that the variation of c_{44} with αs_x is not too strong over the range $\{\alpha \mid 0 \leq \alpha \leq \alpha^{yd}\}$, it seems sensible to expand c_{44} in a power series according to

$$c_{44}(\alpha s_x) = \sum_{k=0}^{\infty} \frac{1}{k!} \left. \frac{d^{(k)} c_{44}}{d(\alpha s_x)^k} \right|_{\alpha=0} (\alpha s_x)^k = \sum_{k=0}^{\infty} a_k (\alpha s_x)^k \simeq a_0 + a_2 (\alpha s_x)^2 \quad (4.9)$$

where we refer to the far right side as the small–strain approximation. Notice that the set of coefficients $\{a_k\}$ refer to the *unstrained* bridge phase (i.e., $\alpha = 0$). A molecular expression for $a_0 \equiv c_{44}(0)$ is given in (3.78). In the small–strain approximation a_2 accounts for deviations from Hookean behavior and may therefore be interpreted as a measure of plasticity of the unshered confined film.

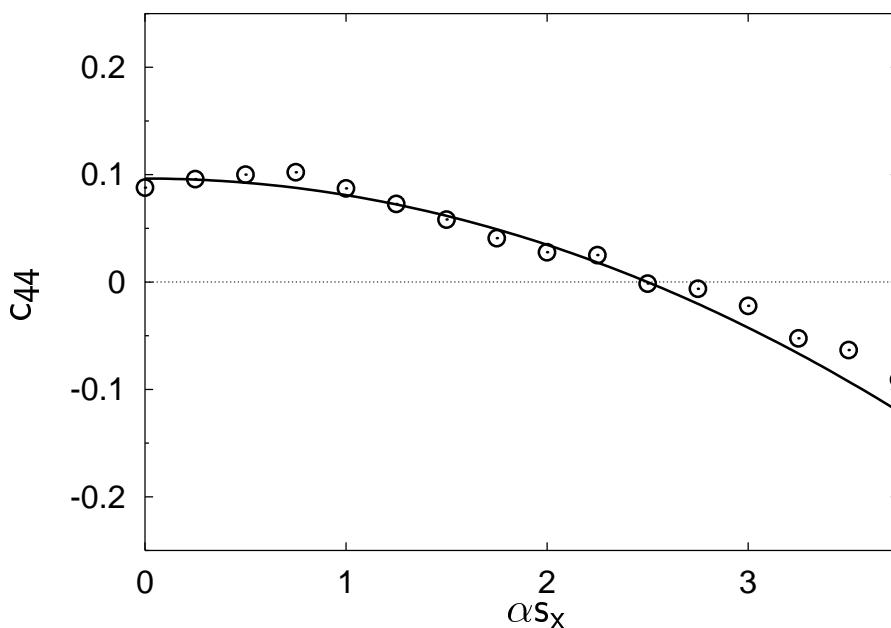


Figure 4.16: Shear modulus c_{44} as function of shear strain αs_x . (\circ): Monte Carlo simulations in grand mixed stress-strain ensemble; (—): representation of small-strain approximation $c_{44}(\alpha s_x) = a_0 + a_2(\alpha s_x)^2$ [see (4.9), (4.10)]. Note: systems having negative values of c_{44} are mechanically unstable.

The vanishing of the coefficients a_{2k-1} ($k = 1, \dots, \infty$) in (4.9) can be rationalized by symmetry considerations. As detailed in appendix B the x -component of the force exerted by the walls on a fluid molecule is an odd function of x . For the two highly symmetric cases $\alpha = 0$ and $\alpha = 1/2$, respectively, the probability density of the grand mixed isostress-isostrain ensemble $f_0(s_z, N, \mathbf{r}^N)$ [see (3.52)] is symmetric with respect to the plane $x = 0$. Therefore $\langle F_x^{[k]} \rangle \equiv 0$, $k = 1, 2$. Thus from the definition of $\{a_k\}$ in (4.9) and (3.77) it is furthermore clear that for $\alpha = 0$, $a_{2k-1} \equiv 0$ ($k = 1, \dots, \infty$). However, we note in passing that these coefficients do not vanish *a priori* for $\alpha \neq 0$ since the $f_0(s_z, N, \mathbf{r}^N)$ is asymmetric in this case. From (3.77) and (4.9) we obtain the (shear stress) equation of state

$$T_{zx}(\alpha s_x) = \int_0^{\alpha s_x} d(\alpha' s_x) c_{44}(\alpha' s_x) \simeq a_0 \alpha s_x + \frac{1}{3} a_2 (\alpha s_x)^3 \quad (4.10)$$

Table 4.1: Comparison of shear modulus c_{44} from molecular expression and yield-point location.

c_r	$\langle s_z \rangle$	$\alpha^{yd} s_x$	T_{zx}^{yd}	From (4.11)	From (3.78)
				$c_{44}(0)$	$c_{44}(0)$
2/10	2.113	1.350	0.075	0.084	0.079
4/10	2.075	2.499	0.161	0.096	0.088
4/10	3.057	2.588	0.101	0.058	0.060
5/10	2.069	2.743	0.169	0.092	0.101
6/10	3.044	2.412	0.095	0.059	0.066

based upon the small-strain approximation. In principle, a_0 and a_2 are determined by ordinate and initial curvature of the function $c_{44}(\alpha s_x)$ ($\alpha \rightarrow 0$) (see figure 4.16). The latter is extremely difficult to extract from a molecular expression given the typical accuracy with which the shear modulus can be calculated in our Monte Carlo simulations (see figure 4.16). However, an accurate estimate is possible based upon (4.6) which, together with (4.10) leads to

$$a_0 \equiv c_{44}(0) = \frac{3}{2} \frac{T_{zx}^{yd}}{\alpha^{yd} s_x} \quad (4.11)$$

and

$$a_2 \equiv \frac{1}{2} \frac{d^2 c_{44}(\alpha s_x)}{d(\alpha s_x)^2} \Big|_{\alpha=0} = -\frac{3}{2} \frac{T_{zx}^{yd}}{(\alpha^{yd} s_x)^3} \quad (4.12)$$

in terms of yield stress and strain. These latter quantities can be determined with high precision from (3.64), (3.65), (3.72), and plots similar to the ones shown in figure 4.14, figure 4.15(a), and figure 4.21(a). Validity of (4.11) is illustrated by table 4.1 where we compare it with the shear modulus obtained directly from the molecular expression (3.78) for a selection of unsheared bridge phases. Normalizing the (shear) equation of state (4.10) by using (4.8) and subsequently inserting (4.11) and (4.12) permits one to recast (4.10) as

$$\tilde{T}_{zx} = \frac{\tilde{\alpha}(3 - \tilde{\alpha}^2)}{2} \quad (4.13)$$

where up to the yield point $0 \leq \tilde{\alpha} \leq 1$ and $0 \leq \tilde{T}_{zx} \leq 1$ are dimensionless quantities so that (4.13) may be viewed as a master (stress) equation in agreement with the plot in figure 4.15(b). We emphasize that the master equation is a direct consequence of the small-strain approximation. A unique representation

of stress curves is precluded if, on the other hand, one includes higher-order terms proportional to a_{2k} ($k \geq 2$) in the expansion (4.9) because then expressions for $\alpha^{y^d} s_x$ and $T_{zx}^{y^d}$ [determined *via* (4.7), (4.10)] depend on the expansion coefficients in a complex way. Thus, contrary to Ref [86] there is no hope to obtain a unique expression like (4.13) free of any materials constants $\{a_{2k}\}$.

4.2.2 Thermodynamic stability

From a fundamental point of view, bridge phases comprising different numbers of molecular strata may be viewed as different thermodynamic phases. This interpretation is evident from (3.23) indicating that these different bridge morphologies (generally corresponding to different values of s_z and T_{yy}) will exhibit different values of the grand mixed isostress-isostrain potential Ψ [see (3.23)]. A multiplicity of morphologies exists despite the fact that the thermodynamic state is uniquely specified by the set $\{T, \mu, s_x, s_y, T_{zz}, \alpha s_x\}$ of natural variables of Ψ . However, from an equilibrium perspective only the morphology corresponding to the *global* minimum of Ψ is a thermodynamically stable phase; the others must be metastable.

Fortunately, only a small, finite number of possible morphologies can exist under the present thermodynamic constraints. This can be understood by considering the (normal) compressional stress T_{zz} (see (3.75), (3.76)) plotted as a function of substrate separation s_z in figure 4.17(a). Data plotted in figure 4.17 were obtained in Monte Carlo simulations in the grand canonical ensemble which has the advantage that the wall distance s_z belongs to the set of natural variables instead of T_{zz} . The plot in figure 4.17(a) shows that T_{zz} is a damped oscillatory function of s_z . These oscillations are fingerprints of stratification (see section 4.1.1), that is the formation of new fluid layers as the substrate separation increases at constant T and μ [79]. Damping can be ascribed to the decreasing influence of the wall potential $\Phi(x, z)$ if s_z increases. Eventually the system undergoes a phase transition to a droplet phase (see figure 4.6). Droplet phases exhibit a local density which is low but approximately uniform in the core region [see figure 4.11(c)]. This region increases with increasing s_z . Thus the local density in the core region equals more and more that of the corresponding

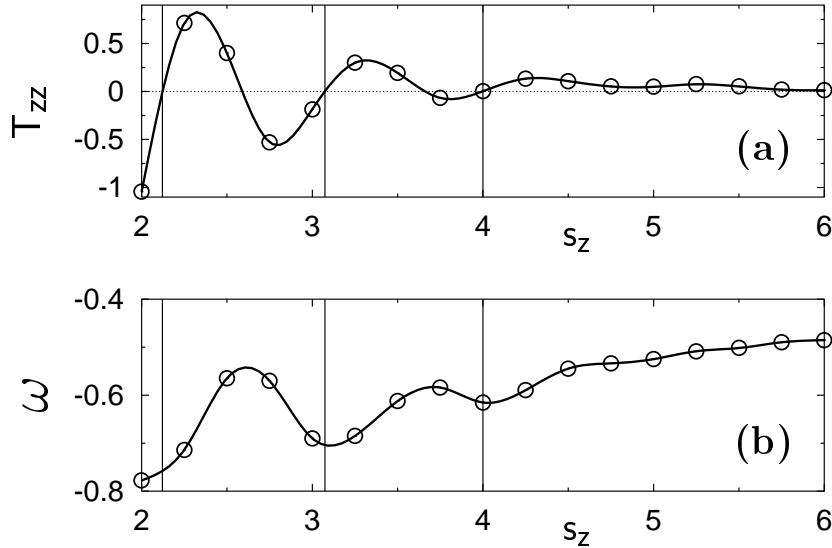


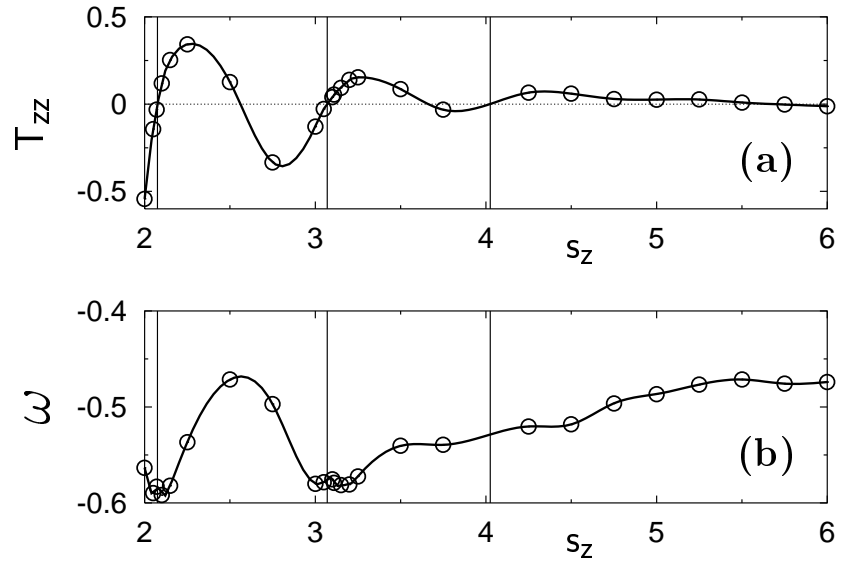
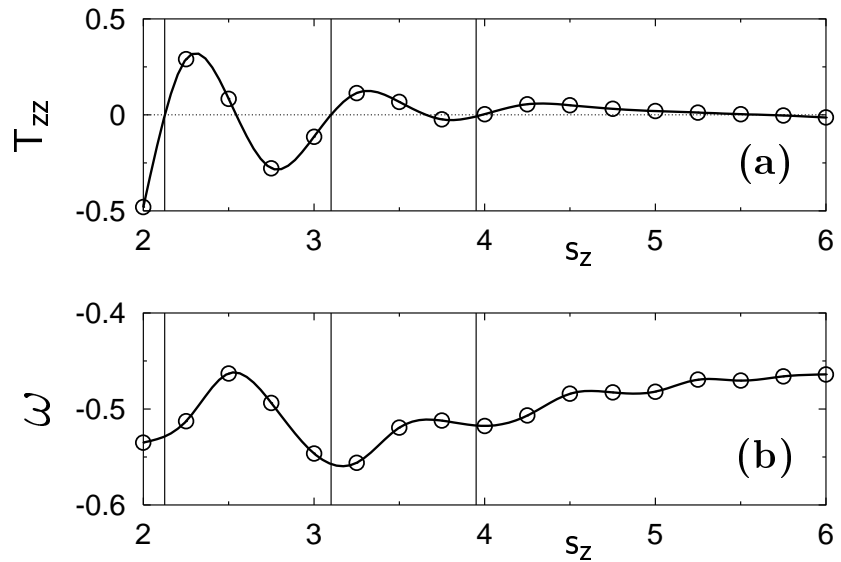
Figure 4.17: (a) Normal compressional stress T_{zz} (a) (see (3.75), (3.76)) as function of substrate separation from Monte Carlo simulations in grand canonical ensemble (o) ($\alpha_{s_x} = 0.0$). Solid lines are intended to guide the eye. (b) as (a) but for line density of the grand potential ω [see (4.16)]. Intersections between the latter and vertical lines demarcate (meta- or thermodynamically) stable states in the grand mixed stress-strain ensemble for $T_{zz} = 0.0$ (see text).

bulk phase (i.e. bulk phase at the same T and μ). As a result

$$\lim_{s_z \rightarrow \infty} T_{zz}(s_z) = -P_{\text{bulk}} \quad (4.14)$$

where $P_{\text{bulk}}(\mu, T) \simeq 0.03$ is the bulk pressure. In other words, because stratification diminishes with increasing s_z , oscillations in $T_{zz}(s_z)$ vanish eventually, too [109]. Therefore, the plot in figure 4.17(a) shows that under the present conditions and for $s_z \geq 6.0$ stratification becomes unimportant.

In the grand mixed stress-strain ensemble morphologies consistent with the set $\{T, \mu, s_x, s_y, T_{zz}, \alpha_{s_x}\}$ of state variables can now be identified with intersections between the oscillatory curve $T_{zz}(s_z)$ and the isobar $T_{zz} = \text{const} \leq 0$. However, only intersections for which $dT_{zz}/ds_z \geq 0$ correspond to (thermodynamically or meta-) stable states as pointed out in [110]; intersections for which $dT_{zz}/ds_z < 0$ pertain to mechanically unstable states which cannot be

Figure 4.18: As figure 4.17, but for $\alpha_{s_x} = 2.25$.Figure 4.19: As figure 4.17, but for $\alpha_{s_x} = 2.50$.

realized in the grand mixed stress–strain ensemble. The thermodynamically stable phase corresponds to the intersection having the smallest (areal) grand potential density (3.21)

$$\omega = \Omega/A_z = T_{yy}s_z \quad (4.15)$$

at $T_{zz} = 0$. Based upon this rationale, an inspection of figure 4.17 shows that the thermodynamically stable, unstrained morphology ($\alpha = 0.0$) is a monolayer film with $s_z \simeq 2.1$ ($T_{zz} = 0.0$). If confined films are progressively sheared a parallel analysis of plots in figure 4.18 and figure 4.19 shows that the minimum of ω for $s_z \simeq 2.1$ becomes shallower while another minimum around $s_z \simeq 3.1$, corresponding to a bilayer film, becomes deeper with increasing shear strain. Eventually the depth of the latter minimum exceeds that pertaining to the monolayer film so that a bilayer film becomes the thermodynamically stable phase. Thus, a shear strain exists such that ω is the same for mono- and bilayer films, meaning that a monolayer phase coexists with a bilayer phase.

To obtain a more concise picture of thermodynamic stability of different film morphologies we plot the (areal) grand mixed isostress-isostrain potential density (3.23)

$$\zeta = \Psi/A_z = (T_{yy} - T_{zz})s_z \quad (4.16)$$

as a function of αs_x in figure 4.20 for the same system analyzed in figures 4.17-4.19. In a sequence of Monte Carlo simulations in the grand mixed isostress-isostrain ensemble we calculate ζ directly from (4.16), ($T_{zz} = 0$) using the molecular expression for T_{yy} given in (3.73). An alternative expression for $\zeta(\alpha s_x)$ can be obtained by integrating (3.24)

$$\begin{aligned} \zeta(\alpha s_x) &= \zeta(0) + \int_0^{\alpha s_x} d(\alpha' s_x) T_{zx}(\alpha' s_x), \quad \text{fixed } T, \mu, s_x, s_y, T_{zz} \quad (4.17) \\ &\simeq \zeta(0) + \frac{a_0}{2} (\alpha s_x)^2 + \frac{a_2}{12} (\alpha s_x)^4 \end{aligned}$$

where the second line is based upon the small-strain approximation (4.10). Full lines in figure 4.20 are representations of (4.17) where the constants a_0 and a_2 were determined as in section 4.2.1. Solid lines plotted in figure 4.20(a) are therefore obtained without further adjusting a_0 and a_2 ; $\zeta(0)$ is taken from Monte Carlo simulations for unstrained bridge phases. The excellent agreement

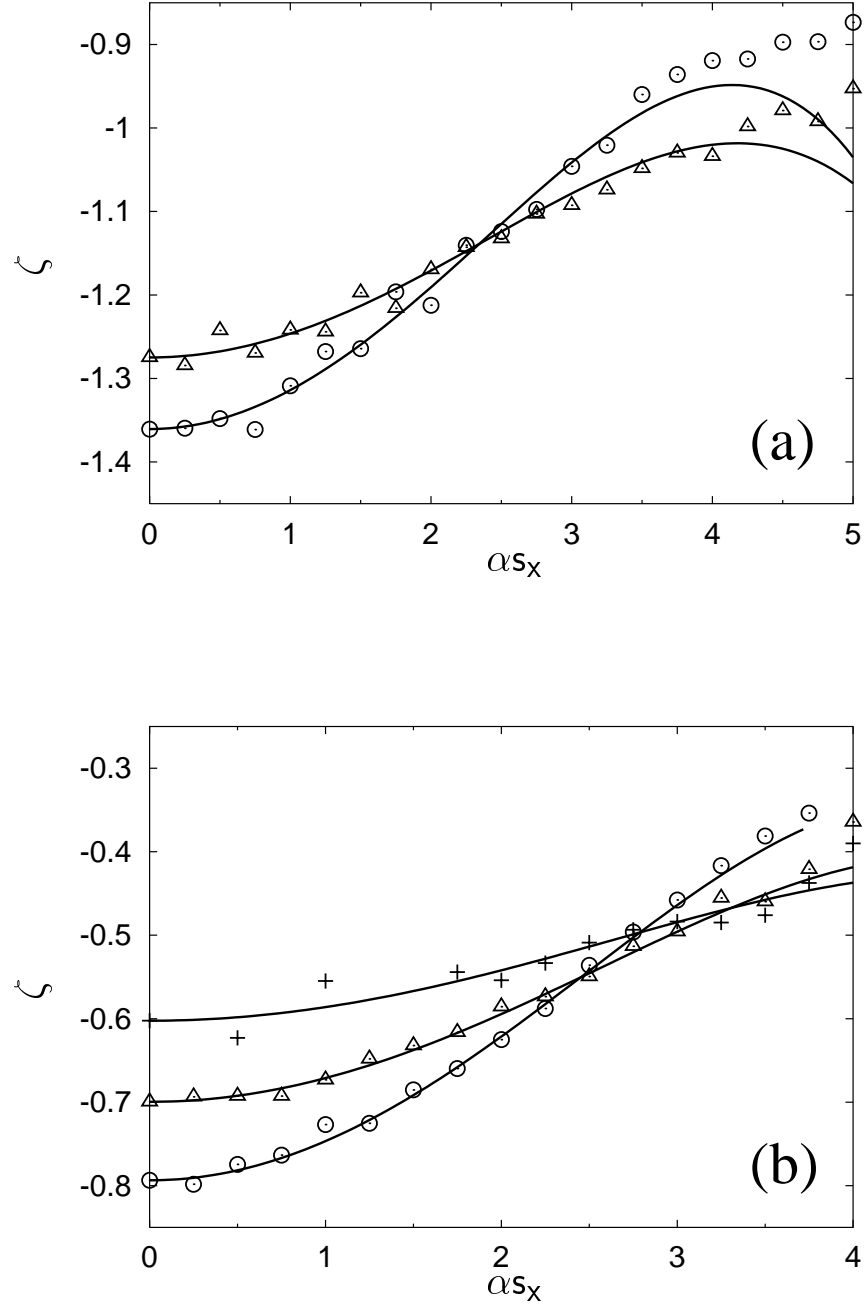


Figure 4.20: (a) Areal free-energy density ζ as function of shear strain αs_x for mono- (\circ), bi- (Δ), and trilayer (+) morphologies calculated in grand mixed stress-strain ensemble Monte Carlo simulations [see (4.16), (3.73)] for $c_r = 6/10$. Solid lines are calculated from (4.17). (b) As (a), but for $c_r = 4/10$.

between $\zeta(\alpha s_x)$ from the Monte Carlo simulations in the grand mixed stress–strain ensemble and the small–strain–approximation in (4.17) highlights once more the validity of the latter for all $\alpha \leq \alpha^{yd}$. However, the plot in figure 4.20(a) also shows that the small–strain assumption is doomed to fail for sufficiently large shear strains in accord with one’s expectation.

From the plots in figure 4.20(a) one also notices that ζ (and therefore Ψ , $A_z = \text{const}$) is lowest for a monolayer bridge phase over the range $0.0 \leq \alpha s_x \leq 2.3$ indicating that the monolayer is the thermodynamically stable phase in this regime. Figure 4.20(a) also shows that intersections $\alpha^* s_x$ exist at which Ψ for a pair of different morphologies assumes the same value. Thus, at $\alpha = \alpha^*$ these different phases coexist so that the points $\alpha = \alpha^*$ correspond to first–order phase transitions between bridge phases comprising different numbers of molecular strata. While there is no obvious relationship between α^* for the coexistence of mono– and bilayer morphologies and α^{yd} , we notice that for all the cases investigated a monolayer film is the thermodynamically stable morphology for all $\alpha \leq \alpha^{yd}$ so that up to the yield point, plots in figure 4.15 apparently pertain to thermodynamically stable phases.

Thicker films are therefore thermodynamically stable only if the shear strain exceeds the yield strain. For example, plots in figure 4.20(a) for $c_r = 6/10$ show that ζ for a bilayer bridge phase is lower than for the corresponding monolayer bridge phase over the range $2.3 \leq \alpha s_x \leq 5.0$ where the bilayer bridge phase is the thermodynamically stable phase according to the above discussion. An additional trilayer bridge phase was investigated for $c_r = 4/10$ as plots in figure 4.20(b) show. For $c_r = 4/10$ the bilayer is thermodynamically stable over the range $2.4 \leq \alpha s_x \leq 3.3$ whereas the trilayer film seems to be thermodynamically stable over the range $3.3 \leq \alpha s_x \leq 4.0$ where all three curves end. However, for the trilayer morphology the statistical error of $\zeta(\alpha s_x)$ is already quite large because T_{yy} is small (see figures 4.17–4.19). For $\alpha \simeq 4.0$ bridge phases become unstable and the system undergoes a first–order phase transition to a gas phase (see section 4.1.3).

It is furthermore noteworthy that universality of stress curves, in the sense of section 4.2.1, is not restricted to monolayer fluids. Plots of \tilde{T}_{zx} versus $\tilde{\alpha}$ in figure 4.21(b) show that simulation data for mono–, bi–, and trilayer bridge phases can

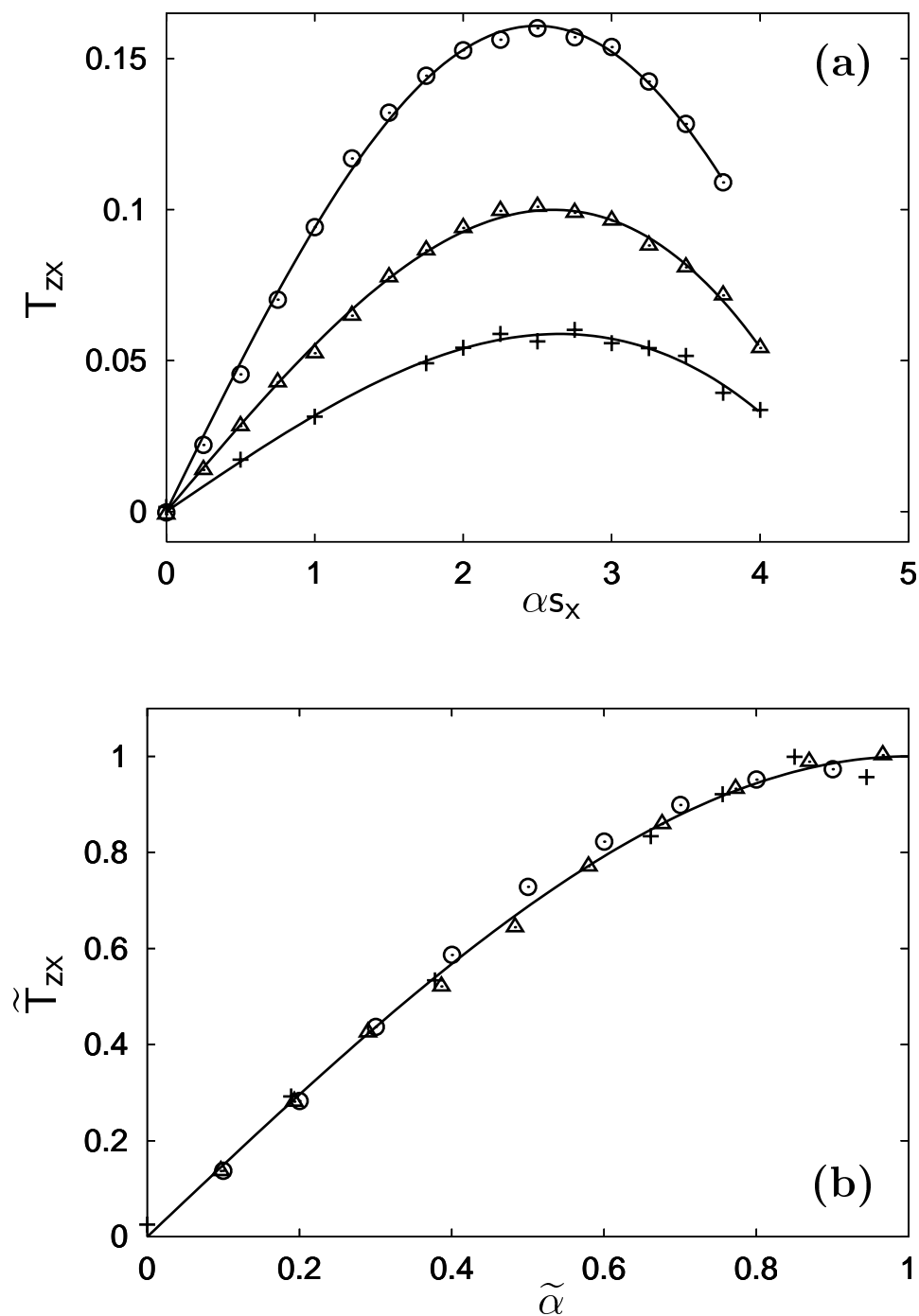


Figure 4.21: (a) As figure 4.15(a), but for mono- (\circ), bi- (Δ), and trilayer ($+$) morphologies and $c_r = 4/10$. (b) as figure 4.15(b) but for data points plotted in (a).

also be mapped onto the master curve (4.13) according to the treatment detailed in the previous section. Again, the stress curves in figure 4.21(a) end at some $\alpha^c s_x$ because the bridge phases evaporate (see section 4.1.3).

Chapter 5

Discussion and conclusions

Phase behavior and mechanical properties of simple fluids confined by chemically corrugated substrates were investigated theoretically in Monte Carlo simulations in the grand canonical and a grand mixed isostress-isostrain ensemble. These computer simulations supplement density-functional calculations of a parallel lattice model based upon a mean-field treatment of the intrinsic free energy. In general, confinement introduces a new lengthscale with profound consequences for phase behavior and materials properties of soft condensed matter (see chapter 4). In this work we are exclusively concerned with confining substrates endowed with stripes of chemically different materials. The widths of these stripes add yet another relevant lengthscale to the system. Hence, a relatively large set of parameters is needed to describe a model system with nanopatterned substrates. To investigate the effect of variations of these parameters on the phase behavior of the confined fluid requires an approach which, on one hand, is capable of representing the heterogeneity of the confining substrates and, on the other hand, permits one to obtain phase diagrams at moderate computational expense. The mean-field treatment (see section 2.3.1) of a confined lattice gas (see figure 2.1) serves this purpose in an almost ideal manner.

However, the mean-field lattice-gas model is based upon two key assumptions. First, positions of fluid molecules are restricted to sites of a simple (cubic) lattice and, second, intermolecular correlations are explicitly neglected. Based upon these two assumptions the grand potential becomes a functional of the

local density $\Omega[\boldsymbol{\rho}]$ [see (2.75)]. From a variational treatment of $\Omega[\boldsymbol{\rho}]$ one obtains a set of transcendental (Euler–Lagrange) equations [see (2.77)] which must be solved to identify thermodynamically stable phases and metastable morphologies associated with global and local minima of the grand potential, respectively.

In the limit of vanishing temperature ($T = 0$) the lattice–gas model may be treated analytically (see section 2.2.3) because the grand potential is given by the internal energy only, while entropic contributions according to the Third Law of Thermodynamics vanish. The identification of thermodynamically stable phases and transformations between them requires knowledge of *all* possible morphologies. A systematic investigation of these morphologies at $T = 0$ in the case of a *single homogeneous* surface was first presented by Pandit *et al* [11]. The chemical heterogeneity of the present substrates, on the other hand, induces a variety of new morphologies differing from those reported in Ref. [11] in both number and structure. However, a systematic classification of morphologies is still possible utilizing the modular approach detailed in section 2.2.2. The modular approach developed in this thesis enables one to identify the complete set of morphologies and subsequently to determine the full phase diagram at $T = 0$.

For higher temperatures ($T > 0$) an analytic solution of the lattice–gas model is no longer possible. Instead, the full phase diagram is obtained by solving the mean-field equations (2.77) iteratively. Since the mean–field treatment is exact in the limit of vanishing temperature (see section 2.3.3), exact solutions derived at $T = 0$ serve as suitable initial guesses for the iteration procedure. This is particularly convenient because it can be rationalized that the iteration procedure utilized here provides the *full equilibrium* phase diagram [see appendix A]. Therefore, the present approach prevents one from accidentally missing parts of the phase diagram, as in previous work where less sophisticated techniques were used [79, 64, 65, 93, 94, 95, 96].

The exact phase diagrams $\mu_x(T)$ obtained here turn out to be ramified webs of coexistence lines $\mu_x^{\alpha\beta}(T)$, that is, lines of first order phase transitions between phases α and β . The structure of the web depends distinctly on the system parameters. As these parameters vary, the web evolves, where some of the coexistence lines are (almost) independent of the variation of certain model

parameters (see figure 2.11 and figure 4.2). This is already evident from the analytic solutions in (2.53) at $T = 0$, where some of the expressions for $\mu_x^{\alpha\beta}$ are independent of certain subsets of system parameters (see section 2.2.3). Thus, the solutions at $T = 0$ are also useful to predict variations of the phase diagram due to changes of single system parameters.

Unfortunately, the two key assumptions of the mean-field lattice gas, namely discretization of space and lack of correlations are quite unrealistic as far as fluids are concerned. Moreover, the impact of both assumptions is *a priori* uncontrollable. Therefore, we attempt to verify predictions of the lattice-gas model with the aid of a more realistic continuous model in which the treatment of intermolecular correlations is exact.

Equilibrium properties of the continuous model were obtained by Monte Carlo simulations in the grand canonical ensemble, which treats the confined phase as an open system in the thermodynamic sense. The price paid for the more realistic modeling of confined fluids is a much greater demand for computer time by Monte Carlo simulations compared with the lattice model. This, in turn, limits the scope of Monte Carlo methods so that only key predictions of the lattice-gas treatment could be checked. These concern the sequence of phase transitions expected upon variations of substrate separation in section 4.1.1 where the excellent qualitative agreement between the two approaches is illustrated. Therefore, we conclude that the mean-field lattice gas model is capable of representing the phase behavior of confined fluids qualitatively correctly as far as first-order phase transitions are concerned.

Phase transitions of fluids confined by chemically decorated substrates can be divided into two groups: surface-induced and confinement-induced transitions. Surface-induced transitions controlled by a single chemically heterogeneous surfaces have been studied extensively by Dietrich and co-workers [37, 111, 112, 113]. The simplest confinement-induced phase transition is the analogue of the bulk liquid-gas transition known as “capillary condensation”. If the confining substrates are decorated with chemical patterns composed of strongly and weakly adsorbing materials, the strongly attractive parts of the substrate may induce partial condensation of the fluid whereupon a so-called bridge phase may form. Consequently, bridge phases consist of a high-density regime filling the

gap between the strongly attractive substrate parts, surrounded by low-density gas [see figure 4.3(b)]. Bridge phases are distinguished by their inhomogeneity in the direction perpendicular to the alternating chemical stripes regardless of the distances between the confining walls. The present work is largely devoted to a systematic investigation of thermodynamic and mechanical properties of bridge phases (see section 4.1) reported first by Röcken and co-workers [64, 65].

This unique local structure causes a bridge phase to sustain a nonvanishing shear strain (to which they “respond” with a nonvanishing shear stress). Application of a shear strain is possible since the substrates are inhomogeneous in one lateral direction (x), so that their misalignment in that direction (which is a measure of the applied shear strain) can be specified quantitatively. In the limit of small deformations the shear stress increases linearly with the conjugate strain (see figure 4.14). This can be interpreted as elastic deformation of the bridges, that is Hookean behavior. Negative deviations from this Hookean response at higher shear strains indicate plastic deformation. Increasing plasticity eventually causes the shear stress to reach a maximum (yield point) and to decay for strains exceeding the yield strain. Thus, shear-stress curves $T_{zx}(\alpha s_x)$ of fluid bridges exhibit a qualitatively similar shape as those obtained for confined solidlike films by Schoen *et al* [100]. However, these latter shear-stress curves differ in both lengthscale of the deformation and height of the maximum (i.e. yield stress) from the ones calculated here [see figure 5.1(a)]. For bridge phases, $T_{zx}(\alpha s_x)$ varies nonmonotonously with the degree of substrate corrugation (see figure 4.15).

In view of the Hookean behavior in the limit of small shear strains, the shear modulus c_{44} can be expanded in powers of the shear strain [see (4.9)]. This small-strain approximation eventually permits one to deduce the dependence of T_{zx} on αs_x in the vicinity of the unstrained bridge, that is for $\alpha s_x = 0$ [see (4.10)]. Within the framework of a theory of corresponding states the expressions for $T_{zx}(\alpha s_x)$ obtained from the small strain-approximation can be renormalized so that a master curve is obtained which no longer depends on any system parameters [see (4.13) and figure 4.14].

The theory of corresponding states is not limited to the present bridge phases but may also be applied to confined solidlike films as figure 5.1 clearly indicates.

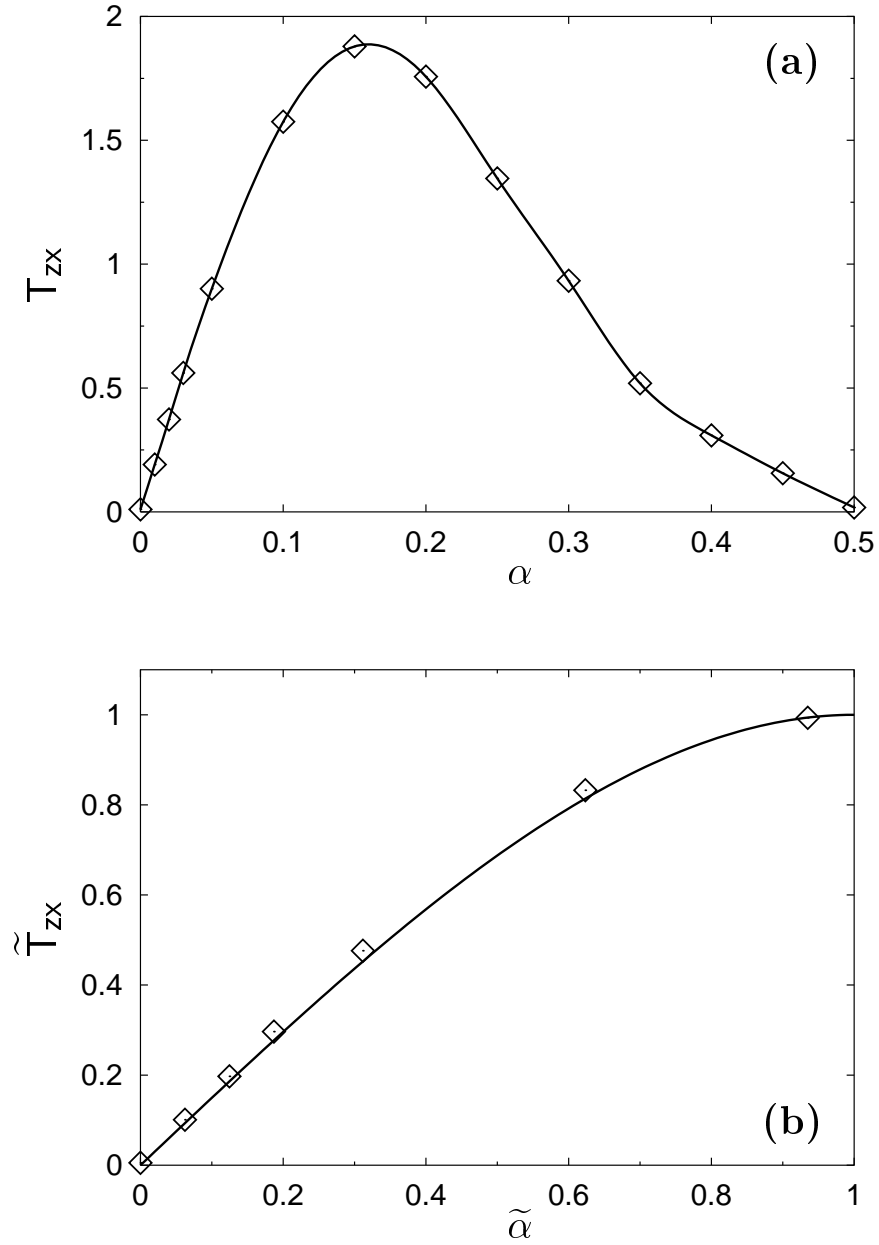


Figure 5.1: *a*) Stress curve $T_{zx}(\alpha)$ for a solidlike film forming between discrete substrates (from [100]). Solid line is a least-squares fit of a polynomial to the (discrete) Monte Carlo data points (\diamond) intended to guide the eye. *b*) Reduced stress curve $\tilde{T}_{zx}(\tilde{\alpha})$ [see (4.8)] calculated from the data plotted in (a). The solid line is a representation of the master curve (4.13)

Consequently, a confined *fluid* bridge exhibits qualitatively the same shear stress curves as a confined *solid*. In their SFA experiments (see chapter 1) Klein and Kumacheva interpreted the appearance of a nonvanishing shear stress as clear evidence for solidification of the confined film [70, 71]. In the light of the present results this is highly questionable.

This work is exclusively concerned with one-component (i.e., pure) confined phases. However, in future investigations it would be very intriguing to replace the present single-component fluid by binary (A–B) fluid mixtures. Consequently, three types of fluid–fluid interactions arise, namely A–A, B–B, and A–B between molecules of the two mixture components. In addition, there are two types of interactions between A molecules and the substrate and B molecules and the substrate, respectively (assuming the substrate to be chemically homogeneous). In other words, the phase behavior of the confined binary mixture depends on five independent types of interaction potentials rather than two as in a pure fluid. It is therefore conceivable that additional phase transitions may occur including liquid–liquid transitions. Wilding *et al* demonstrated that even a symmetric binary bulk mixture (that is, A–A and B–B interactions are identical and only the A–B interaction is different) exhibits quite a complex phase diagram [114]. In another study, Gelb *et al* recently studied a symmetric binary mixture confined to a cylindrical pore with homogeneous walls [115]. In their model none of the mixture components is preferentially adsorbed by the pore wall. They observed a demixed fluid phase consisting of alternating “plugs” of finite size that are composed predominantly of one or the other molecular species, respectively. This interesting morphology is very similar to bridge phases analyzed here in that high- and low-density regimes of the bridge are replaced by A-rich and B-rich regions (i.e., the “plugs”). However, within the framework of a mean-field lattice gas model of a confined binary mixture formation of such a plug morphology seems highly unlikely since nothing supports internal interfaces energetically as long as the wall potential is translationally invariant. Thus, the question arises whether the mean-field lattice gas is incapable of describing “plug-phases” (with finite plug size) in principle or whether these plugs may form as metastable morphologies in the simulations of Gelb *et al* [115].

So far we were concerned with a unique chemical structure of the substrate, namely alternating chemical stripes of variable width causing the symmetry to be broken in directions *normal* to the walls and *perpendicular* to the stripes. Thus, system properties are translationally invariant only in the direction *parallel* to the stripes, that is, the fluid is homogeneous in that direction. Therefore, in the continuous model a Gibbs–Duhem equation exists, offering the possibility to calculate thermodynamic potentials directly from ensemble averages of “mechanical” properties [see (3.23) and (3.21)]. However, this “mechanical” approach cannot be extended to substrates coated with chemically patterns such that properties of the confined fluid are not translationally invariant in *any* direction. An example of such a substrate structure was recently employed by Lenz *et al* [40] who studied the wetting of a single surface endowed with ring-shaped surface domains of macroscopic extent. The lack of a closed analytic expression for Ω in terms of stresses and strains is a nontrivial obstacle if one wishes to investigate the phase behavior of fluids interacting with such a low-symmetry substrate in the spirit of section 3.2 of this work. The problem may, however, be overcome by thermodynamic integration [75]. The main difficulty then is that the integration path must not intersect with any coexistence line. This, however, is problematic again since it requires knowledge of the *a priori* unknown phase diagram. Depending on the details of the system in question the latter may be rather complex as we have shown above. Applying the lattice–gas model to substrates decorated with circular domains is also nontrivial since these domains can be represented only very roughly by a sensible lattice structure.

Nevertheless, substrates endowed with circular chemical pattern seem quite intriguing. In the spirit of the work of Lenz *et al* [40] one may envision circular patterns consisting of alternating rings of weakly and strongly adsorbing solid. If a fluid is confined by such decorated substrates partial condensation triggered by the rings may occur in very much the same way in which bridges arise in this study. However, in the former system this phase transition may also be controlled by the curvature of the circular pattern with which the substrate is decorated.

Appendix A

Jacobi–Newton iteration

The numerical procedure used to determine phase diagrams of the confined lattice gas (see figure 2.1) is presented schematically in figure A.1. We begin with the analytic phase diagram at vanishing temperature ($T = 0$) (see section 2.2). For $T > 0$ the phase diagram is obtained by computing grand potential curves $\Omega^\alpha(\mu)$ (of morphologies α) to identify thermodynamically stable phases and phase coexistence [see section 2.4]. Since it is *a priori* unknown which morphologies will become coexisting phases at the actual temperature $T_k > 0$, we assume these to be the same as for the preceding temperature T_{k-1} (see figure A.1). This is possible since for the initial temperature $T_0 = 0$ the exact phase diagram is available.

However, one may accidentally miss triple points where a new coexisting phase arises. In principle, this problem cannot be avoided *a priori* but can be circumvented *a posteriori* because the triple point can be determined accurately as detailed below. To compute grand potential curves $\Omega^\alpha(\mu)$ for morphologies α at a given temperature T_k , equilibrium densities $\rho^\alpha = \{\rho_i^\alpha\}$ (which depend on μ) must be determined [see (2.75)].

For a particular morphology α (henceforth, we drop the superscript α to simplify notation) given T_k and μ this can be done by solving the variational expression [see (2.77)] using the Jacobi–Newton iteration technique [116] proceeding in alternating sequences of “local” and “global” minimization steps. For

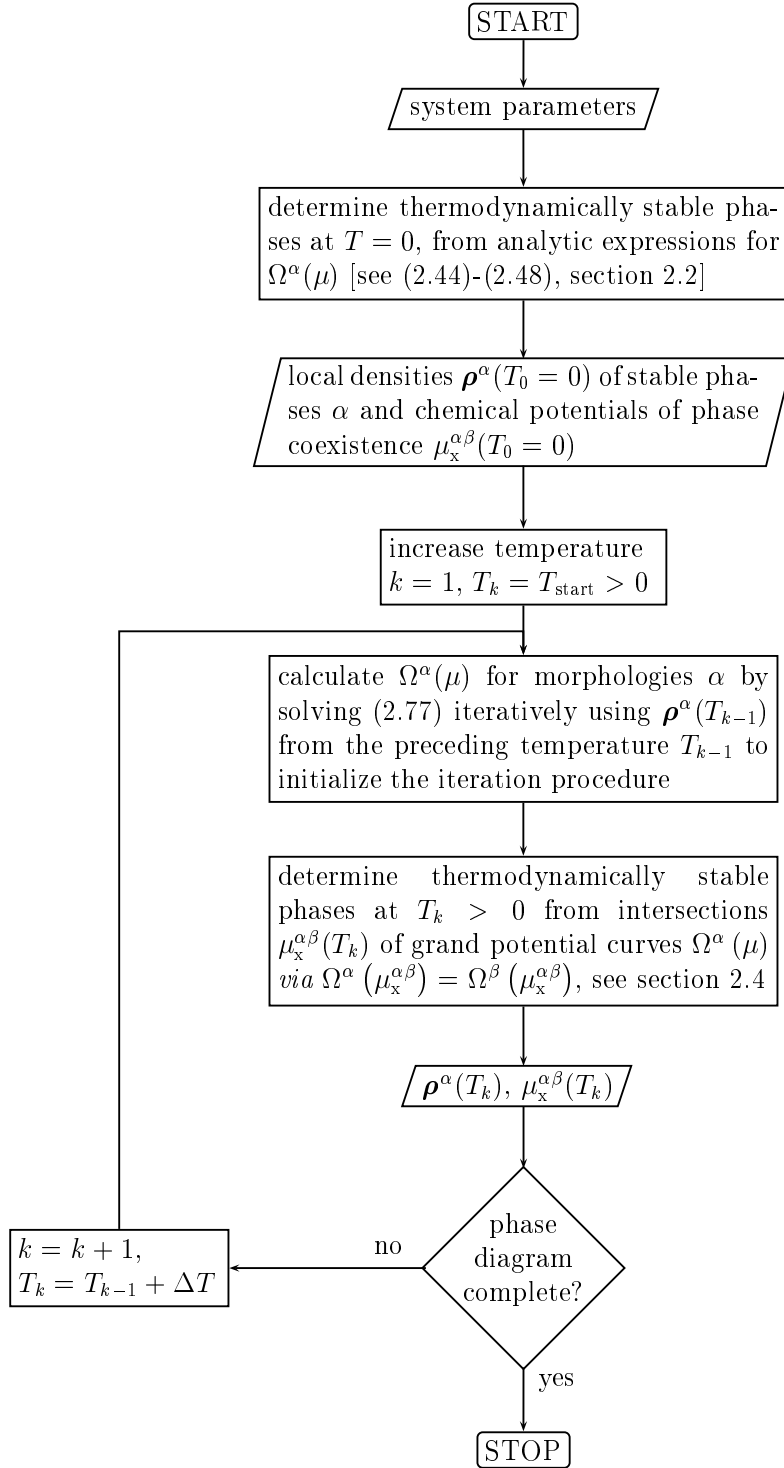


Figure A.1: Scheme of the iterative technique used to calculate phase diagrams of the confined lattice gas.

a particular site i one can rewrite (2.77) using (2.106)

$$T \ln \frac{\rho_i}{1 - \rho_i} - 2\rho_i - \eta_i = 0 \quad (\text{A.1})$$

where $\eta_i = \eta_i(\mu, \Phi_i, \rho_j)$ is a function of the chemical potential μ , the external potential at lattice site i , Φ_i , the number of nearest neighbors in the x - z -plane, and their associated local densities $\rho_j = \{\rho_j^g\}$, where ρ_i^g is the local density at lattice site i in the l -th local and g -th global minimization step. An estimate of the density ρ_{l+1}^g is obtained via

$$\rho_{l+1}^g = \rho_l^g - \frac{f(\rho_l^g)}{f'(\rho_l^g)}, \quad i = 0, 1, 2, \dots \quad (\text{A.2})$$

where from (A.1)

$$f(\rho_l^g) = T \ln \frac{\rho_l^g}{1 - \rho_l^g} - 2\rho_l^g - \eta_i(\mu, \Phi_i, \rho_j^g) \quad (\text{A.3})$$

and

$$f'(\rho_l^g) = \left[\frac{df(\rho_i)}{d\rho_i} \right]_{\rho_i^g} = \frac{T}{\rho_i^g(1 - \rho_i^g)} \quad (\text{A.4})$$

It is important to realize that throughout each local minimization cycle $\boldsymbol{\eta} = \{\eta_i\}$ is maintained at its initial value assigned at the beginning of that particular cycle. The iterative solution of (A.2) is halted if $\max_i |\rho_i^g - \rho_{i-1}^g| \leq 10^{-7}$. Local minimization is performed by visiting each lattice site consecutively; the local cycle ends once all sites have been considered.

Global minimization then involves updating the local density of the *entire* lattice according to $\rho_{0}^{g+1} = \rho_{l^*}^g$ thus providing new initial values for the next *local* minimization cycle [see (A.2) and figure A.1]. Global minimization is carried out until $\max_i |\rho_i^{g+1} - \rho_i^g| \leq 10^{-7}$.

After determining phase coexistence and identifying thermodynamically stable phases at temperature T_k , one proceeds by increasing temperature $T_{k+1} = T_k + \Delta T$ and returning to step 5 of the scheme figure A.1).

There are some technicalities of the technique presented above worth mentioning:

- Inspecting (A.4) and (A.3) one realizes, that in the two limiting cases $\rho_i = 0$ or $\rho_i = 1$ the second term in (A.2) is zero. Therefore the iteration fails if it is initialized using either $\rho_i = 0$ or 1. Instead, values like 0.0001 or 0.9999 should be employed in practice.

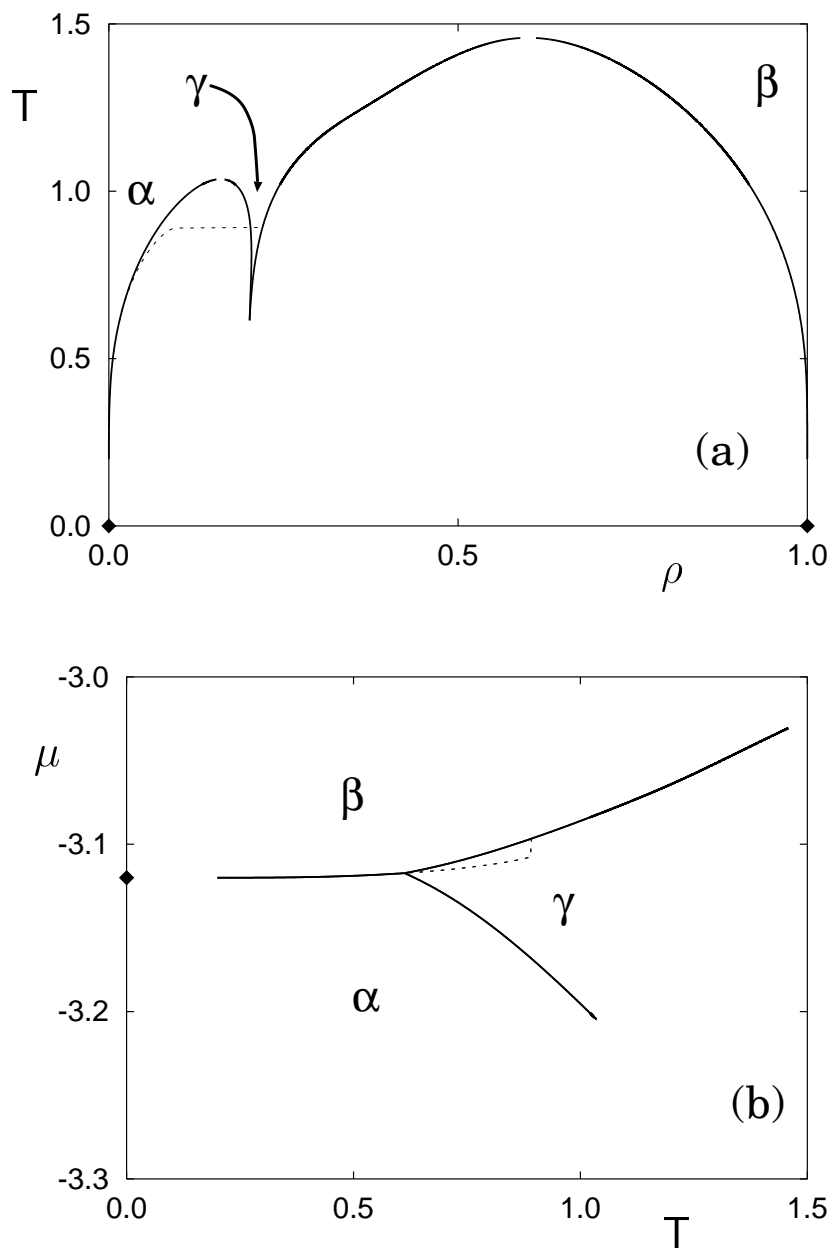


Figure A.2: Phase diagram of a mean-field lattice gas confined by homogeneous walls ($n_x = 10$, $e_{\text{wall}} = 1.1$). Full lines represent the phase diagram $\mu_x(T)$, dotted lines indicate the first accidental calculation path. (a) T - ρ representation (b) μ - T representation

- If f in (A.3) has a zero at ${}^g_i\rho_i$ this zero is usually close to an extremum of f . Both zero and extremum get closer the lower the temperature is. Therefore, at low temperatures initial densities are required which are very close to the sought (equilibrium) solutions. For that reason Newton's method usually fails at low temperatures ($T \lesssim 0.4$). A possibility to tackle this problem is to introduce a damping coefficient c ($0 < c \leq 1$) such that (A.2) is replaced by

$${}^g_{i+1}\rho_i = {}^g_i\rho_i - c \frac{f({}^g_i\rho_i)}{f'({}^g_i\rho_i)}, \quad i = 0, 1, 2, \dots \quad (\text{A.5})$$

However, in practice the accessible (low) temperature region remains limited on account of the sensitivity of initialization (usually $T \gtrsim 0.25$).

- Very low temperatures ($T < 0.1$) can be reached by starting at a sufficiently high temperature ($T \gtrsim 0.4$) where Newton's method succeeds and which is still low enough to employ the analytical ($T = 0$) solutions to initialize the iterative procedure. The calculation then proceeds as above (see figure A.1) but *decreasing* T in a stepwise fashion.
- The most substantial problem is the appearance of one or more triple points in the phase diagram. At a triple point $(T_{\text{tr}}^{\alpha\gamma\beta}, \mu_{\text{tr}}^{\alpha\gamma\beta})$ a coexistence line $\mu_x^{\alpha\beta}(T)$ bifurcates into two branches $\mu_x^{\alpha\gamma}(T)$ and $\mu_x^{\gamma\beta}(T)$, because a new phase γ becomes thermodynamically stable. The difficulty is that *a priori* one does not know where the triple point will appear and what the structure of the new phase is. Thus, one may accidentally miss the new phase altogether. Suppose, for instance, the phase diagram shown in figure A.2 is calculated. Below the triple point temperature $T_{\text{tr}}^{\alpha\gamma\beta}$ we proceed as detailed above. If the calculation is continued without care one may stay on the branch $\mu^{\alpha\beta}(T)$ which is now metastable [see figure A.2(b)]. However, the metastable path $\mu^{\alpha\beta}(T)$ ends at the critical temperature $T_c^{\alpha\gamma}$ since $\Omega^\alpha(\mu, T)$ vanishes at this temperature. Thus, for $T \gtrsim T_c^{\alpha\gamma}$ the solution "jumps" to the one belonging to coexistence line $\mu_x^{\gamma\beta}(T)$ [see figure A.2(b)]. Now this artificial "jump" enables us to determine the triple point $(T_{\text{tr}}^{\alpha\gamma\beta}, \mu_{\text{tr}}^{\alpha\gamma\beta})$, since it is clear now that such a triple point exists and what the new phase γ is. To do so one needs to go back to a temperature below the triple point $T \leq T_{\text{tr}}^{\alpha\gamma\beta}$, which is, of course

still unknown. To locate $T_{tr}^{\alpha\gamma\beta}$ one has to go back to successively lower temperatures until $\Omega^\gamma(\mu_x^{\alpha\beta}) = \Omega^\alpha(\mu_x^{\alpha\beta}) \equiv \Omega^\beta(\mu_x^{\alpha\beta})$. This procedure permits us to eventually calculate the *complete* phase diagram.

- In practice, the critical point cannot be reached. This is because the respective minima of the grand potential representing the two coexisting phases are very close. Therefore they are hardly distinguishable causing the iteration technique to fail numerically. Therefore, all phase diagrams in the T - ρ representation are not closed in the vicinity of the critical point.

Appendix B

Fluid–substrate forces in the continuous model

This appendix provides explicit expressions for the components $f_x^{[k]}(x_i, z_i)$ and $f_z^{[k]}(x_i, z_i)$ of the force exerted by the substrates on a film molecule i located at a point (x_i, z_i) (see [79]). The z -component of that force is defined by

$$f_z^{[k]}(x_i, z_i) := -\frac{\partial \Phi^{[k]}(x_i, z_i)}{\partial z} \quad (\text{B.1})$$

where $\Phi^{[k]}(x_i, z_i)$ is the mean-field representation of the external potential [see (3.10)]. From (B.1) one obtains after lengthy but straightforward algebra (see [79])

$$\begin{aligned} f_z^{[k]}(x_i, z_i) &= \frac{3\pi}{2} n_A \sigma^2 \sum_{m=-\infty}^{\infty} \sum_{m'=0}^{\infty} \quad (\text{B.2}) \\ &\quad \times (\epsilon_{\text{fw}} - \epsilon_{\text{fs}}) \{ \Theta[x''_{\text{u}}(x, d_{\text{s}}), z''] - \Theta[x''_1(x, d_{\text{s}}), z''] \} \\ &\quad + \epsilon_{\text{fw}} \{ \Theta[x''_{\text{u}}(x, s_{\text{x}}), z''] - \Theta[x''_1(x, s_{\text{x}}), z''] \} \end{aligned}$$

where x''_{u} and x''_1 are defined by (3.11) and (3.12), respectively,

$$\Theta(x'', z'') := \frac{21}{32} K_3(x'', z'') - K_4(x'', z'') \quad (\text{B.3})$$

$$\begin{aligned} K_3(x'', z'') &:= -\frac{2}{9} \frac{x'' \sigma^{11}}{(z'')^3 \sqrt{R^9}} \left[1 + \frac{8}{7} S + \frac{48}{35} S^2 + \frac{64}{35} S^3 + \frac{128}{35} S^4 \right] \quad (\text{B.4}) \\ &\quad - \frac{x'' \sigma^{11}}{z'' \sqrt{R^{11}}} \left[1 + \frac{8}{7} S + \frac{48}{35} S^2 + \frac{64}{35} S^3 + \frac{128}{35} S^4 \right] \\ &\quad - \frac{2}{9} \frac{(x'')^3 \sigma^{11}}{(z'')^5 \sqrt{R^9}} \left[\frac{8}{7} + \frac{96}{35} S + \frac{192}{35} S^2 + \frac{512}{35} S^3 \right] \end{aligned}$$

and

$$K_4(x'', z'') := - \left[\frac{2}{3} \frac{x'' \sigma^5}{(z'')^3 \sqrt{R^3}} + \frac{x'' \sigma^5}{z'' \sqrt{R^5}} \right] (1 + 2S) \quad (\text{B.5})$$

$$- \frac{4}{3} \frac{(x'')^3 \sigma^5}{(z'')^5 \sqrt{R^3}} .$$

The quantities R and S are defined by (3.7) and (3.8), respectively.

Similarly, one obtains

$$f_x^{[k]}(x_i, z_i) := - \frac{\partial \Phi^{[k]}(x_i, z_i)}{\partial x} \quad (\text{B.6})$$

$$= \frac{3\pi}{2} n_A \sigma^2 \sum_{m=-\infty}^{\infty} \sum_{m'=0}^{\infty}$$

$$\times (\epsilon_{\text{fw}} - \epsilon_{\text{fs}}) \{ \theta[x''_{\text{u}}(x, d_s), z''] - \theta[x''_1(x, d_s), z''] \}$$

$$+ \epsilon_{\text{fw}} \{ \theta[x''_{\text{u}}(x, s_x), z''] - \theta[x''_1(x, s_x), z''] \}$$

where

$$\theta(x'', z'') = I_1(x'', z'') - I_2(x'', z'') \quad (\text{B.7})$$

$$I_1(x'', z'') := \frac{21}{32} \sqrt{\left(\frac{\sigma^2}{R}\right)^{11}} \quad (\text{B.8})$$

and

$$I_2(x'', z'') := \sqrt{\left(\frac{\sigma^2}{R}\right)^5} . \quad (\text{B.9})$$

Because I_1 and I_2 are even functions of x'' [see also (3.7)], θ is an even function of x'' as well. For the special case $\alpha s_x = 0$, that is absence of a shear strain, one easily obtains [see (3.11) and (3.12)]

$$-x''_{\text{u}}(x, d) = x''_1(-x, d), \quad \text{and} \quad -x''_1(x, d) = x''_{\text{u}}(-x, d) \quad (\text{B.10})$$

since the transformation $m \rightarrow -m$ is inconsequential for the summations in (B.6)

$$\sum_{m=-\infty}^{\infty} \equiv \sum_{-m=-\infty}^{\infty} . \quad (\text{B.11})$$

Thus,

$$\theta[x''_{\text{u}}(-x, d), z''] - \theta[x''_1(-x, d), z''] \quad (\text{B.12})$$

$$= \theta[-x''_1(x, d), z''] - \theta[-x''_{\text{u}}(x, d), z'']$$

$$= - \left\{ \theta[x''_{\text{u}}(x, d), z''] - \theta[x''_1(x, d), z''] \right\}$$

and therefore $f_x^{[k]}$ is an odd function of x (provided $\alpha_{s_x} = 0$).

Appendix C

Implementation of the fluid–substrate potential

From an inspection of (3.10) it is immediately clear that the fluid-wall potential $\Phi^{[k]}$ cannot be computed directly, since infinite summation is numerically impossible. However, following Schoen et al. [79] it turns out that in practice a sufficiently accurate numerical representation of $\Phi^{[k]}$ is obtained by replacing the double sum in (3.10) according to

$$\sum_{m=-\infty}^{\infty} \sum_{m'=0}^{\infty} \longrightarrow \sum_{m=-2}^2 \sum_{m'=0}^{50} . \quad (\text{C.1})$$

As shown in the same reference it is too time consuming to calculate the fluid-wall interaction in every simulation step, even in the case of truncated summations (C.1). Instead of computing $\Phi^{[k]}$ during each simulation step, the truncated version of $\Phi^{[k]}$ is calculated prior to the simulation on a fine grid x_h, z_k spanning the entire simulation cell. The potential at an arbitrary point in the x – z –plane ($\Phi^{[k]}$ is translationally invariant in y –direction) is then calculated by bilinear interpolation [117].

The computational effort can be reduced further by regarding the symmetry of $\Phi^{[k]}$ [see (3.10)]. From their definitions [see (3.5), (3.6)] one identifies I_3 and I_4 to be odd functions of x'' (3.3) and therefore, Δ [see (3.9)] to be an odd

function of x'' likewise. Thus,

$$\begin{aligned}
& \Delta\left(x + \frac{1}{2}d, z''\right) - \Delta\left(x - \frac{1}{2}d, z''\right) \\
= & -\Delta\left(-x - \frac{1}{2}d, z''\right) + \Delta\left(-x + \frac{1}{2}d, z''\right) \\
= & \Delta\left(-x + \frac{1}{2}d, z''\right) - \Delta\left(-x - \frac{1}{2}d, z''\right)
\end{aligned} \tag{C.2}$$

where the second equality reveals that $\Phi^{[1]}$ is an even function of x . Therefore it is sufficient to calculate $\Phi^{[1]}$ in the region $0 \leq x \leq s_x/2$ and to apply the transformation

$$[1]: \quad x \longrightarrow \tilde{x} = |x| : \quad \Phi^{[1]}(x, z) = \Phi^{[1]}(\tilde{x}, z) . \tag{C.3}$$

Since the upper wall “2” is identical with the lower wall “1” except the spatial position, $\Phi^{[2]}$ is an even function of $(x - \alpha s_x)$. Thus, the interaction contribution from the upper wall can be obtained by introducing a transformation similar to (C.3)

$$[2]: \quad \left\{ \begin{array}{l} x \longrightarrow \tilde{x} = |x - \alpha s_x| \\ z \longrightarrow -z \end{array} \right\} \quad \Phi^{[2]}(x, z) = \Phi^{[1]}(\tilde{x}, -z) . \tag{C.4}$$

Bibliography

- [1] F. Kohler, *The Liquid State*, Verlag Chemie, Weinheim, (1972).
- [2] W. Nolting, *Grundkurs: Theoretische Physik 6. Statistische Physik*, Verlag Zimmermann-Neufang, Ulmen, 2nd ed., (1994).
- [3] D.J. Van der Waals, *Over de Continuïteit van der Gas- en Vloeistoestand*, PhD thesis, Leiden, (1873).
- [4] J.S. Rowlinson, *Studies in Statistical Mechanics*, North-Holland, Amsterdam, (1988).
- [5] P.A. Monson and D.A. Kofke, *Adv. Chem. Phys.* **115**, 113 (2000).
- [6] J.W. Cahn, *J. Chem. Phys.* **66**, 3667 (1977).
- [7] C. Ebner and W.F. Saam, *Phys. Rev. Lett.* **38**, 1486 (1977).
- [8] W.F. Saam and C. Ebner, *Phys. Rev. A* **17**, 1768 (1978).
- [9] Y. Fan and P.A. Monson, *J. Chem. Phys.* **99**, 6897 (1993).
- [10] M. Schick, *Liquids at Interfaces, Proceedings of the Les Houches Summer School Lectures and Session XLVIII* ed J. Charvolin, J.F. Joanny and J. Zinn-Justin, p. 415–496. Elsevier Science, Amsterdam, (1990).
- [11] R. Pandit, M. Schick, and M. Wortis, *Phys. Rev. E* **26**, 5112 (1982).
- [12] B.S. Hong, J.H. Hang, S.T. Kim, Y.J. Cho, and M.S. Park, *Thin Solid Films* **351**, 274 (1999).
- [13] W. Barthlott and C. Neinhuis, *Planta* **202**, 1 (1996).

- [14] D. Beysens, *Liquids at Interfaces, Proceedings of the Les Houches Summer School Lectures and Session XLVIII* ed J. Charvolin, J.F. Joanny and J. Zinn-Justin, p. 499–548. Elsevier Science, Amsterdam, (1990).
- [15] E.M. Blokhuis and B. Widom, *Corr. Opin. Colloid Interface Sci.* **1**, 424 (1996).
- [16] G.H. Findenegg and S. Herminghaus, *Curr. Opin. Colloid Interface Sci.* **2**, 301 (1997).
- [17] D.W.L. Tolfree, *Rep. Prog. Phys.* **61**, 313 (1998).
- [18] F. Burmeister, C. Schäfle, B. Keilhofer, C. Bechinger, J. Boneberg, and P. Leiderer, *Adv. Mater.* **10**, 495 (1998).
- [19] J. Boneberg, F. Burmeister, C. Schäfle, P. Leiderer, D. Reim, A. Fery, and S. Herminghaus, *Langmuir* **13**, 7080 (1997).
- [20] K. Kern, H. Niehus, A. Schatz, P. Zeppenfeld, J. Goerge, and G. Cosma, *Phys. Rev. Lett.* **67**, 855 (1991).
- [21] P. Zeppenfeld, V. Diercks, C. Tölkes, R. David, and M.A. Krzyowski, *Appl. Surf. Sci.* **130-132**, 484 (1998).
- [22] P. Zeppenfeld and M. Hohage, *Phys. Bl.* **56**, 33 (2000).
- [23] P. Avouris, *Acc. Chem. Res.* **28**, 95 (1995).
- [24] G. Meyer and K.-H. Rieder, *Physik in unserer Zeit* **31**, 8 (2000).
- [25] A. Kumar and G. Whitesides, *Appl. Phys. Lett.* **63**, 2002 (1993).
- [26] J. Drelich, J.D. Miller, A. Kumar, and G.M. Whitesides, *Colloids and Surfaces* **93**, 1 (1994).
- [27] A. Kumar, H.A. Biebuyck, and G.M. Whitesides, *Langmuir* **10**, 1498 (1994).
- [28] P.C. Hidber, W. Helbig, E. Kim, and G.M. Whitesides, *Langmuir* **12**, 1375 (1996).

- [29] T. Pompe, A. Fery, S. Herminghaus, A. Kriele, H. Lorenz, and J.P. Kottaus, *Langmuir* **15**, 2398 (1999).
- [30] R.J. Jackman, J.L. Wilbur, and G.M. Whitesides, *Science* **269**, 664 (1995).
- [31] M. Schoen and S. Dietrich, *Phys. Rev. E* **56**, 499 (1997).
- [32] S. Dietrich, *New approaches to problems in liquid state theory* ed C. Caccamo, J.-P. Hansen and G. Stell, p. 197–244. Kluwer Academic Publishers, Dordrecht, (1999).
- [33] K. Reimer, S. Dietrich, and M. Napirowski, *Phys. Rev. E* **60**, 4027 (1999).
- [34] A.O. Parry, A.J. Wood, and C. Rascón, *J. Phys.: Condens. Matter* **13**, 4591 (2000).
- [35] H. Gau, S. Herminghaus, P. Lenz, and R. Lipowsky, *Science* **283**, 46 (1990).
- [36] P. Lenz and R. Lipowsky, Morphological transitions of wetting layers on structured surfaces. *Phys. Rev. Lett.* **80**, 1920 (1998).
- [37] C. Bauer and S. Dietrich, *Phys. Rev. E* **61**, 1664 (2000).
- [38] C. Bauer, *Benetzung chemisch strukturierter Substrate*. PhD thesis, Bergische Universität Gesamthochschule Wuppertal, (1999).
- [39] P. Lenz and R. Lipowsky, *Eur. Phys. J. E* **1**, 249 (2000).
- [40] P. Lenz, W. Fenzel, and R. Lipowsky, *Europhys. Lett.* **53**, 618 (2001).
- [41] R. Lipowsky, *Curr. Opin. Colloid Interface Sci.* **6**, 40 (2001).
- [42] S. Herminghaus, A. Fery, and D. Reim, *Ultramicroscopy* **69**, 211 (1997).
- [43] T. Pompe, A. Fery, and S. Herminghaus, *Langmuir* **14**, 2586 (1998).
- [44] A. Fery, T. Pompe, and S. Herminghaus, *J. Adhesion Sci. Technol.* **13**, 1071 (1999).
- [45] S. Herminghaus, T. Pompe, and A. Fery, *J. Adhesion Sci. Technol.* **14**, 1767 (2000).

- [46] M. Grunze, *Science* **283**, 41 (1999).
- [47] H. Becker and C. Gärtner, *Phys. Bl.* **55**, 51 (1999).
- [48] H. Shi, W.-B. Tsai, M.D. Garrison, S. Ferrari, and B.D. Ratner, *Nature* **398**, 593 (1999).
- [49] M.A. Bruns, B.N. Johnson, S.N. Brahmaandra, K. Handipue, J.R. Webster M. Krishnan, T.S. Sammarco, P.M. Man, D. Jons, D. Heldsinger, C.H. Mastrangelo, and D.T. Burke, *Science* **282**, 484 (1998).
- [50] R.F. Service, *Science* **282**, 399 (1998).
- [51] J. Fang and C.M. Knobler, *Langmuir* **12**, 1368 (1996).
- [52] R. Wang, K. Hashimoto, A. Fujishima, M. Chikuni, E. Kojima, A. Kitamura, M. Shimohigoshi, and T. Watanabe, *Nature* **388**, 431 (1997).
- [53] G. Möller, M. Harke, H. Motschmann, and D. Perscher, *Langmuir* **14**, 4956 (1998).
- [54] R. Evans, *J. Phys.: Condens. Matter* **2**, 8989 (1990).
- [55] M. Thommes and G.H. Findenegg, *Langmuir* **10**, 4270 (1994).
- [56] S. Groß, *Untersuchungen zur Porenkondensation und zum Zustandsverhalten reiner Fluide in mesoporösen SiO₂-Materialien*. PhD thesis, Technische Universität Berlin, (1997).
- [57] C.G.V. Burgess, D.H. Everett, and S. Nuttall *Pure Appl. Chem.* **61**, 1845 (1989).
- [58] M.L. Rosinberg. *New approaches to old and new problems in liquid state theory* ed C. Caccamo, J.-P. Hansen and G. Stell, p. 245-271 Kluwer Academic Publishers, Dordrecht, (1999).
- [59] E. Kierlik, M.L. Rosinberg, G. Tarjus, and E. Pitard, *Mol. Phys.* **95**, 341 (1998).
- [60] E. Kierlik, M.L. Rosinberg, G. Tarjus, and P.A. Monson, *Fundamentals of Adsorption*, vol. 6, p. 867-872. Elsevier, Paris, (1998).

- [61] E. Kierlik, M.L. Rosinberg, G. Tarjus, and E. Viot, *Phys. Chem. Chem. Phys.* **3**, 1201 (2001).
- [62] K.S. Page and P.A. Monson, *Phys. Rev. E* **54**, R29 (1996).
- [63] K.S. Page and P.A. Monson, *Phys. Rev. E* **54**, 6557 (1996).
- [64] P. Roecken and P. Tarazona, *J. Chem. Phys.* **105**, 2034 (1996).
- [65] P. Roecken, A. Somoza, P. Tarazona, and G.H. Findenegg, *J. Chem. Phys.* **108**, 8689 (1998).
- [66] C. Chmiel, K. Karykowski, A. Patrykiewicz, W. Rzyśko, and S. Sokołowski, *Mol. Phys.* **81**, 691 (1994).
- [67] M. Schoen, *Colloids and Surfaces A: Physicochem. eng. ASP*, in press.
- [68] L.D. Gelb, K.E. Gubbins, R. Radhakrishnan, and M. Sliwinski-Bartkowiak, *Rep. Prog. Phys.* **62**, 1573 (1999).
- [69] J. Israelachvili, *Intermolecular & Surface Forces*, Academic Press, London, 2nd ed., (1991).
- [70] J. Klein and E. Kumacheva, *J. Chem. Phys.* **108**, 6996 (1998).
- [71] E. Kumacheva and J. Klein, *J. Chem. Phys.* **108**, 7010 (1998).
- [72] M. Schoen, *Computational Methods in Surface and Colloid Science*, p. 1–75. Marcel Dekker and Inc., New York Basel, (2000).
- [73] P. Harrowell, *Supramolecular Structures in Confined Geometries* ed G. Warr and S. Manne, Oxford University Press, Oxford, (1999).
- [74] R.J. Baxter, *Exactly Solved Models in Statistical Mechanics*, Academic Press, London, (1982).
- [75] K. Binder, *Z. Phys. B – Condensed Matter* **45**, 61 (1981).
- [76] H.B. Callen, *Thermodynamics and an introduction to thermostatistics*, John Wiley & Sons and Inc., New York, 2nd ed., (1985).
- [77] R. Evans, *Adv. Phys.* **28**, 143 (1979).

- [78] F. Schwabel, *Statistische Mechanik*, Springer, Berlin, (2000).
- [79] M. Schoen and D.J. Diestler, *Phys. Rev. E* **56**, 4427 (1997).
- [80] H.B. Callen, *Thermodynamics*, John Wiley & Sons and Inc., New York, (1960).
- [81] G. Arfken, *Mathematical Methods for Physicists*, Academic Press, London, 3rd ed., (1985).
- [82] D.A. McQuarrie, *Statistical Mechanics*, Harper & Row, New York, (1976).
- [83] T.L. Hill, *Statistical Mechanics*, Mineola, Dover, (1987).
- [84] R.H. Fowler, *Statistical Mechanics*, Cambridge University Press, Cambridge, (1966).
- [85] M. Schoen, *Physica A* **240**, 328 (1997).
- [86] P. Bordarier, M. Schoen, and A.H. Fuchs, *Phys. Rev. E* **57**, 1621 (1998).
- [87] M.P. Allen and D.J. Tildesley, *Computer Simulation of Liquids*, Clarendon Press, Oxford, (1987).
- [88] W.W. Wood, *Physiks of Simple Liquids* ed H.N.V. Temperley and J.S. Rowlinson and G.S. Rushbrooke, North Holland, Amsterdam, (1968).
- [89] F. Vesely, *Computereperimente an Flüssigkeitsmodellen*, Physik Verlag, Weinheim, (1978).
- [90] J.P. Hansen and I.R. McDonald, *Theory of Simple Liquids*, Academic Press, London, 2nd ed., (1986).
- [91] D. Frenkel, *Computer Simulation in Chemical Physics*, p. 93–152. Kluwer Academic Publishers, Dordrecht, (1992).
- [92] N. Metropolis, A.W. Rosenbluth, M.N. Rosenbluth, A.H. Teller, and E. Teller, *J. Chem. Phys.* **21**, 1087 (1953).
- [93] M. Schoen and D.J. Diestler, *Chem. Phys. Lett.* **270**, 339 (1997).
- [94] H. Bock and M. Schoen, *Phys. Rev. E* **59**, 4122 (1999).

- [95] H. Bock and M. Schoen, *J. Phys.: Condens. Matter* **12**, 1569 (2000).
- [96] H. Bock and M. Schoen, *J. Phys.: Condens. Matter* **12**, 1545 (2000).
- [97] V.P. Gregory and J.C. Schug, *Mol. Phys.* **82**, 677 (1994).
- [98] M. Schoen, C.L. Rhykerd Jr., J.H. Cushman, and D.J. Diestler, *Mol. Phys.* **66**, 1171 (1989).
- [99] P. Bordarier, B. Rousseau, and A.H. Fuchs, *Thin Solid Films* **330**, 21 (1998).
- [100] M. Schoen, S. Hess, and D.J. Diestler, *Phys. Rev. E* **52**, 2587 (1995).
- [101] M. Schoen, *Computer Simulations of Condensed Phases in Complex Geometries*, Springer, Berlin Heidelberg, (1993).
- [102] D.J. Diestler, M. Schoen, and J.H. Cushman, *Science* **262**, 545 (1993).
- [103] M. Schoen, D.J. Diestler, and J.H. Cushman, *J. Chem. Phys.* **100**, 7707 (1994).
- [104] M. Schoen, *Mol. Simul.* **17**, 369 (1996).
- [105] P.A. Thompson and M.O. Robbins, *Science* **250**, 792 (1990).
- [106] P.A. Thompson and M.O. Robbins, *Phys. Rev. A* **41**, 6830 (1990).
- [107] M. Lupkowski and F. van Swol, *J. Chem. Phys.* **95**, 1995 (1991).
- [108] P.A. Thompson, G.S. Grest, and M.O. Robbins, *Phys. Rev. Lett.* **68**, 3448 (1992).
- [109] R. Evans, J.R. Henderson, C.D. Hoyle, A.O. Parry, and Z.A. Sabeur, *Mol. Phys.* **80**, 755 (1993).
- [110] M. Schoen, T. Gruhn, and D.J. Diestler, *J. Chem. Phys.* **109**, 301 (1998).
- [111] C. Bauer and S. Dietrich, *Eur. Phys. J. B* **10**, 767 (1999).
- [112] C. Bauer, S. Dietrich, and A.O. Parry, *Europhys. Lett.* **47**, 474 (1999).
- [113] C. Bauer and S. Dietrich, *Phys. Rev. E* **60**, 6919 (1999).

- [114] N.B. Wilding, F. Schmid, and P. Nielaba, *Phys. Rev. E* **58**, 2201 (1998).
- [115] L.D. Gelb and K.E. Gubbins, *Phys. Rev. E* **53**, 3185 (1997).
- [116] W. Törnig, *Numerische Mathematik für Physiker und Ingenieure*, Springer, Berlin, (1979).
- [117] W.H. Press, B.P. Flannery, S.A. Teukolsky, and W.T. Vetterling, *Numerical Recipes in FORTRAN*, Cambridge University Press, Cambridge, (1990).

Curriculum Vitae

Dipl. Chem. Henry Bock

Date of birth: 15/07/1970

Place of birth: Eisenhüttenstadt/Germany

Nationality: German

Marital Status: married, 2 children

EDUCATION

09/1985 - 09/1989	Carl-Friedrich-Gauß-Gymnasium Frankfurt (Oder)
11/1989 - 11/1990	Military service
04/1991 - 01/1997	Undergraduate, Chemistry Department, Technische Universität Berlin
01/1997	Diploma in Chemistry (roughly equivalent to Masters degree)
07/1997 - present	Ph.D. student, thesis title “Fluids confined by nanopatterned substrates”

PROFESSIONAL EXPERIENCE

01/1998 - present	Member of scientific staff Sonderforschungsbereich 448 “Mesoscopically structured composite systems” (Chairman G. H. Findenegg), TU Berlin
04/1998 - present	Teaching Assistant in courses “Statistical Thermodynamics” and “Mathematics for Chemists”